Infrared Borescopic Characterization of Ignition and Combustion Variability in Heavy-Duty Natural-Gas Engines

by

Ahmet Mazacioglu

A dissertation submitted in partial fulfillment
of the requirements for the degree of
Doctor of Philosophy
(Mechanical Engineering)
in the University of Michigan
2019

Doctoral Committee:

Professor Volker Sick, Chair
Professor Andre L. Boehman
Dr. Michael C. Gross, Southwest Research Institute
Professor Mark J. Kushner

Ahmet Mazacioglu

mazaci@umich.edu

ORCID iD: 0000 - 0003 - 4128 - 177X

DEDICATION

This dissertation is dedicated to science.

ACKNOWLEDGEMENTS

First and foremost, I would like to thank my advisors Prof. Volker Sick and Dr. Michael C. Gross for their continuous support, guidance, and encouragement throughout every stage of this work. I would also like to thank my other committee members Prof. Mark J. Kushner and Prof. Andre L. Boehman for their informative discussions that helped me understand plasmas and internal combustion engines better.

The information, data, or work presented herein was funded in part by the Office of Energy Efficiency and Renewable Energy (EERE), U.S. Department of Energy, under Award Number DE-EE0007307 for High-Efficiency Cost-Optimized Spark-Ignited Natural Gas (HECO-SING) Engines project in collaboration with Robert Bosch LLC. Especially, I would like to thank Justin Kern at Robert Bosch LLC for providing his engineering expertise throughout the project. I would also like to acknowledge Alexander Freitag and Steve White from Robert Bosch LLC for making this project financially possible and sharing their facilities with us.

Finally, I would like to thank all the past and current members of the Sick Lab for contributing to a productive and enjoyable working environment. I would like to especially thank Caleb Sherwood and Margaret Poppe for their industrious work and collaboration in image processing, Dr. Dave Reuss for teaching me about internal combustion engines and sharing his unparalleled approach to engineering, Dr. Hao Chen for his help in Matlab and LaVision DaVis software, James Elkins for his technical support, Angela Wu for her help in Matlab programming, Lucca Henrion for his collaboration in infrared work, Mohammad Alzuabi and Ivan Tibavinsky for data and presentation discussions, Andrew Di Mauro for his collaboration in neural networks, and Allison Gibson for her appreciation of cats.

Table of Contents

LIST OF TABLES

LIST OF FIGURES

NOMENCLATURE

A	projected area of the flame in the image
$c_{m,n}$	pixel intensity at m^{th} row and n^{th} column
CAD	crank-angle degree
CCV	cycle-to-cycle variability
CoV(IMEP)	coefficient of variation of IMEP
EGR	exhaust-gas recirculation
I	second moment of projected area of the flame in the image
IMEP	indicated mean effective pressure
IR	infrared
m	row index
M	total number of rows in the image
mean($MFB_{00.5}$)	the mean value of $MFB_{00.5}$, evaluated over all cycles of a measurement
MFB_x	the crank angle at which *x*% of the fuel mass has been burned, evaluated for one cycle
n	column index
N	total number of columns in the image
P_{max}	peak in-cylinder pressure
$R(x, y)$	Pearson correlation coefficient measured between variables *x* and *y*
r_{gyr}	radius of gyration
S	total integrated signal in an image
x_c	location of the centroid on the *x*-axis
y_c	location of the centroid on the *y*-axis
λ	air/fuel equivalence ratio
$\theta_{x/5}$	the crank angle *x*/5 of the time (in CAD) between spark timing and mean($MFB_{00.5}$)
°aTDC	degrees after top dead center

ABSTRACT

Natural gas (NG) is attractive for heavy-duty (HD) engines for reasons of cost stability, emissions, and fuel security. NG requires forced ignition, but conventional gasoline-engine ignition systems are not optimized for NG and are challenged to ignite mixtures that are lean or diluted with exhaust-gas recirculation (EGR). NG ignition is particularly difficult in large-bore engines, where it is more challenging to complete combustion in the time available.

High-speed infrared (IR) in-cylinder imaging and image-derived quantitative metrics were used to compare four ignition systems in terms of the early flame-kernel development and cycle-to-cycle variability (CCV) in a heavy-duty, natural-gas-fueled engine that had been modified to enable exhaust-gas recirculation and to provide optical access via borescopes. Imaging in the near IR and short-wavelength IR yielded strong signals from the water emission lines, which acted as a proxy for flame front and burned-gas regions while obviating image intensification (which can reduce spatial resolution). Four ignition technologies were studied: a conventional system delivering 65 mJ of energy to each spark, a high-energy conventional system delivering 140 mJ, a Bosch Controlled Electronic Ignition (CEI) system, which uses electronics to extend the duration and the energy of the ignition event, and a high-frequency corona system (BorgWarner EcoFlash). The corona system produced five separate elongated, irregularly shaped, nonequilibrium-plasma streamers, leading to immediate formation of five spatially distinct wrinkled flame kernels around each streamer.

The high-speed infrared borescopic imaging diagnostic developed here is shown to be an excellent method to accurately identify small flame kernels without the need of image intensifiers, comparable to intensified OH* imaging but with reduced experimental complexity. The results acquired from the production engine under varying air/fuel equivalence ratios and EGR rates uniquely demonstrate that stretched and wrinkled early flame kernels have a great advantage over spherical flames to complete combustion faster, and unlike conventional igniters, corona ignition system produces such flame kernels repeatably without heavy reliance on the flow and compositional conditions of the mixture.

CHAPTER 1 INTRODUCTION

1.1 Natural Gas in Heavy-Duty Applications

In heavy-duty (HD) trucks, compression ignition (CI) is currently the most widespread combustion technology, due to its efficiency and low maintenance requirement. However, the Diesel fuel used in CI engines produces substantial pollutants that require costly and complicated after-treatment. There is a growing interest in replacing Diesel fuel with natural gas (NG), which is a much cleaner-burning fuel. Particular interest exists in the United States, for reasons of fuel cost and fuel security. NG has a significantly higher autoignition temperature (580°C) than Diesel fuel (210°C) and a lower cetane number (-10) [1] than Diesel (44-55); hence it is not suitable for CI. On the other hand, the large octane number (122 Motor Octane Number, [2]) of NG makes it very suitable for spark ignition (SI), due to its knock resistance. Additionally, it is preferred to burn NG in lean conditions to minimize fuel consumption, and also use exhaust-gas recirculation (EGR) to reduce emissions of oxides of nitrogen (NO_x). However, reaching these goals is challenging, because common spark-ignition techniques in current use are not specifically optimized for heavy-duty NG combustion, let alone its lean and EGR-diluted versions. Therefore, it is necessary to use an ignition system that can reliably ignite and ensure complete combustion of lean/dilute NG mixtures. In this dissertation, the effectiveness of four ignition systems is compared using standard measurements based on in-cylinder pressure and measurements made by in-cylinder infrared (IR) imaging. Details of the high-speed IR imaging and the quantitative metrics derived therefrom are also provided.

1.2 High-Speed Infrared In-Cylinder Imaging

Even though pressure transducers provide valuable information about the combustion phasing where combustible mixture's mass fraction burned is 0.5% (MFB_{005}) or higher, they do not provide any information about combustion earlier than that because the early flame kernels do not cause a pressure signal significant enough to be detected over noise. Most importantly, pressure sensors do not provide any information about the physics of the in-cylinder processes

that cause the resultant engine output. Ideally, understanding all the critical phenomena inside an engine cylinder requires resolving all the complex processes ranging from atomic length and time scales (~10^{-10} m and ~10^{-10} s to describe spark breakdown) to engine cylinder length and time scales (~10^{-1} m and ~10^{3} s to describe large-scale flows and thermal transience). Resolving all these processes simultaneously and completely in such a large dynamic range is a task yet to be overcome with today's technology. Still, optical diagnostics provide the tools that yield insightful answers to such a complicated problem.

Trade-offs exist between different means of optical access. Optically accessible engines provide the best view of the combustion chamber, but they are expensive, limit peak pressure, limit engine speed, can tolerate only short runtimes, and require extensive maintenance. Borescopes provide much more restricted access, but they can be installed in an otherwise production engine and can withstand the peak pressures normally reached by production engines. For this project, it was mission-critical to operate at the pressures and engine speeds of the development engine, so borescopic access was chosen.

There are also trade-offs between different wavelength bands in which to perform optical measurements. Optical diagnostic techniques (e.g., laser-induced fluorescence, laser-induced incandescence, particle-image-velocimetry, shadowgraphy, schlieren imaging) have been employed in the study of combustion for decades [3, 4]. The vast majority of these measurements have been performed in or near the visible band (~400-700 nm), due to the advanced development level of imaging technology in this band. Silicon is a mature material system, thanks to its use in computer processors, and it offers sensitivity to wavelengths of ~400-1100 nm [5]. Lens technology is also very mature in the visible band, since consumer cameras work in the visible, which enables sophisticated achromatic compound lenses. By contrast, infrared imaging technology is less mature. However, imaging in the IR offers some crucial benefits that make it attractive for combustion research. First, the near-blackbody radiation produced by soot [6] at combustion-relevant temperatures is much stronger in the IR than the visible. More importantly, as shown in Figure 1, the relevant chemical species (e.g., water, carbon dioxide, carbon monoxide) exhibit narrow emission lines in the bands covering 1.0 to 5.5 μm [7-10]. The water lines are of particular interest here. While water is present in the intake charge due to atmospheric humidity, it is found at higher temperature and concentration (both of which yield strong emission) in the volume where combustion has occurred. The significant

increases in water concentration (due to a peak water production rate of ~15x10^{-3} mol/[cm^3-s] for a laminar, stoichiometric, methane/air premixed flame) and temperature (~4-fold for a laminar, stoichiometric, methane/air premixed flame) across the thickness of the flame front, a distance of approximately 0.5 mm under atmospheric conditions (this flame front thickness is even significantly smaller under higher pressures present in engines) [11], allow water to serve as a proxy for the location of the flame front and burned-gas region. Since the IR emission lines are so strong, it is often possible to collect sufficient signal without using an intensifier, thus eliminating an expensive, delicate component that reduces spatial resolution. Due to the limited optical access offered by the borescopes, the IR band was selected for this project in order to maximize the available signal.

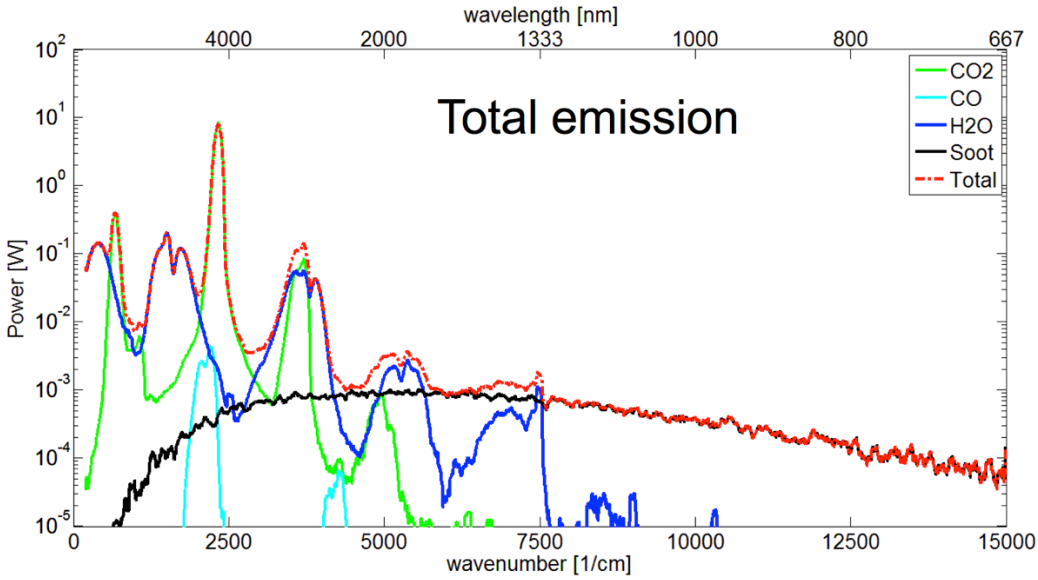

Figure 1. Spectral analysis of radiation in a Diesel engine at 10 CAD aTDC [10].

CHAPTER 2 IGNITION BACKGROUND

2.1 Ignition Limits

Leaner air/fuel mixtures are desirable for improved efficiency, due to more ideal thermodynamic properties of the mixture, reduced pumping work, lower heat losses from lower burned-gas temperatures, and the higher compression ratios that can be reached without knock. However, leaner mixtures require higher ignition energy and some method of accelerating the flame growth so that combustion can be completed during the power stroke. In order to address these requirements, Quader [12] defined two limiting parameters, which are illustrated in Figure 2[13]: (i) the flame-initiation (or ignition) limit, and (ii) the partial-burn limit. The first limit marks the threshold at which ignition fails, and it is affected by factors that cause flame quenching, such as charge dilution, mixture motion, mixture temperature, compression ratio, spark energy, and the spark plug's heat range and gap. The second limit marks the boundary where the flame-propagation speed becomes too low to complete combustion after the mixture is ignited. The partial-burn limit is affected by charge dilution, mixture temperature, mixture turbulence, and the location and geometry of the spark. Spark-timing selection must be made considering both of these limits. Advanced spark timing prevents partial burns, since advanced timing provides more time for the flame to propagate. Advanced timing also leads to more misfires, especially in leaner mixtures, since the temperatures and pressures early in the cycle are not high enough for flame initiation, and the turbulence level quenches the flame kernel. In contrast, retarding the spark reduces the misfire risk, but it also reduces the available time for flame propagation and hence makes the combustion more susceptible to partial burn. For an ignition system, the goal is to remain in the stable combustion zone, but reaching this goal becomes increasingly challenging as the mixture becomes leaner or more dilute or the combustion chamber becomes larger. Even when the misfire and partial-burn limits are not reached directly, inconsistencies in flow and mixing may yield uneven species concentrations and temperature profiles within the combustion chamber, which eventually leads to cycle-to-cycle variability (CCV) [14-17]. CCV is desired to be as low as possible, and ignition selection should be made to enable combustion with minimum instability.

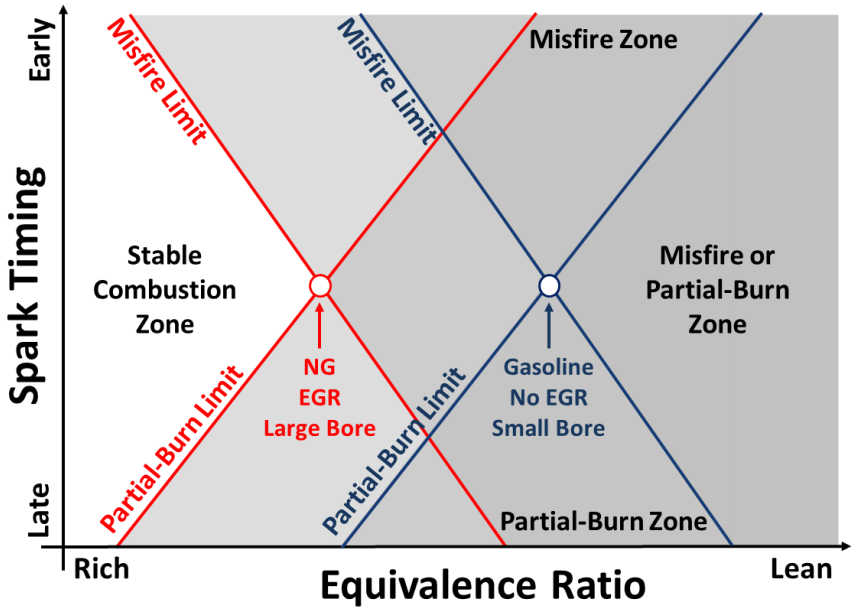

Figure 2. The impact on ignition limits of fuel, air/fuel ratio, dilution, and combustion-chamber size. Adapted from [13].

Typically, advanced ignition systems attempt to overcome the ignition limit by increasing either their output energy (e.g., dual-coil ignition [18, 19], Controlled Electronic Ignition [20]) or the effectiveness of the spark-to-gas energy transfer (e.g. microwave-assisted spark ignition [21, 22], corona ignition [23-25], nanosecond-pulsed transient-plasma ignition[26, 27], breakdown ignition [13], laser ignition [28]). On the other hand, these systems attempt to overcome the partial-burn limit by some combination of increasing the flame-propagation rate (e.g., microwave-assisted ignition [29, 30]) or reducing the flame-travel distance within the cylinder (multi-plug ignition [31], high-frequency corona ignition [25, 32, 33]).

In the work reported here, four ignition systems were compared. The first was a conventional, inductive-discharge ignition (IDI) system [34] that delivered 65 mJ to each spark. The second was an IDI system that delivered 140 mJ. The third used a modified circuit to produce a tunable spark duration and thus tunable energy [20]. The fourth was a a high-frequency corona system (BorgWarner EcoFlash).

2.2 Spark-Ignition Fundamentals

A spark discharge is characterized by the voltage, current, and duration of the spark, which all depend on the surrounding gas, pressure, gap length, gap shape, and the electrical

circuit characteristics. There are four phases of a spark discharge [34]. These phases are illustrated in Figure 3, and the energy distribution during each phase is tabulated in Table 1.

- *Prebreakdown:* A potential difference is applied to a gap with initially infinite impedance. As the voltage increases, free electrons in the gap accelerate towards the anode. If the gap voltage is high enough, these accelerated free electrons collide with the gas molecules in the gap and ionize them, which reduces the impedance of the gap. Similarly, electron-gas collisions result in excited molecules, and these excited molecules radiate ultraviolet (UV) light, which promotes further electron emissions from the cathode, and that emission of electrons eventually (at around 50-100 kV/cm) becomes a self-sustaining discharge, which in turn leads to the next phase: breakdown. The faster the voltage rises, the shorter the prebreakdown phase will be. Typically, the prebreakdown phase is of order 1 ns in duration.
- *Breakdown:* Once the breakdown is reached, the spark current rapidly jumps to ~100 A, causing a rapid increase in the power delivered to the channel, further ionizing the plasma, which further reduces the impedance and the sustaining voltage of the channel. Since the process is so quick, taking only ~10 ns, energy transfer is governed by electron collisions and not by convection/diffusion of the combustible mixture. Therefore, the energy losses in the breakdown phase are minimal, and nearly all the electrical energy transfers directly into the spark plasma (~50 μm in diameter). As the electron temperature rises rapidly to ~60,000 K, the gas in the channel heats, pressure rises, and the plasma channel initially expands with a shockwave at supersonic speed. The breakdown phase is thermodynamically the most efficient phase of spark discharge.
- *Arc:* As the gas around the spark expands, the velocities decay to flame speeds within ~μs, following the breakdown. In the arc phase, currents are still relatively high (>0.1 A), and the gap voltage drops to ~100 V within ~μs. Due to the lengthened timescales, the total energy transferred is greater than in the breakdown phase, but the thermal efficiency is significantly reduced due to heat losses to the electrodes. The electron temperature drops significantly to ~6000 K. All the input energy comes from the capacitance of the high-voltage spark-plug cable and the coil.
- *Glow:* This final phase of discharge happens on a millisecond timescale. Because the energy stored in the capacitance is finite, the input power to the plasma drops, and the current falls to <100 mA. Since the duration of this phase is much higher than the others, it is much less efficient, and the majority of the heat losses to the electrodes occur during glow discharge phase.

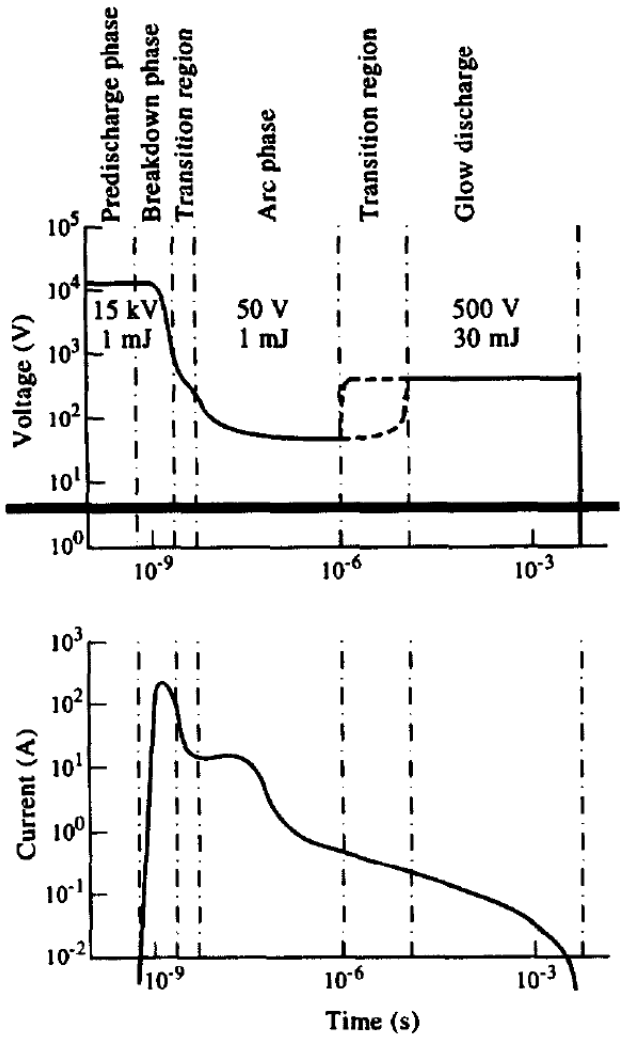

Figure 3. Schematic of voltage and current variation with time for conventional coil spark-ignition system [34].

	Breakdown, %	Arc, %	Glow, %
Radiation loss	< 1	5	< 1
Heat loss to electrodes	5	45	70
Total losses	6	50	70
Plasma energy	94	50	30

Table 1. Energy distribution for breakdown, arc, and glow discharges [34].

2.3 Surveyed Ignition Systems

2.3.1 Conventional Ignition Techniques

Conventionally, a spark ignition system has a device that creates the electrical signal, a high-voltage cable that carries the signal to the spark location, and a spark plug that discharges the current to the combustible mixture. Many ignition systems have variations in terms of appearance, electrical signal output, and performance, yet their circuitry can be simplified as shown in Figure 4 [34]. The two most popular ignition technologies that have been used in the past century and today are inductive-discharge ignition (IDI) and capacitive-discharge ignition (CDI).

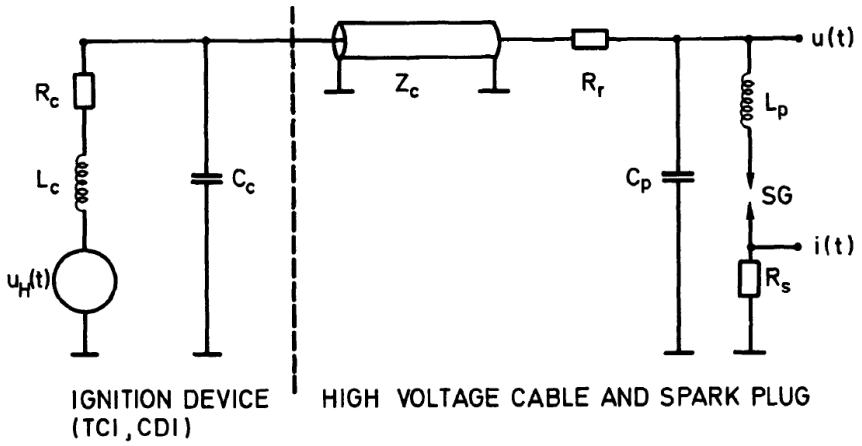

Figure 4. Equivalent circuit of conventional ignition systems. The high-voltage distribution spark gap is omitted since it does not affect the principal functions of the device. u_H,, high-voltage signal; L_c coil inductance; R_c, coil resistance; C_c, coil capacitance; Z_c, cable impedance; R_r, radio-interference-damping resistance; C_p, plug capacitance; L_p, plug inductance; SG: spark gap; R_s, resistance of current shunt (incorporated for measuring purposes only); u, spark voltage; i, spark current; t, time; TCI, transistorized coil ignition; CDI, capacitive-discharge ignition. [34].

2.3.1.1 Inductive-Discharge Ignition

Inductive-discharge ignition, also commonly referred to as transistorized coil ignition (TCI) or Kettering induction ignition, only relies on the coil inductance, L_c, in Fig. 3, to store the electromagnetic energy and provide the high-voltage signal to the spark plug. In such a system, the coil capacitance, C_c, is minimal. As it can be seen from Figure 5, IDI systems are characterized by spark durations on the order of 1 ms (longer than the capacitive-discharge duration by a factor of ~10), which could be beneficial for ignition of lean and highly compressed mixtures at high engine speeds. Generally, IDI systems have a simpler design than capacitive-discharge systems.

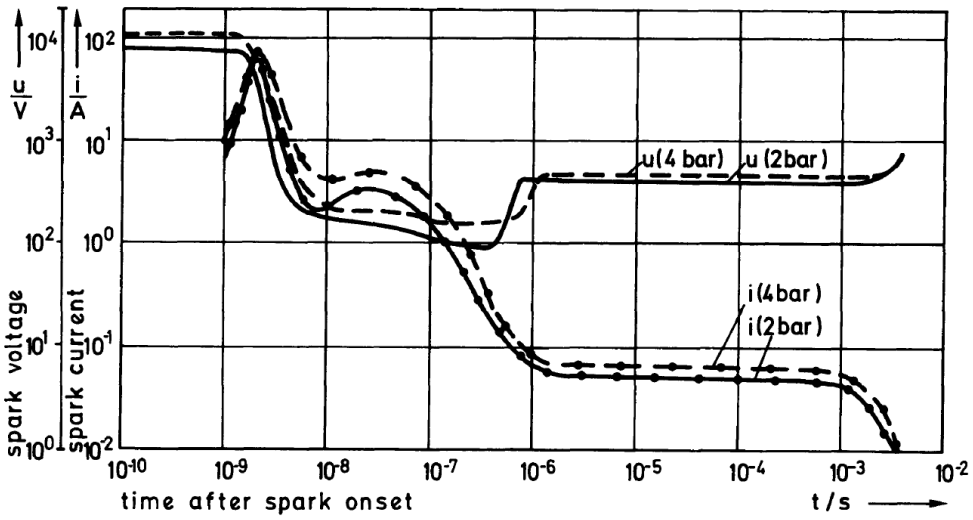

Figure 5. Voltage-time and current-time characteristics of an IDI system in air at 300 K. The systems supplies 30 mJ to a 1-mm gap [34]. *u*, voltage; *i*, current; *t*, time.

2.3.1.2 Capacitive-Discharge Ignition

A CDI system has a circuit that charges the coil capacitor to high voltages until ignition time, and then discharges the capacitor into the ignition coil and then to the spark plug. Coil inductance is typically very low, and the discharge characteristics predominantly rely on the coil capacitance. Material selection becomes more critical and expensive in CDI systems in order to maintain reliability at such high voltages. Compared to an IDI system, a CDI system is characterized by a much shorter discharge (~100 μs, as illustrated in

Figure 6 Figure 6), which leads to lower heat losses at the electrodes, and insensitivity to shunt resistance, though the quick discharge may be problematic for cold-start applications.

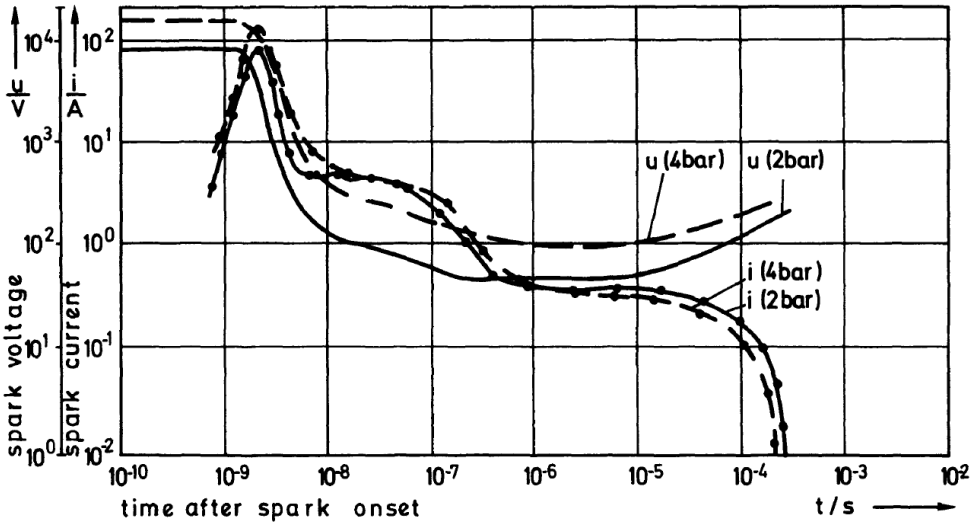

Figure 6. Voltage and time traces of a capacitive-discharge ignition system in air at 300 K and 1-mm gap supplying 3 mJ to the gap electrodes [34].

2.3.2 Long-Duration, High-Energy, Low-Volume Approaches

2.3.2.1 Dual-Coil Ignition

Dual-coil ignition (DCI) is similar to conventional inductive-discharge ignition; however, DCI achieves spark-discharge by means of two ignition coils instead of one, as shown in Figure 7, [35]. These two coils are connected to each other on the primary side, and their secondary sides are connected to the spark plug by means of diodes. At the start of the ignition sequence, the first coil is charged by an electronic control unit. Once fully charged, the first coil discharges, creating a spark plasma. In the meantime, the second coil is charged with a fixed time delay relative to the first coil, and before the spark from the first coil is completed, the second coil spark begins discharging, extending the spark event. This process can be repeated for a number of charge-discharge cycles for each coil. This way, a longer-duration, higher-energy spark is created, as illustrated in Figure 8. The number of charge-discharge cycles is set so that the desired energy can be discharged continuously over a long duration. The main limiting factor for the maximum attainable output from this igniter is the electrodes' durability at high temperatures. Initial tests from BorgWarner show that iridium plugs have a significant durability advantage over platinum plugs in this application. Engine tests with dual-coil igniters show that EGR tolerance can be extended 4-10% depending on the engine load, and the burn rates can be improved [18, 35].

Figure 7. BorgWarner dual-coil ignition system [35].

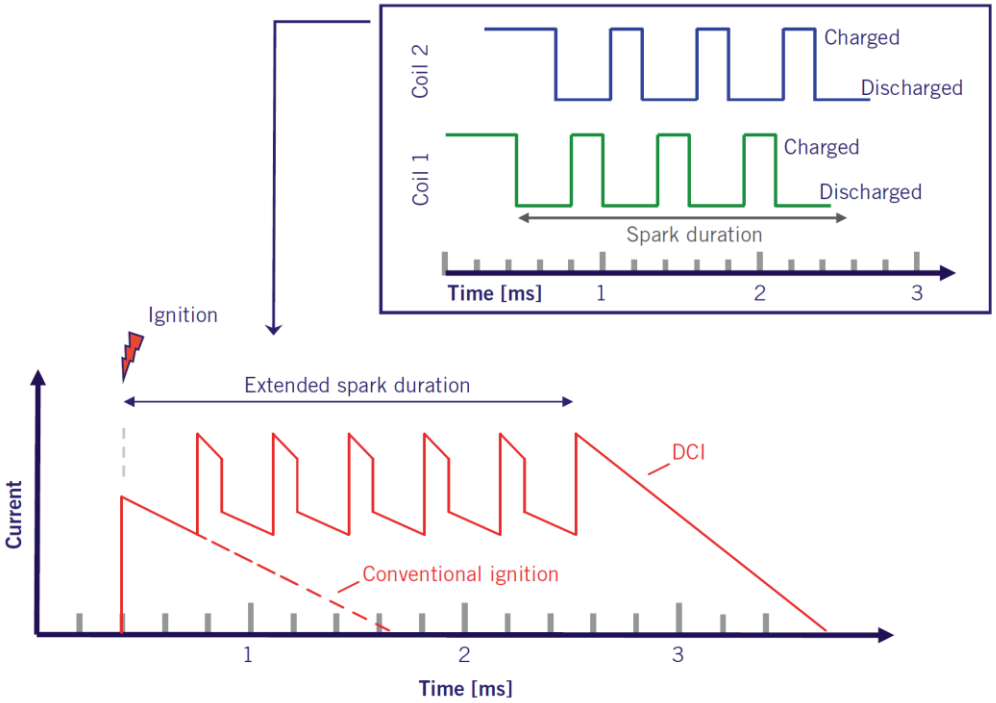

Figure 8. Functional principle of the dual-coil ignition (DCI) [35].

2.3.2.2 Controlled Electronic Ignition

Bosch's Controlled Electronic Ignition (CEI) technology has a modified circuit that enables the system to produce a constant ignition current for a long duration [36]. This way, a higher overall energy output (50-300 mJ) is achieved compared to the conventional ignition systems (~65 mJ) (Figure 9). CEI is also reported to demonstrate ~30% higher spark voltage than conventional igniters. Such a high-voltage, constant-current, long-duration discharge enhances Joule heating and reduces the risk of misfire. Therefore, CEI is a good candidate for EGR-diluted, lean, low-cetane fuel (e.g. CNG, ethanol), and cold-start applications. Potential drawbacks are increased heat losses through electrodes due to increased spark duration, and lower material life due to increased erosion.

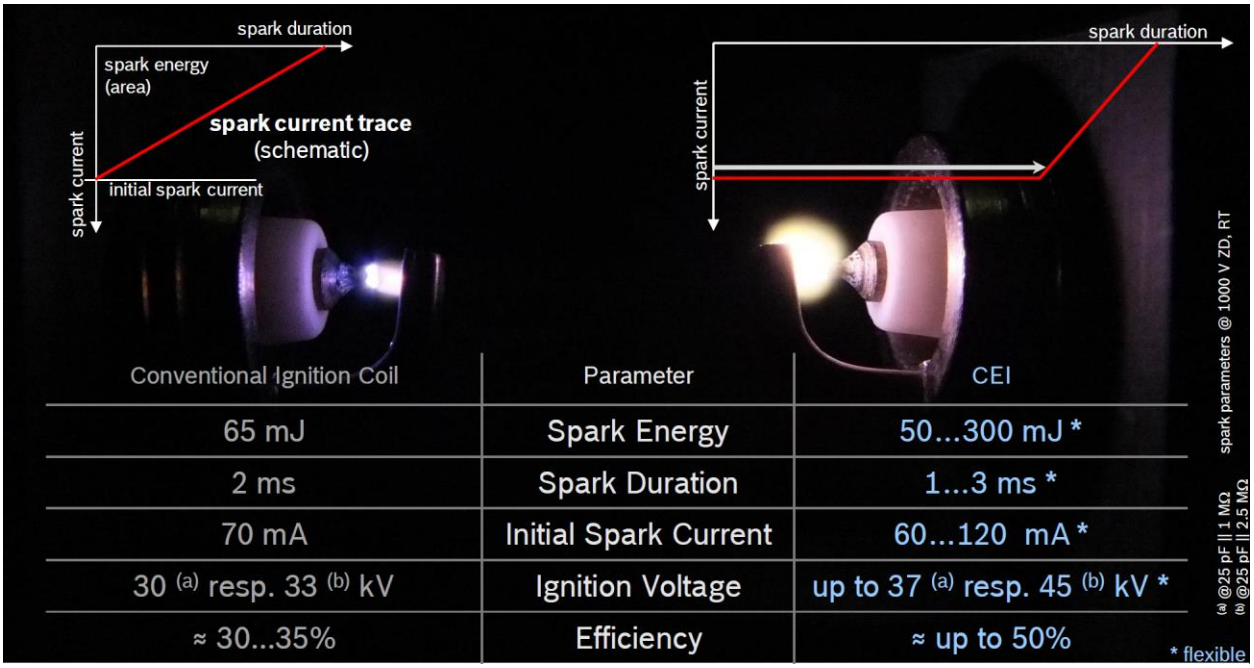

Figure 9. Comparison of conventional ignition and Controlled Electronic Ignition (CEI) [36].

2.3.3 High-Power, Low-Volume Approaches

2.3.3.1 Breakdown Ignition

As explained in Section 2.2, the most energy-efficient phase of a spark discharge is the breakdown, so a straightforward approach to improve a spark igniter is to modify its electrical circuit so that majority of the energy is delivered during this phase. In a typical breakdown ignition system, as can be seen from Figure 10, the voltage drops below 10% of initial value within <10 ns, while the current oscillates with decreasing amplitude for about 60 ns. These

systems deliver their energy in 1/10,000 the time of conventional systems, and reach ~1-2 MW of peak power as opposed to capacitive systems' ~1k W, and inductive systems' ~10 W. This rapid and efficient energy delivery enhances early flame growth. In highly turbulent engines (i.e., smaller, faster engines) the overall combustion duration is decreased, so breakdown systems become especially advantageous [37].

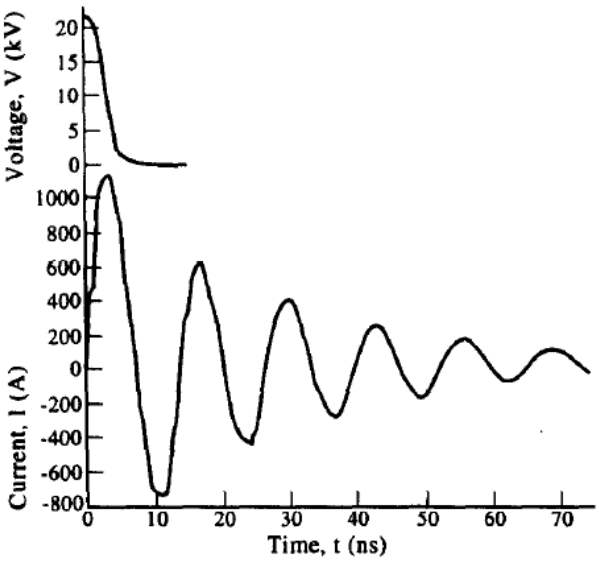

Figure 10. Voltage and current traces for a breakdown ignition system [37].

There are two competing factors that determine a breakdown systems' effect on NO_x emissions, as found in Anderson's experiments [38, 39]. On one hand, the rapid process gives less time for NO_x formation; on the other hand, elevated peak temperatures trigger more NO_x formation. There does not yet appear to be a consensus in the literature on the net impact on NO_x emissions of breakdown ignition systems.

2.3.3.2 Laser Ignition

Since faster energy delivery is preferable for improved thermal efficiency and minimized heat loss, one other approach has been laser ignition. Even higher power outputs (6 MW) are available in ~50 ns with CO_2 laser igniters [37]. There have been serious research efforts on laser ignition (currently still ongoing at Argonne National Lab, Princeton University, and elsewhere), but there are several impracticalities that must be addressed before implementing it on a production engine. The biggest problem is keeping the laser's output window clean and transparent inside a working cylinder. Furthermore, lasers of sufficient power require some means of cooling. Finally, the cost associated with laser-ignition systems (one laser per cylinder

or one laser per engine in addition to switching optics) represents a hurdle. Still, there has been promising studies conducted in reciprocating engines with methane-air or natural gas mixtures [40-43]. An in-depth review on laser ignition principles and potential use can was presented by Phuoc [28].

2.3.4 High-Volume Approaches with Conventional Igniters

2.3.4.1 Multiple-Spark-Plug Ignition

As discussed in Section 2.1 and shown in Figure 2, the two major ignition limits are due to misfire and partial burn. Breakdown and laser ignition systems significantly reduce the risk of misfire, while also reducing partial burns. Another approach that is specifically geared towards solving the partial-burn problem is the use of multiple spark plugs in a single cylinder, as illustrated in Figure 11. This approach reduces the distance a flame must travel by creating multiple flame kernels distributed around the combustion chamber. As a result, the combustion reaches completion faster. Furthermore, the risk of misfire in any given cycle is greatly minimized since it is much less likely that all the plugs will misfire during any cycle.

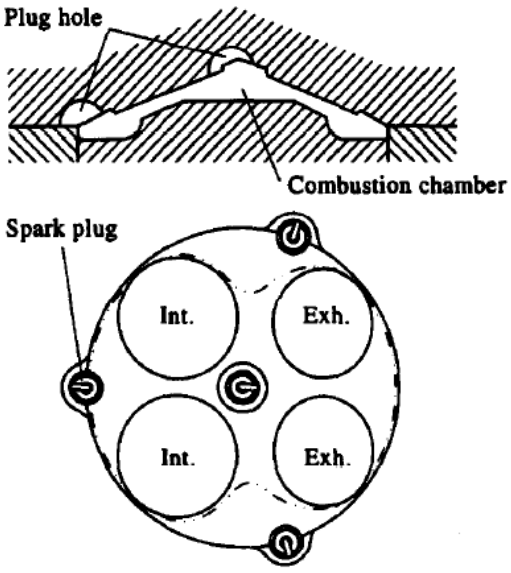

Figure 11. An example of multiple-spark-plug ignition concept [44].

If multiple spark plugs improve performance, then the next question is how many of them are necessary, and how they should be distributed to extend the lean limit. Nakamura studied engines with from 1 to 12 igniters in a single cylinder to answer these questions [45]. Figure 12

shows Nakamura's measurements of brake specific fuel consumption (BFSC), hydrocarbon (HC) emissions, and NO_x emissions as functions of air/fuel (A/F) ratio for several arrangements of spark plugs as well as HC emissions as a function of spark-plug arrangement. (Note that the lean misfire limit [LML] is noted on the curves on the lower right.) Since the combustion duration is decreased and a larger volume is covered, unburned HC, BSFC, and NO_x emissions decrease significantly with increased number of spark plugs. However, the number of plugs itself is not the only determining factor in the combustion performance. All the desirable output parameters become much more favorable when the spark plugs uniformly cover the available area of the head. Since the flames are quenched at the cylinder walls, it is most effective to place the spark plugs more centrally on the cylinder head. Even at lower number of spark plugs (2, 3, or 4 instead of 12) very similar improvements are observed.

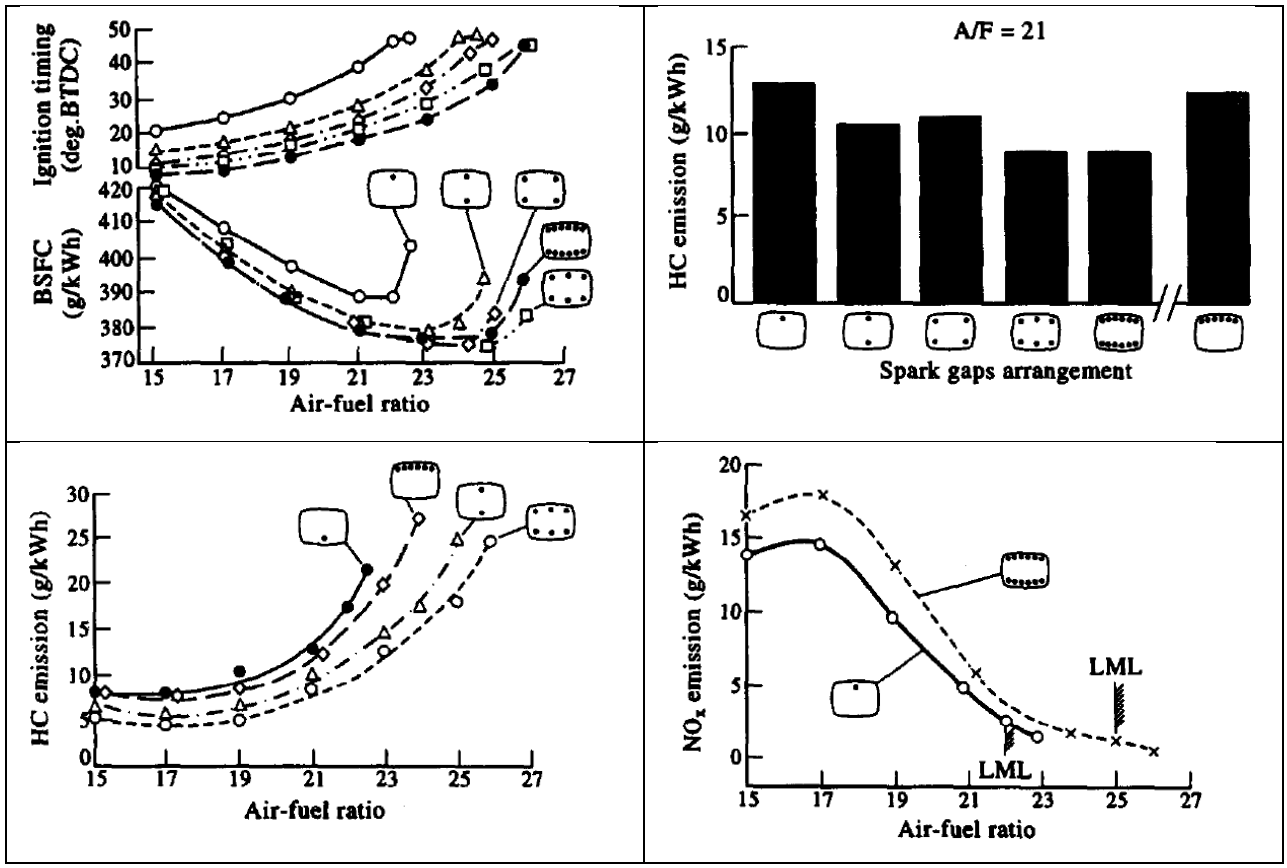

Figure 12. The effect of number and distribution of multiple spark plugs on several important performance and emissions parameters [45]. Abbreviations are explained in the text.

Despite the advantages in fuel consumption and emissions offered by multi-plug ignition, this technology suffers from additional cost and packaging challenges. The packaging issue is

the more critical one. Employing multiple spark plugs not only requires valuable real estate on the roof of the combustion chamber, but it also necessitates re-engineering the entire engine head so that the plugs are isolated from the coolant and do not interfere with the intake and exhaust ports. The packaging challenge has prevented adaptation of multiple-plug ignition in production engines, and the required redesign of the head prevents this technology from being viable for retrofitting an existing engine.

It should be noted that two plugs were used per rotor in many of Mazda's production Wankel rotary engines. (Three plugs were used for each rotor of the Le Mans-winning 787B.) In those cases, the unique shape and moving nature of the working chamber both made multiple plugs more beneficial and easier to package, and the small number of rotors used in each engine mitigated the additional cost.

2.3.4.2 Rail-Plug Ignition

Rail-plug igniters use high-energy electrical discharges (typically ~1 J) inside small-volume cavities. Figure 13 shows a schematic of a rail-plug igniter and the associated electrical circuit. As illustrated in the figure, the electrical circuit is connected to the rail plug at the base of the channel where it is the narrowest. Hence, the electrical signal produces the initial spark at the narrow base, and then the plasma moves along the channel due to thermal expansion. In order to accelerate the spark plasma to higher velocities, a carefully timed electromagnetic force, called Lorentz force, is applied to the plasma by means of an additional follow-on circuit incorporated into a conventional ignition circuit. While the conventional part of the circuit supplies the Joule heating to create the spark plasma, the primary purpose of the follow-on circuit is to supply the Lorentz force to move the ionized spark kernel away from the rail-plug housing to a location within the combustible mixture where the thermodynamic conditions are more favorable for rapid flame growth [46].

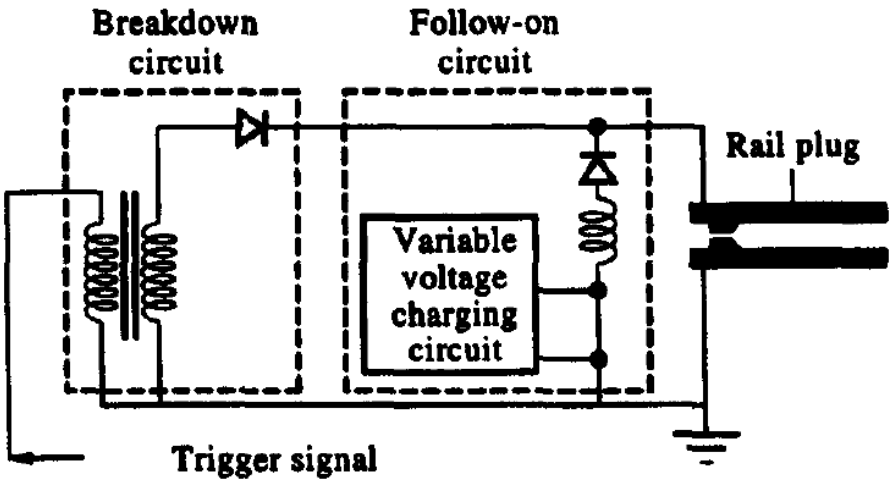

Figure 13. The circuit diagram of a rail-plug ignition system [46].

Laboratory research on rail-plug igniters [46] yielded improvements in indicated mean effective pressure (IMEP) and cycle-to-cycle variation. Unfortunately, several shortcomings of this ignition system were also observed. One drawback is that these igniters have demonstrated shorter material life due to electrode and orifice erosion. This impaired durability could be mitigated by using more sophisticated materials, but only at increased cost. The high power of the discharge also yields higher heat-transfer losses and a potential safety hazard. Although rail-plug ignition never reached commercialization due to its shortcomings, this technology demonstrated the importance of larger volume ignition, which later, more advanced systems tried to achieve by different means.

2.3.5 Momentum-Based Approaches

2.3.5.1 Pre-Chamber-Initiated Ignition

Another method to improve the ignitability of lean mixtures is to utilize a pre-chamber ignition system. In this system, there is a small combustion chamber containing a fuel injector (or fuel-scavenging mechanism) and an igniter that is attached to the much larger main combustion chamber. The pre-chamber is filled with a rich, easily ignitable air-fuel mixture, and a much leaner mixture is supplied to the main chamber. The overall air/fuel ratio is typically lean. As the pre-chamber mixture is ignited, the hot burned gas mixture flows out of the pre-chamber through nozzles to the main chamber, penetrates into the leaner mixture, and the radical-rich hot jet (Figure 15) ignites the leaner main chamber mixture.

Many pre-chamber concepts have appeared in the literature, as diagrammed in Figure 14, [47]. The systems differ from each other mainly in terms of the pre-chamber fueling technique, the relative volume of the pre-chamber, the size of the nozzles, and the flow characteristics of the pre-burned igniter jet.

According to Toulson's 2010 review [47], jet ignition, while showing near-Diesel thermal efficieny and fuel economy, also exhibits the emissions, noise, and control advantages of SI and is projected to be less expensive than Diesel due to the reduced aftertreatment costs. Toulson's table comparing the advantages and disadvantages of jet ignition compared to spark ignition, Diesel, and HCCI is provided in Table 2.

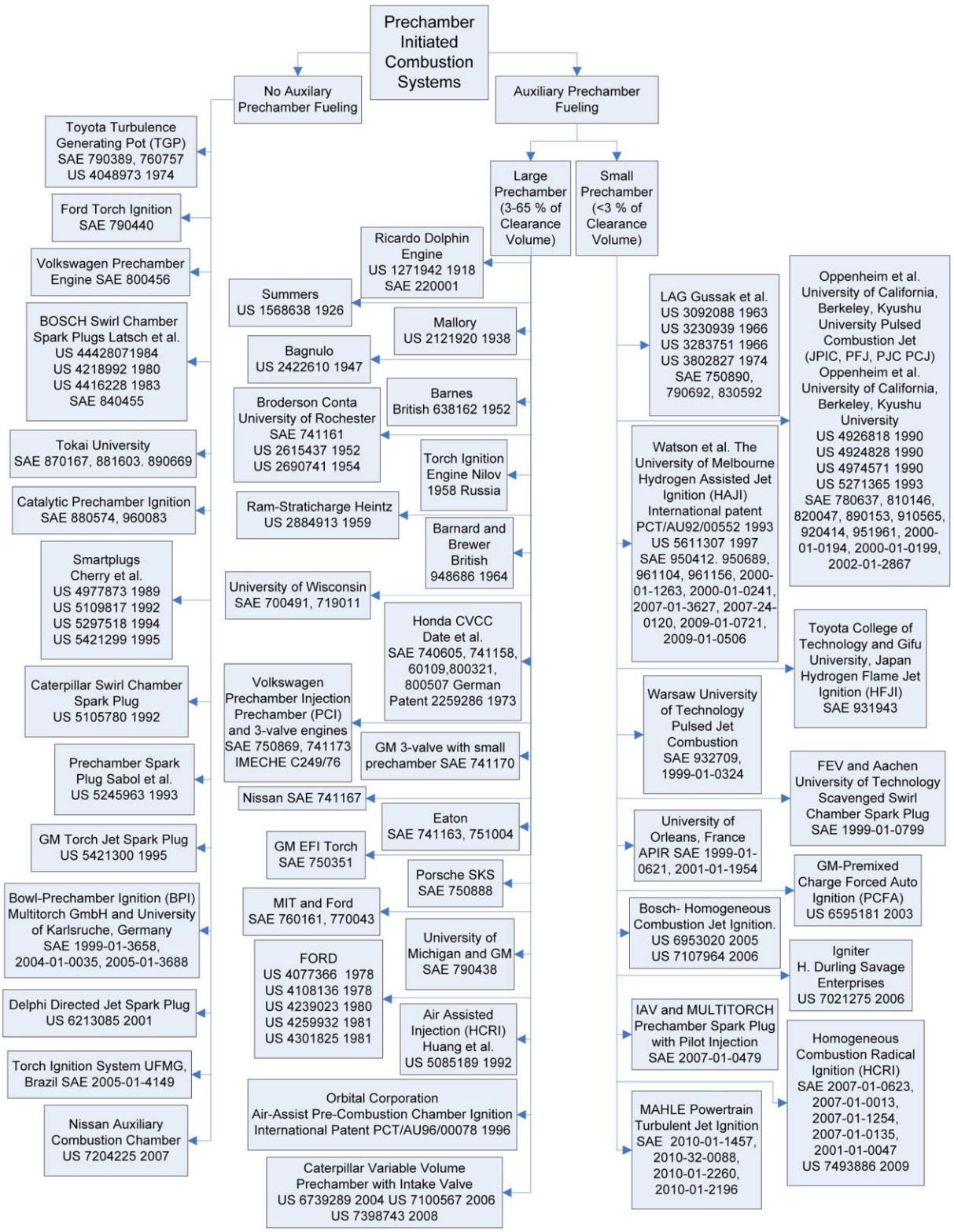

Figure 14**.** Summary of the developmental history of pre-chamber ignition systems [47]. Each branch is arranged in chronological order from top to bottom.

	Spark Ignition	Diesel	HCCI	Jet Ignition
Special technology required for implementation	Spark plug, port fuel injector or direct injector, 3-way catalyst	Direct injector, advanced emission clean up technology for PM and NOx	Variable valve lift and phasing, spark plug, direct injector, advanced control system with closed loop combustion control, 3-way catalyst (stoichiometric) or a lean NOx trap, NSC or SCR may be required	Spark plug, direct injector (pre-chamber) and port or direct injector (main chamber), 3-way catalyst
Emissions	Very low emissions can be achieved with a 3-way catalyst	NOx and PM emission clean up technologies such as particle traps, lean NOx traps, NSC or SCR are expensive	Low engine out NOx but may not be low enough to not require expensive lean-NOx after-treatment to meet emission standards	Low engine-out NOx emissions. A 3-way catalyst or oxidation catalyst is required
Peak efficiency	Least efficient	High efficiency	High efficiency relative to SI, near Diesel efficiency	High efficiency relative to SI, near Diesel efficiency
Speed / load range	Successful over production range	Successful over production range	1-5 bar BMEP load (normally aspirated) up to ~16 bar boosted 1000-4000 rev/min speed range [10]	Successful over production load range, limited data available at high speeds
Fuel economy over drive cycle	Lowest drive-cycle fuel economy	Best drive-cycle fuel economy. Up to 30% improvement over SI	Up to 10-15% improvement relative to spark ignition	Up to 18% improvement relative to spark ignition [11]
Controls	Least complicated control strategy	Complicated control strategy to ensure emission clean-up	Most complicated control strategy that must manage mode transitions and transients	Control strategy similar to SIDI with multiple pulse injections
NVH (noise)	Least noisy. Max pressure rise rate at 1500 rev/min, 3.3 bar IMEPnet [11]: ~1.5 bar/CAD, λ=1 ~1.2 bar/CAD, λ=1.4	Combustion generated noise requires engine compartment silencing Max pressure rise rate at 1500 rev/min, 3.3 bar IMEPnet [13]: ~5-8 bar/CAD	Noise similar to diesel, requiring engine compartment silencing. Max pressure rise rate at 1500 rev/min, 3.3 bar IMEPnet [12]: ~4 bar/CAD, λ=1.3	In the range of spark ignition. Max pressure rise rate at 1500 rev/min, 3.3 bar IMEPnet [11]: ~1.8 bar/CAD, λ =1 ~0.8 bar/CAD, λ =2
Engine structure	Lightest and least expensive	Must design for very high rates of combustion pressure rise adding cost and weight	High rates of pressure rise add cost and weight due to structural concerns	Similar to spark ignition
Reliability	Very reliable	Very reliable	In R&D phase	Unknown
Cost	Least expensive	Very expensive due to emission after-treatment	More expensive than SI but projected to be less expensive than Diesel	More expensive than SI but projected to be less expensive than Diesel

Table 2**.** General comparison of common combustion technologies and jet ignition [47]. HCCI, homogeneous-charge compression ignition; PM, particulate matter; NO_x, oxides of nitrogen; NSC, NO_x storage catalyst; SCR, selective catalytic reduction, SIDI: spark Ignition Direct Ignition.

2.3.5.1.1 The LAG Process

After the jet-ignition concept was first introduced in the late 1950s. Gussak [47, 48] developed the first jet-ignition engine. He named the jet-ignition process Lavinia Aktivatisia Gorenia (LAG), Russian for Avalanche Activated Combustion. To this day, the mechanism behind jet ignition is still known as the LAG process. In the LAG process , as illustrated in Figure 15 , active radicals from a quenched flame provide “avalanche kernels” as a distributed ignition source in the main chamber. Gussak determined that, in order to produce the most

effective radical-rich, high-momentum jets, the pre-chamber geometry should be as follows: pre-chamber size equal to 2-3% of the clearance volume, orifice area 0.03-0.04 cm^2 per 1 cm^3 of pre-chamber volume, and orifice length/diameter ratio of 0.5 [49]. The most significant discovery from the this work was the importance of active radicals in pre-chamber ignition [50].

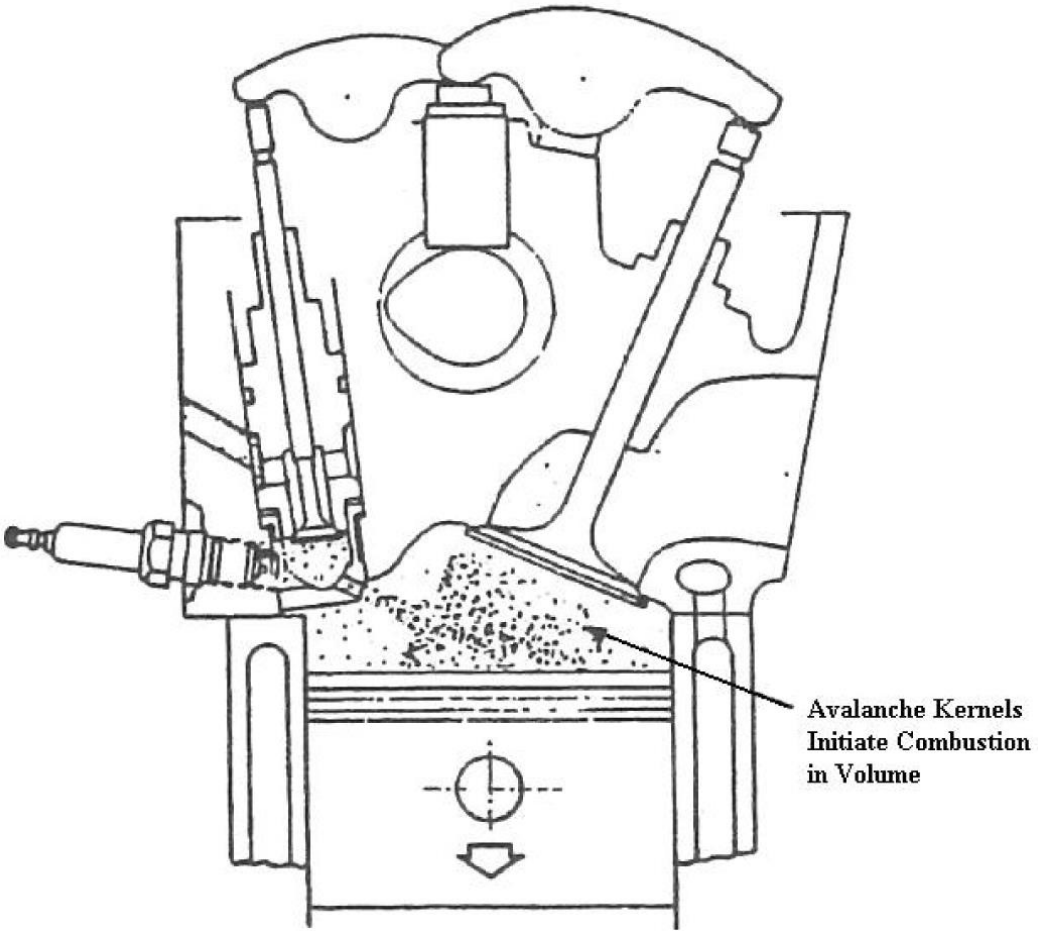

Figure 15. An illustration of the Lavinia Aktivatisia Gorenia (LAG) process showing the avalanche kernels [47, 48].

2.3.5.1.2 Turbulent Jet Ignition

In the most recent, most advanced version of pre-chamber-initiated ignition is MAHLE Turbulent Jet Ignition (TJI), recently renamed MAHLE Jet Ignition (MJI), which is illustrated in Figure 16 and Figure 17. The design goals for this system were as follows:

- A very small pre-chamber size (~2% of the main chamber) so that the fuel consumption is reduced.

- Very small nozzles (~1 mm^2) so that the igniter jet can be turbulent (and possibly supersonic when converging-diverging nozzles are used) and can carry more momentum to penetrate deeper into the lean main chamber gases.
- Finer control over the fueling location and stratification within the pre-chamber.
- Finer control over the spark location, timing, and energy within the pre-chamber.

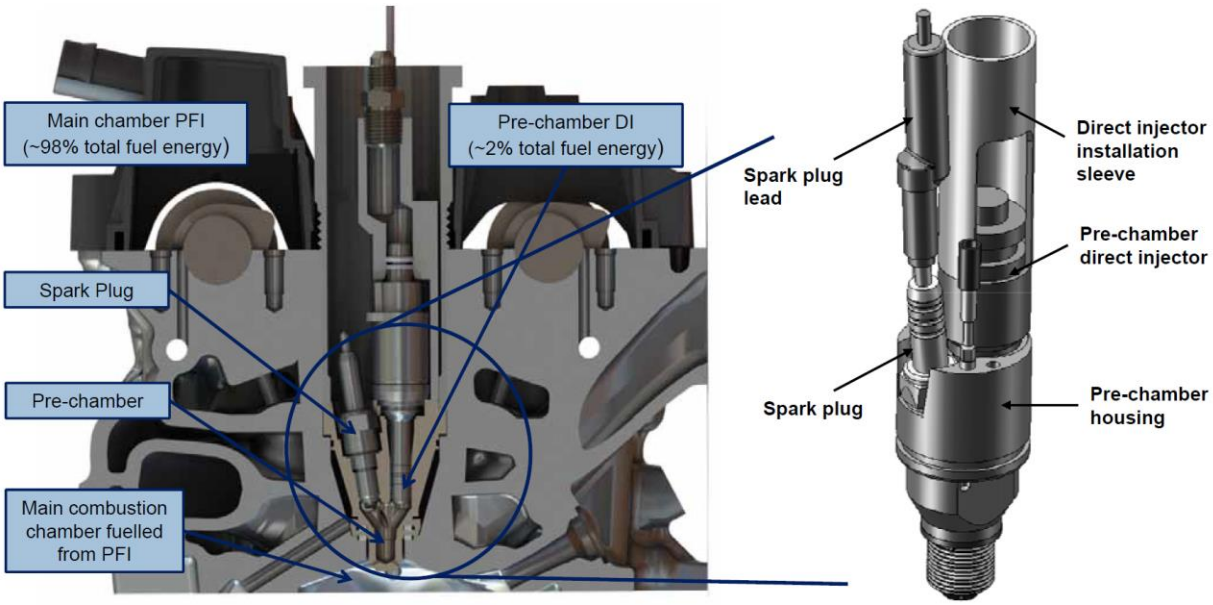

Figure 16. Drawings of the MAHLE Turbulent Jet Ignition system [47].

The combusting jets produced in TJI provide ongoing combustion and motion of substantial fuel/air mass that enables combustion in diluted mixtures and generally benefits engine efficiency [47]. The TJI system has been shown to enable ultra-lean operation (fuel/air equivalence ratio, ϕ, <0.5), exhibit very high EGR tolerance, yield very high (near-Diesel) thermal efficiency, and reduce NO_x emissions significantly. There is some concern that the additional surface area of the pre-chamber may cause higher heat losses than conventional systems, though the high thermal efficiency demonstrated indicates that a properly sized pre-chamber may minimize this heat loss. The TJI system does suffer from some increased cost, due to the substitution of a pre-chamber, spark plug, and second injector for a single spark plug and the additional fuel-delivery components. The main shortcoming of this system, however, is the packaging requirement. The pre-chamber module is by necessity significantly larger than a spark plug. Fortunately, the area occupied on the roof of the combustion chamber is approximately the same as that of a single spark plug.

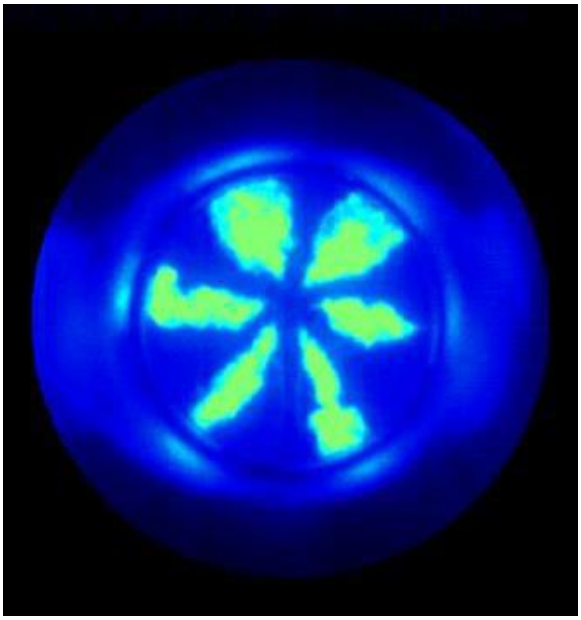

Figure 17. MAHLE Turbulent Jet Ignition system: Image of the hot turbulent jet leaving the pre-combustion chamber to ignite the mixture in the main chamber [47].

2.3.5.1.3 Supersonic Jet Ignition

As an effort to increase the penetration speed of the pre-combusted jet, a 2016 study conducted by Biswas at Purdue investigated the potential effects of utilizing supersonic jets, instead of subsonic deflagration jets [51]. In this laboratory setup, a small pre-chamber is connected to a larger constant-volume main chamber through a single nozzle. Three different nozzle geometries (straight, converging, converging-diverging), which result in different jet flow regimes, were tested. Significant lean-limit extension (from $\phi = 0.35$ to 0.22 in the main chamber) was observed under supersonic jet conditions produced by a converging-diverging nozzle, compared to the subsonic jet conditions formed by a straight nozzle of same throat area. In infrared imaging and OH* chemiluminescence imaging, diamond-shaped shock structures in the supersonic jets and a high-temperature zone downstream of the shocks were observed. The lean-limit extension was attributed to these additional high-temperature zones.
Unfortunately, supersonic jet ignition operating in ultra-lean conditions also results in pressure-related combustion instabilities. In the main chamber, an acoustic disturbance grows and eventually affects heat-release rate and causes oscillating flame propagation. Such acoustic concerns would likely be a significant problem in a reciprocating engine where the shockwave-boundary interactions would be much more complicated. It should also be noted that the fuel used for this experiment was H_2, which was chosen due to its simplicity. Additional difficulties

might be observed in more complex fuels. Despite the current shortcomings, the idea of nozzle modification in a jet ignition system may yield result in improved performance as the nozzle design is iterated.

2.3.5.2 Diesel-Pilot Ignition

Another method that utilizes a high-momentum igniter jet is Diesel-pilot ignition. In this type of system, the engine runs primarily on natural gas, but a small quantity of Diesel fuel is used as the ignition source [52]. The spark plug found in a conventional NG engine is replaced with a Diesel injector, as shown in Figure 18. The Diesel fuel is sprayed in jets, and due to the high cetane number of the fuel, it autoignites and then serves as a distributed ignition source for the NG that is injected shortly after the Diesel. Since the pilot Diesel fuel is supplied in small quantities, one major concern with Diesel-pilot is keeping the Diesel fuel locally rich enough to ignite with a short ignition delay. Hence, Diesel and NG injection timings must be arranged such that the natural gas does not lean down the initial Diesel spray, preventing autoignition.

This method of ignition leads to much lower soot and NO_x emissions compared to pure Diesel engines, while still maintaining a reasonably high brake mean effective pressure. Unfortunately, storing and delivering two different fuels and the complicated injection system represent two major drawbacks. Even though there are cases where NG is supplied via port fuel injection [53], direct injection of the NG is preferred due to its ability to more carefully control the timing and distribution of the natural gas relative to the Diesel fuel [54].

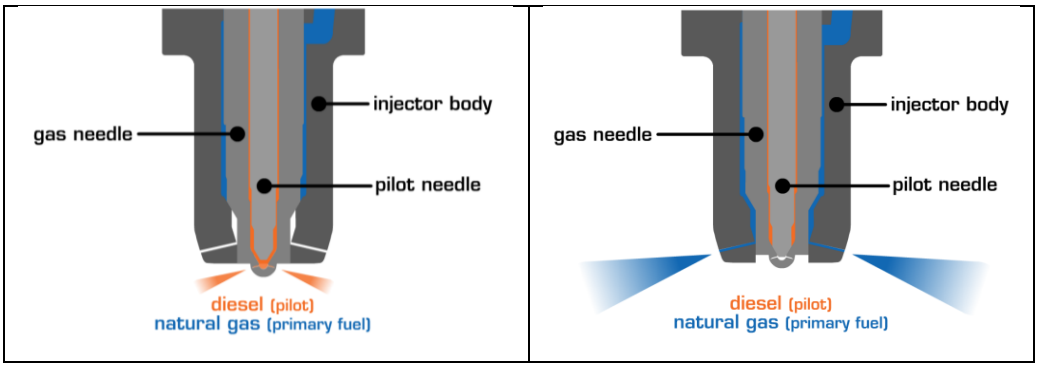

Figure 18. Westport high-pressure Diesel-pilot injector assembly. A single injector delivers the Diesel fuel first, then the natural gas [54].

2.3.6 Approaches Exploiting Non-Equilibrium Plasma

2.3.6.1 Introduction to Plasmas

A number of advanced ignition technologies exploit the properties of non-equilibrium plasmas, so a short introduction to the different types of plasmas is provided in this section.

A plasma is an ionized gas, which can be created from an ordinary gas by heating it or subjecting it to a strong electric field produced by a microwave oscillator or laser. Plasmas, unlike non-ionized gases, have are highly chemically active, exhibit electrical conductivity, and contain high-energy particles [33]. Fully ionized plasmas are quasi-neutral (*i.e.*, instantaneously contain equal amounts of negative and positive charges) systems in which only ionized gas particles and electrons are present and show collisionless, collective behavior. At continuum scale, an ideal plasma only has Coulomb interactions between its particles. Partially ionized plasmas contain non-ionized gas particles along with ionized gas and electrons; hence they behave as a transition state between an ordinary gas and an ideal plasma. Both long-range (Coulombic) and short-range (collisional) interactions are present and effective in a partially ionized plasma [33]. Depending on the temperature and pressure, plasmas can gain or lose ideality. Partially ionized plasmas are more common in the published ignition studies.

In a plasma, electrons, due to their much lower mass, can reach much higher kinetic energies than can heavier particles (ions, radicals, gas molecules, atoms). Hence, a plasma can contain high-temperature electrons and low-temperature ions simultaneously [55]. However, this phenomenon can occur only under non-equilibrium (also called transient or non-thermal) conditions; therefore, such a plasma is called non-equilibrium plasma, transient plasma, or non-thermal plasma. Non-equilibrium plasmas can only be sustained under higher Townsend

numbers (ratio of electric field to the particle density), which in a typical internal combustion engine setting means high electric fields and low pressures [33], otherwise the high-temperature electrons dissipate their energy into the surroundings via collisions until the plasma reaches localized thermal equilibrium. Table 3 summarizes the differences between thermal and non-thermal plasmas.

Plasmas can also be divided into two groups depending on temperature: low-temperature plasmas have electron temperatures below about 10^5 K, while high-temperature plasmas are above that threshold. Typically, automotive engines utilize low-temperature plasmas for ignition. Low-temperature plasmas can be either thermal or non-thermal, while high-temperature plasmas are typically thermal under engine pressures and particle densities. Table 4 illustrates the typical temperature ranges of ions and electrons separately for each kind of plasma.

Thermal Plasma	Non-Thermal Plasma
- The electron temperature is equal to the temperature of the bulk gas. - High gas temperatures are observed. - High levels of ionization are observed.	- The electron temperature is higher than that of the ions. - Reaction kinetics are enhanced. - Lower gas temperatures are observed. - There is potential to influence flame stability (by modifying Lewis numbers and promoting wrinkling).

Table 3. Comparison of thermal and non-thermal plasma comparison based on [22].

Low-Temperature Plasma		High-Temperature Plasma
Thermal	Non-Thermal	
$T_i \approx T_e \approx 10^4$ K Example: electro-thermal chemical plasma	$T_i \approx 10^2$ K, $T_e \approx 10^4$ K Example: corona discharge	$T_i \approx T_e \approx 10^7$ K Example: fusion plasma

Table 4. Plasma classification based on temperature and thermalization [33]. T_i, typical ion temperature; T_e, typical electron temperature

2.3.6.2 Microwave-Assisted Ignition

Studies on premixed laminar-flames show that spark-ignited flames propagate faster when they are under a microwave (MW)-generated electric field [29, 56]. Laser diagnostics on

laminar flames further reveal that the peak density of hydroxyl radicals (neutral OH molecules) near the flame front under MW assistance is enhanced significantly, which leads to higher flame speeds [57]. Recently, there has been an effort in Dibble's lab at the University of California at Berkeley to test microwave-assisted spark ignition technology [22]. The experiments have been performed with methane (the primary constituent of natural gas) in a constant-volume combustion chamber with a conventional capacitive-discharge spark plug and an additional MW source to enhance the electron mobility without increasing the gas temperatures. The combination of the spark plug and MW signal produced, a non-equilibrium plasma in the methane. The resulting combustion demonstrates improved reaction kinetics and early flame-kernel growth without raising the peak gas temperatures at the ignition site. The MW-enhanced kinetics eventually leads to faster flame development, extension of the ignitability limit, and lower NO_x emissions.

Figure 19 shows Schlieren images of early flame growth in methane ignited by conventional spark ignition and by microwave-assist SI in Dibble's constant-volume chamber [22]. All frames were recorded 5 ms after ignition. Although the faster flame growth is noticable at lower pressures (~1-2 bar), the advantage disappears as the pressure increases beyond ~3 bar, because of the higher rate of molecular collisions mitigating the mobility enhancement of MW-assisted ignition. This high-pressure effect is a very serious problem that prevents the adaptation of MW-assisted ignition in SI engines, because in reciprocating engines, the pressures at the time of ignition are well above 5 bar. Still, one must take into account that the high temperatures in a real engine can also reduce the gas density in the engine, thus reducing molecular collisions, which could mitigate the effect of high pressure and make MW-assisted ignition more viable. Optical-engine tests with MW-assisted igniters were performed by Imagineering, Inc. in Japan [21, 58]. Under low-pressure conditions (2.75 bar IMEP, ~20 bar maximum pressure), substantial improvements in lean limit, OH density, IMEP, cyclic pressure stability, and CO emissions are recorded. Under slightly higher-pressure conditions (5 bar IMEP, still significantly lower than found in a heavy-duty engine), the gains diminish substantially. Overall, the published results indicate that MW-assisted ignition is far from ready for use in production or production-based engines.

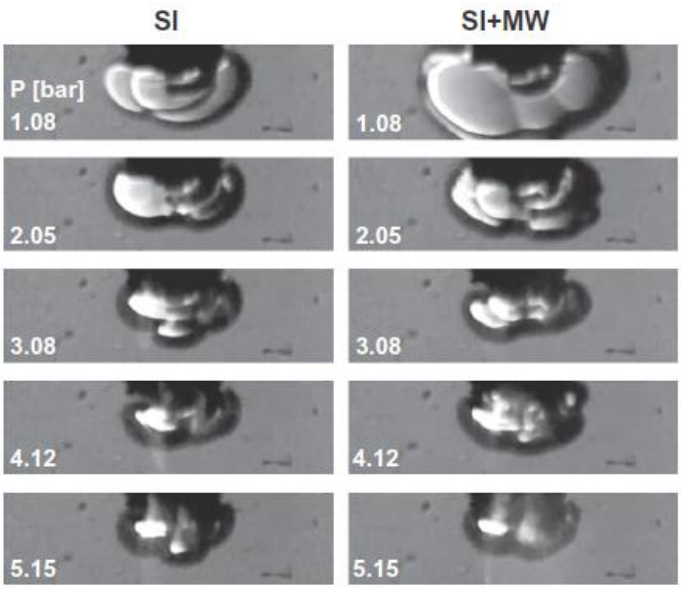

Figure 19. Schlieren images of early flame growth using spark ignition (SI, left) and microwave-assisted SI (SI+MW) [22]. All images are recorded 5 ms after ignition. Pressures increases from top to bottom. Notice how SI+MW flame growth is much faster than SI at lower pressures, and how that effect diminishes with the increasing pressure.

2.3.6.3 Corona Ignition

Between two electrodes, if the potential gradient (electric field) is sufficiently large to ionize the gas only at multiple discrete points, then ionization occurs only at these particular points while the rest of the gas remains mostly unaffected. Such low-power electric-discharge plasmas that occur near atmospheric conditions are known as a corona discharge [33]. Generation of a corona discharge is only possible after the corona inception voltage (CIV) for that particular electrode set is provided to the system. CIV is found by an empirical equation named Peek's law, which describes very strong dependence between CIV and the geometry of the electrodes [59]. In particular, the curvature ratio between the anode and cathode is the primary determining factor, which sets corona apart from an ordinary spark. For the lowest CIV, one of the electrode tips should be very sharp (needle-like), while the other one should be flat. For instance, in an engine application with corona ignition, a regular spark plug is completely replaced by an anode with a sharp tip (or multiple sharp tips, see Figure 20), while the cylinder wall, which has a much longer-radius curvature, behaves as the cathode. Gas density and the distance between two electrodes are the other important factors that determine the value of CIV. Polarity selection of electrodes is also critical. For either polarity selection, the discharge occurs at the sharp tips due to higher localized electric field; for ignition applications, the sharper

electrode is specifically selected to be the positive electrode in order to have a positive corona (also known as streamer corona) discharge. In such a discharge, positive ions, also called streamers, move away from the sharp tip and propagate through the gas, and the resulting streamers cover more interelectrode space than a negative corona does. Corona discharge also results in a secondary flow within the gas, called ionic wind, that increases the level of turbulence and facilitates faster and more efficient combustion.

Corona discharge has many advantages over spark discharge. As a process based on non-equilibrium plasma, corona discharge carries its energy through electrons that are significantly hotter than the bulk gas (Table 4). Corona relies on electron-impact decomposition instead of Joule heating of the combustible mixture from spark discharge [27]. Hence, without dumping unnecessary energy into heating the gas, the reaction kinetics are favored such that combustion happens faster, colder, with lower NO_x, and with minimized heat loss in the electrodes. Most importantly, as opposed to a traditional spark igniter's ~1-mm single-channel plasma, a corona igniter creates multiple, ~25-mm long streamers [25]. Therefore, corona ignites a much larger volume of the mixture, leading to distributed, turbulent, fast-propagating flame kernels as can be seen from Figure 21 [32].

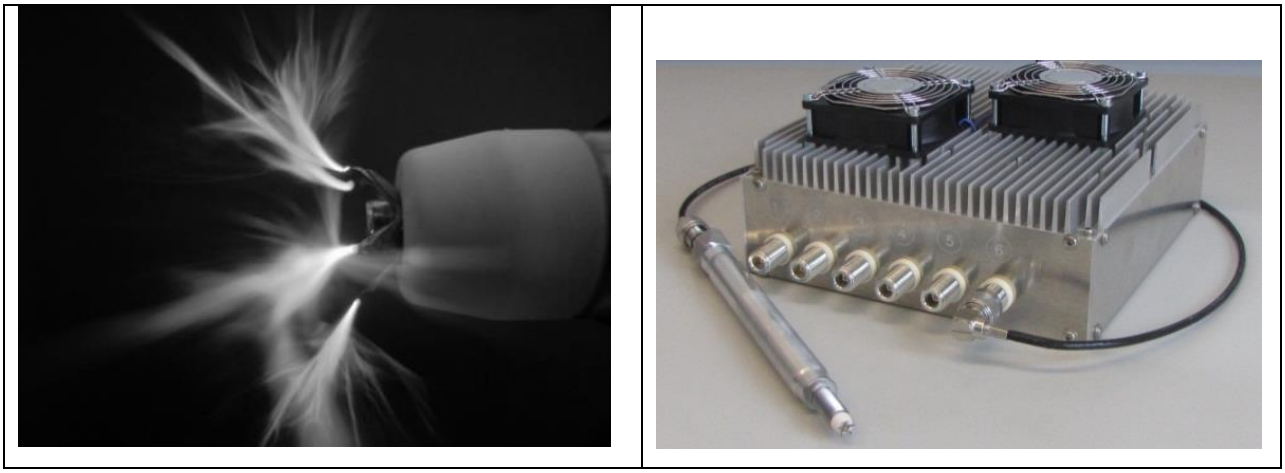

Figure 20. BorgWarner EcoFlash ignition system [25]. Corona discharge in ambient air (left), and prototype assembly (right).

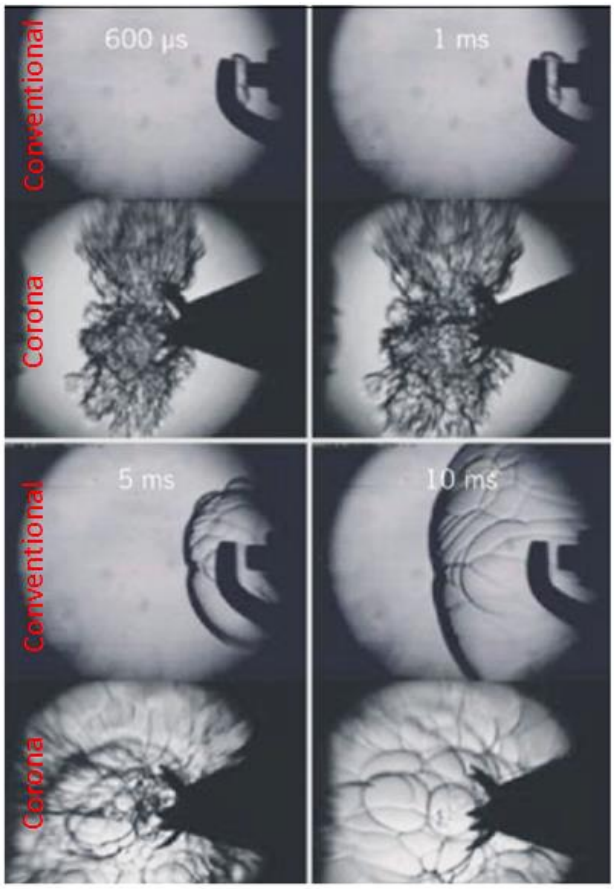

Figure 21. Comparison of combustion initiation by conventional spark ignition (Bosch PPlus-transistor coil ignition with enhanced performance) and by corona ignition (BorgWarner EcoFlash prototype) with E20 fuel at a filling pressure of 20 bar, a mixture temperature at 200 °C and a combustion air ratio of λ=1.0 [32].

In 2007, Cathy *et al.* conducted single-cylinder, gasoline-fueled optical-engine experiments to compare corona ignition against the conventional technologies, and corona demonstrated higher energy efficiency and more rapid flame initiation than the rest of the systems tested [26]. In 2013, Graf [60] tested corona ignition against other popular igniters (transistor coil, modulated direct current, single charge ignition, multi-charge ignition systems, and their varieties) in a research engine with E20 fuel, and corona performed significantly better than the other systems in terms of engine running smoothness, ignition delay, and combustion duration. Graf's results are illustrated in Figure 21. In 2014, Briggs in 2014 [32] tested 18 different igniters, including a corona igniter, a laser igniter, a rail-plug igniter, multiple surface igniters, different kinds of torch igniters, along with various conventional systems. Corona ignition demonstrated the highest burn rates, and the lowest variability of them all.

2.3.6.4 Nanosecond-Pulsed Transient-Plasma Ignition

A nanosecond-pulsed transient-plasma ignition systems use short electrical pulse trains to produce a non-equilibrium plasma and to facilitate rapid, energy-efficient, low-temperature combustion [26, 61-69]. These electrical pulse trains consist of 5-20 pulses with durations of ~10 ns, pulse spacings of 0.1-600 μs, and peak powers of 650 kW [62, 63]. The resulting plasma, created under high electric field, enables gas excitation, dissociation, and ionization by electron-impact, which creates new chemically active species that can facilitate additional interaction mechanisms that modify and accelerate the kinetics of the entire combustion [66, 67].

In experiments conducted in a constant-volume chamber, nanosecond-pulsed transient-plasma ignition systems demonstrated a "jetting" effect where the flame kernel was expelled outwards into the chamber away from the spark electrodes, The jetting increases flame wrinkling, which enhances the flame-kernel growth rates. Increasing the number of pulse enhances the flame-propagation rates. These results are illustrated in Figure 22, [62].

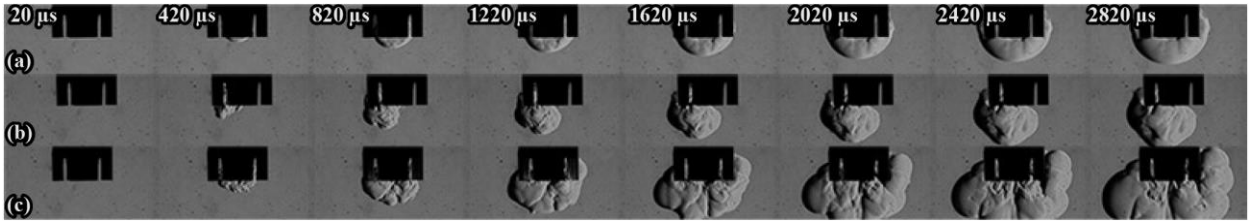

Figure 22. Comparison of flame-kernel growth: (a) inductive spark, (b) pulsed discharge with 5 pulses, (c) pulsed discharge with 20 pulses [62].

One of the biggest advantages of nanosecond-pulsed transient-plasma ignition is that it requires significantly lower energy (520 mJ for 20 pulses, [63]) in engine applications compared to the other transient-plasma corona ignition (4000 mJ) [32], which is also a system based on non-equilibrium plasma. Engine experiments with gasoline revealed that a nanosecond-pulsed plasma system can initiate rapid and stable combustion under extra-lean and highly EGR-diluted conditions [26, 63]. Significant improvements (20% in EGR-tolerance and 10% in lean-limit) are observed compared to conventional IDI igniters under a part-load condition of 1500 rpm, 5.6 bar IMEP [63].

The only potential disadvantage of this system, like any other technology exploiting non-equilibrium plasma, is that it relies on molecular-level collisions, so its effectiveness may diminish at higher in-cylinder pressures unless the provided electric field is increased proportionally to match the increase in particle density. It should be noted that this system and

the long-duration corona ignition reach non-equilibrium plasma conditions through different discharge characteristics. Hence, we expect the two systems to behave differently. The higher peak power outputs in this system could be beneficial for sustaining performance at elevated engine pressures.

Since nanosecond-plasma ignition is a very new technology, we have identified only Transient Plasma Systems (TPS) [70], a start-up company whose founders studied this technology in their graduate research, as a manufacturer. Although still early in its development, the TPS system has yielded promising experimental results in various reputable research laboratories, such as Argonne National Laboratory [63], Gundersen's laboratory at University of Southern California [26, 64], and Dibble's laboratory at University of California at Berkeley [62].

2.3.7 Summary of Surveyed Systems

A comparison of all the ignition systems that are surveyed can be found in Table 5. The systems are compared on the basis of 11 parameters, which are divided into three categories: (i) ignition characteristics, (ii) flame enhancement, and (iii) economic factors. Each ignition technology is given a qualitative grade relative to inductive-discharge ignition for each parameter, except for approximate total duration, which is quantitatively rated. If the igniter shows advantage relative to the baseline in a certain parameter, then it is awarded a "+" in that column. If the system is disadvantageous in terms of a parameter, then it is penalized by a "-" character. The more significant the advantage or disadvantage, the more symbols are added in the grade. If the system is neither advantageous nor disadvantageous, then it is given a "0." For the cases where sufficient information was not found, a "?" character is given. Finally, for the cases where there is a reasonable expectation of performance but no experimental data available, "+" or "–" symbols are added in parentheses following a "?" character.

Since different igniters follow different physical mechanisms, certain ignition characteristics need careful interpretation in order to meaningfully compare all the reviewed technologies in Table 5. For instance, majority of the igniters provide energy to the combustible mixture via plasma streamers (e.g. spark or corona). For all such systems, the delivered energy and approximate total duration are all defined based on the electrical discharge events. However, momentum-based approaches need to be interpreted differently, because their source of ignition for the main-chamber combustion is not plasma streamers but reactive jets. Hence, delivered

energy for these systems is defined as their jets' energy content. Total durations for igniters are also interpreted similarly. Streamer-based systems are rated by their electrical discharge duration, pre-chamber-systems are rated by their jet penetration durations, and Diesel-pilot ignition is rated by its ignition delay before autoignition.

Efficiency is defined as the system's capability of converting electrical energy into thermal energy directly input to the combustible mixture without heat losses. As was shown in Table 1, majority of the heat losses in a spark event occur during the glow discharge phase through the electrodes, whereas the most efficient energy release occurs during the breakdown phase. Therefore, systems that utilize faster discharge or non-equilibrium plasma are rated to be more efficient, because these technologies systematically avoid the glow discharge phase. Similarly, longer-duration igniters are rated to be less efficient due to the elongated glow discharge event.

For the igniters where no durability data was found, the expected durability was interpreted based on the ignition energy and duration information available. Typically, durability of an igniter's electrodes is closely linked to the duration of glow discharge and the amount of heat lost through them. Hence, durability is strongly correlated with the system's efficiency. Each system's total number of parts and overall complexity were also considered to be factors that can affect durability. For a more complete assessment for a particular device's durability, one needs to take material choice into account as well.

The most promising systems for ignition of CNG in heavy-duty engines in the near future are identified to be corona, transient-plasma, and turbulent jet ignition. All three of these technologies ignite a larger volume than conventional systems. There are other systems that can increase the ignition volume as well; however, they are either less effective or not as feasible as the above-nominated choices for the HECO-SING project. For instance, having multiple spark plugs is known to be effective, but this approach also requires a complete redesign of the engine head, which drives the costs up while increasing both cost and the risk of part failure. Diesel-pilot ignition is also a technology that has demonstrated improved performance, but it requires an additional fuel-storage and -delivery system for Diesel fuel. Concepts such as laser ignition or supersonic-jet ignition show promise, but they still need further development to be implemented into production or near-production engines. If the vibration patterns of a pre-combusted

supersonic jet are better understood and optimized in the future, for instance, then employing supersonic jet igniters might become feasible.

	Ignition Characteristics					Flame Enhancement			Economy	
	Energy Delivered (mJ)	Total Duration (ms)	Volume Ignition	Low Temperature	Pressure Tolerance	Efficiency	Early Growth	Mas-Burn Rate	Durability	Low Cost
Inductive Discharge	30 (0)	1	0	0	0	0	0	0	0	0
Capacitive Discharge	55 (0)	0.1	0	0	0	+	0	0	0	0
Dual-Coil	55-360 (+)	1-3	0	0	+	? (0)	+	+	-	? (-)
Bosch CEI	50-300 (+)	1-3	0	0	+	? (-)	+	+	? (-)	0
Breakdown	50 (0)	10^{-5}	0	-	+	++	+	0	-	0
Laser	50-400 (+)	10^{-5}	0	-	+	++	+	0	?	? (---)
Multi-Plug	50×*n* (+)	1	++	0	+	0	+	++	-	---
Rail-Plug	2500 (++)	0.2	+	0	0	-	+	+	---	0
Microwave Assisted	50 (0)	2.5	0	+	--	+	+	+	? (-)	? (--)
Corona	4000 (++)	0.5	++	+	? (-)	++	++	+	? (0)	? (-)
ns-Pulsed Plasma	500 (+)	0.5-2	+	+	? (-)	++	++	+	? (0)	? (-)
Turbulent Jet	+++	1-5	+++	?	+	?	+	++	? (-)	--
Supersonic Jet	+++	~1	+++	-	+	?	+	++	? (---)	? (--)
Diesel Pilot	++	~ 5	+++	0	++	?	+	++	-	---

Table 5. Comparison of the ignition systems surveyed. The baseline for the qualitative comparisons is inductive-discharge ignition, for which all the characteristics are graded with 0. + sign shows an advantage over the baseline, and multiple + signs indicate a greater advantage. The inverse is true for the – sign. The evaluation of ignition characteristics for jet and spray igniters are made based on the main-chamber air-fuel mixture ignition; for all the other igniters, discharge characteristics are considered. *n* is the number of igniters per cylinder for any given multi-plug system.

CHAPTER 3 EXPERIMENTAL SETUP AND PROCEDURE

3.1 Engine and Instrumentation

The parameters of the engine used for these experiments are summarized in Table 6. The Weichai WP10NG engine was modified to enable the various combustion modes needed for this project. It was originally capable of lean NG/air mixtures but had no external-EGR capability. A high-pressure EGR system with an EGR cooler and butterfly-type EGR-control valve was added. The EGR, air, and fuel, were mixed in a custom 3-gas mixer. The original turbocharger was replaced with one (Bosch Mahle Turbo Systems 110 Series) that provided higher backpressure to enable higher EGR rates.

Table 6. The specifications of the Weichai WP10NG engine.

Cylinder Configuration	Inline 6
Valves per Cylinder	2
Injection Type	Center-point, 12 injectors
Displacement (cm^3)	9,726
Bore x Stroke (mm)	126 x 130

The engine was run in a test cell with an AVL DynoExact dynamometer and AVL Puma Open control and data acquisition system. The cell included an air handler for conditioned combustion air with mass-flow measurement. The cell also included control of coolant temperature and charge air intercooler temperature. Instrumentation on the engine itself included many temperature and pressure sensors, including an AVL combustion pressure sensor in each cylinder, which were read by an AVL Indicom high-speed data-acquisition system. The dynamometer was equipped with high-resolution engine speed and torque measurement. Engine emissions were measured by Horiba MEXA benches sampling raw exhaust before and after the aftertreatment system and diluted in a full-size dilution tunnel. Intake CO_2 concentration was also measured for calculating the external EGR rate. All emission measurements reported here were made before the aftertreatment.

3.2 Exhaust-Gas Recirculation

In this work, the EGR rate is defined to be the ratio of background-corrected intake CO_2 concentration to background-corrected exhaust CO_2 concentration. The total dilution possible to deliver to the combustion chamber is a combination of EGR and excess air (lean combustion). The air system (including turbocharger, EGR plumbing and valve, charge air cooler, gas mixer, and intake manifold) has a practical limit on the maximum amount of EGR possible for a given quantity of excess air. When running a stoichiometric mixture ($\lambda = 1.0$), the turbocharger does not need to extract a significant amount of power from the exhaust gases, because of the lower boost requirements compared to lean operation. Therefore, this system can achieve up to 30% EGR rate at specific operating points. When running lean (i.e., $\lambda > 1.0$), the turbocharger consumes significant power from the exhaust gases, and the intake manifold pressure is much higher, as required to deliver the excess air to the combustion chamber. These factors limit the amount of EGR that is possible to push from the exhaust manifold to the intake manifold, to approximately 12% maximum, depending on operating point.

The measured EGR rate with the EGR valve completely closed was between 2% and 4%. This nonzero value results from residual CO_2 in the intake manifold from leakage past the EGR valve and possibly re-aspirated exhaust gases in the intake manifold. Thus, no operating conditions with 0% EGR were measured. The current configuration of the air system also limits maximum EGR rate. The concept of the project of which this work is a part is to determine how much dilution can be used with each of several ignition systems, with the goal to have increased engine efficiency and low engine-out emissions at an optimized high-dilution mixture. At some operating points, however, the air system does not have enough dilution capability to test the limit of the ignition system. For future work at all operating points, an air system with higher EGR or boost pressure capability would be recommended. This could be achieved with a multiturbocharger air system, a compressor, a variable geometry turbocharger, or a positive-displacement EGR pump could be utilized.

3.3 Ignition Systems

3.3.1 Conventional Ignition Systems

For the two conventional, IDI experiments described here, the engine was equipped with Bosch coils (functional samples not intended for production) that could deliver up to 140 mJ.

The coils allowed the dwell time (during which the coils are charged) to be adjusted for operation at 65 mJ (simulating the stock system) or at 140 mJ without a hardware change. The 140-mJ setting produced both a higher voltage and a longer duration, compared to the 65-mJ case.

3.3.2 Controlled Electronic Ignition

The third system was Bosch Controlled Electronic Ignition. The CEI discharge goes through the same breakdown, arc, and glow phases as any other spark-plug-based ignition system, but CEI uses a modified circuit producing an extended glow phase that is tunable in duration [20], as illustrated by the current-time cartoon in Figure 23. The current is nearly constant during the extended glow time and then decays in the normal way afterward. The glow times reported here are the extended glow times, which exclude the natural decay and thus underestimate the total glow-phase. The voltage-time curve [20] is more structured than the current-time curve; the voltage is 37-45 kV during the breakdown phase but drops to ~1 kV during the arc phase, after which it fluctuates with an amplitude of ~1 kV throughout the remainder of the discharge. The energy delivered by CEI was claimed by the manufacturer to be 50-300 mJ, depending on the dwell and glow times, which were separately adjustable over 0.4-1.6 ms and 0.3-5.0 ms, respectively. CEI is a proprietary, prototype system, so no additional detail on its inner workings are available. The initial voltage and spark duration produced by CEI is comparable to that of the 140-mJ IDI system; the additional energy (up to about 2 times as much) comes about because the voltage remains at the initial value throughout most of the spark event, rather than experiencing an exponential decay. This high-voltage, constant-current, long-duration discharge enhances Joule heating and reduces the risk of misfire, making CEI a good candidate for EGR-diluted, lean, low-cetane mixtures and cold starts. The potential drawbacks of CEI are increased heat losses through the electrodes and faster electrode erosion due to the longer spark duration.

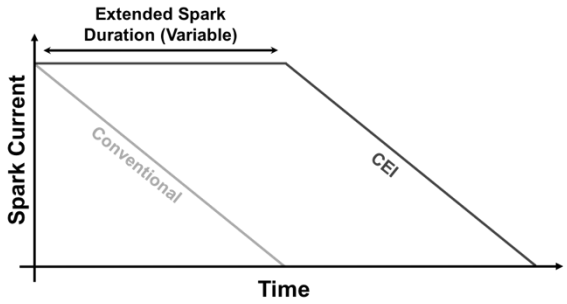

Figure 23. Schematic of the secondary-current behavior of the conventional and CEI system [71]. In courtesy of Dr. Michael C. Gross.

3.3.3 Corona Ignition

The fourth system tested was a high-frequency corona ignition system (BorgWarner EcoFlash). This system used bursts of a 3.16-MHz carrier with a peak-to-peak voltage of ~40 kV to produce non-thermal plasma streamers from the five tips on each igniter. The system's controller box (which sat between the engine control unit and the igniters) was configured via software (BorgWarner) and included settings for the duration of each burst of the carrier, number of bursts, pause between bursts, buck voltage (the voltage output by the controller before being stepped up by the transformer built into the igniter), and other parameters.

3.4 Optical Access and Imaging Equipment

The rearmost cylinder (Cylinder 6), being the most accessible, was modified to provide optical access for two cameras; two borescope sleeves were installed in the head, and reliefs were cut into the top of the piston to provide clearance for the tips of the borescopes. Figure 24 is a drawing of the engine, with cameras and associated hardware, viewed from two directions. Due to the limited options resulting from the positions of the valves, spark plug, ports, coolant passages, and intake manifold, the borescopes could not be positioned 90° apart; the angle between the borescopes, measured about the vertical axis, was ~70°. The relative positions and orientations of the borescopes and spark plug are clearly visible in Figure 25. Initial imaging showed reflections of the flame kernel from the piston. To reduce these reflections, the piston top and head were painted with flat black VHT Flameproof high-temperature coating.

The borescopes, sleeves, and related hardware were purchased from AVL. The AVL Visioscope M14 borescopes measure 7 mm in outside diameter, provide an angular field of view of 70°, and are optimized to focus light between 1.0 and 1.7 μm. The borescopes were cooled with air at ~6 bar pressure that was first passed through an AVL FU filter unit, which removed

particles that could clog the cooling channels. The borescopes were protected from the heat and pressure in the chamber by M14 sapphire windows. The cameras were rigidly held in place relative to the engine and borescopes using a combination of AVL-supplied brackets and custom-fabricated parts.

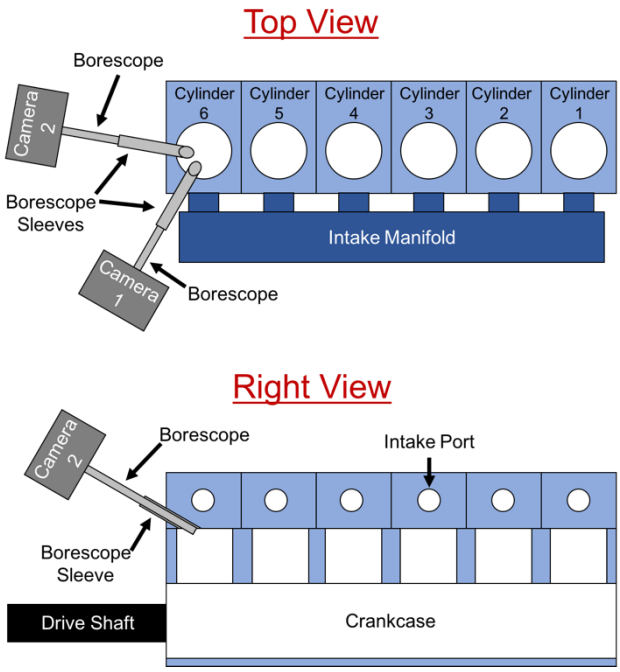

Figure 24. Drawings of the engine and optical equipment, viewed from two directions, showing the positions of the cameras and borescopes [72]. In courtesy of Dr. Michael C. Gross.

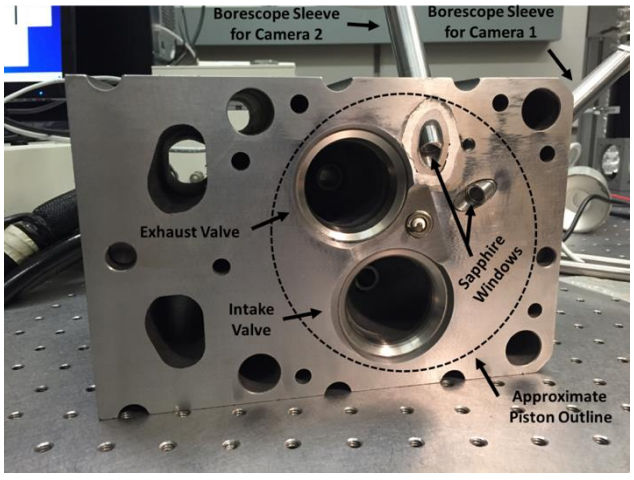

Figure 25. A photograph of the modified head with borescopes installed. Note the two views provided by Cameras 1 and 2 [72]. In courtesy of Dr. Michael C. Gross.

Each camera was a Xenics Cheetah-640-CL with the VisNIR option. The sensor chip has 640 x 512 monochrome pixels with 12 bits of depth, and it is sensitive to wavelengths between

400 nm and 1.7 μm (though maximum sensitivity occurs between 1.0 and 1.6 μm). While the borescopes do transmit visible light (the shorter end of the camera's sensitivity range), the focus is poor in the visible. A 1000-nm long-pass filter, placed between each camera and its borescope, was found to provide the best compromise between image brightness and clarity. The sensitivity of the camera annotated with the long-pass filter is shown in Figure 26. The camera can operate at frame rates up to 865 Hz in full-frame mode, but when only a subset of the sensor is used, much higher frame rates are possible. Preliminary imaging indicated that the field of view (FoV) provided by each borescope only occupied ~60% of the camera sensor in each dimension, so both cameras were windowed to 384 x 336 pixels in order to increase the maximum frame rate beyond 1 kHz without sacrificing any useful information.

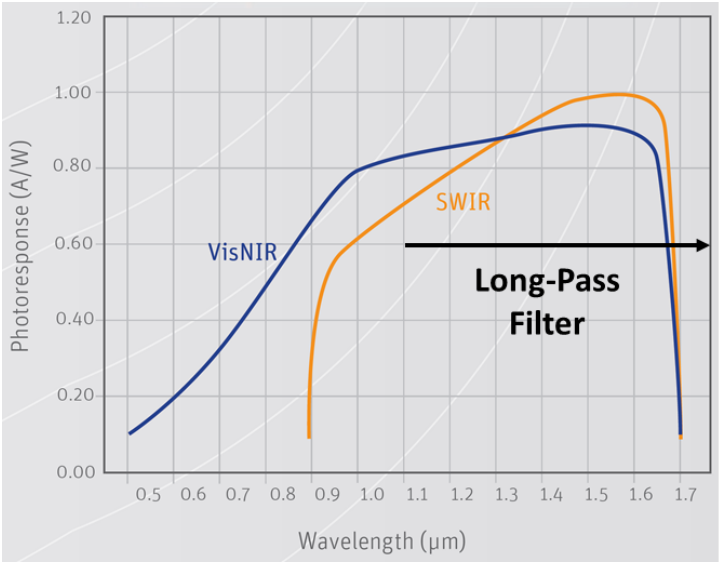

Figure 26. Cheetah-640-CL camera sensitivity as a function of wavelength. VisNIR (blue) option is used with a 1000-nm long-pass filter.

One-per-cycle and 1440-per-cycle signals were provided to a LaVision PTU-X programmable timing unit, which in turn triggered the cameras to capture images. One instance of LaVision Davis 8 was used to program the timing unit and record images from Camera 1; a second instance of DaVis captured images from Camera 2.

3.5 Engine Calibration

It was necessary to determine the maximum air/fuel ratio and EGR dilution for each operating point, as lean combustion is desired for improving fuel efficiency, and EGR dilution is desired for improving both efficiency and NO_x emissions. This dilution amount was determined

by setting an upper limit on the CoV(IMEP) for each individual cylinder of between 6-8%. It should be noted that, despite the modifications for optical access, Cylinder 6 did not suffer the most CCV. The worst CoV(IMEP) values were those of Cylinders 3 and 4, the middle two cylinders. It is speculated that imperfect air/fuel mixing in the intake manifold may have resulted in less well-mixed or globally leaner mixtures reaching these two cylinders, leading to less consistent cycle-to-cycle combustion. The IMEP and CoV(IMEP) values reported here are for Cylinder 6 specifically.

For each operating point defined by engine speed, load (IMEP), air/fuel ratio, and EGR rate, the spark timing was adjusted to position the crank angle at which 50% of the fuel (by mass fraction) has been burned, MFB_{50}, at approximately 9 crank angle degrees after top dead center (°aTDC) for the entire engine. (Throughout this document, MFB_x refers to the crank angle at which *x*% mass fraction of the fuel has been consumed.) This target value was determined from engine mapping with ignition timing sweeps at various operating points as the MFB_{50} that minimized the brake specific fuel consumption.

3.6 Data and Image Acquisition

Before comparing the four ignition systems, the operating points summarized in Table 7 were examined with only CEI in order to understand the effect of the glow and dwell times on ignition and to select the values that would be used for the comparison. Only durations on the long end of the range for each parameter were used, based on guidance provided by the CEI engineers at Bosch. These engineers stated that shorter durations did not yield reliable ignition while longer durations did not improve combustion. Based on the outcomes of these preliminary experiments, described below in the Results and Discussion section, the dwell and glow time were set to 1.0 and 3.0 ms, respectively, for all later experiments.

The operating conditions for directly comparing all three Bosch ignition systems are summarized in Table 8. The operating conditions with the corona igniter in comparison to 65-mJ igniter are summarized in Table 9. At each operating point, the in-cylinder pressure and images were recorded over a 100-cycle period. The statistical metrics reported here were computed from these 100-cycle measurements. Images were recorded at intervals of 5.5 CAD, equivalent to a frame rate of 1.09 kHz. For each operating condition, multiple measurements were made, each with a different timing offset (multiples of 0.5 or 1.0 CAD, depending on the experiment). This image recording process is illustrated in Figure 27. Due to CCV, the images cannot be simply

interleaved to fill in the gaps in the imaging. However, since 100 cycles of images were recorded at each offset, these images can be used to provide statistical information at 0.5- or 1.0-CAD resolution, as will be described in the next section. Images were recorded from just before ignition to the point at which the FoV was filled with flame. Operating points that were lean or diluted necessitated earlier ignition timing and burned later, thus longer imaging periods were required.

Table 7. The conditions tested and the parameters measured during set up of the CEI system. The engine speed and IMEP were 1000 rev/min and 6.8 bar. Each column is color-coded from red (the lowest value) to blue (the highest) [71].

Ignition System	Air/Fuel Equiv. Ratio	EGR [%]	Ignition Timing [^{o} aTDC]	Dwell Time [ms]	Glow Time [ms]	Ignition Delay [CAD]	Comb. Duration [CAD]	CoV(IMEP) [%]	BS HC [g/kW-hr]	BS NO_X [g/kW-hr]	BS CO [g/kW-hr]
CEI	1.5	16	-47.25	1.0	0.5	46.1	32.1	1.96	4.60	1.12	2.71
					3	46.1	33.8	1.76	4.57	1.15	2.67
				1.2	0.5	46.1	32.3	1.71	4.53	1.15	2.61
					3	46	35.1	1.63	4.46	1.22	2.53

Table 8. The operating conditions tested and parameters measured with all ignition systems except corona. The engine speed and IMEP were 1000 rev/min and 6.8 bar. Each column is color-coded from red (the lowest value) to blue (the highest) [71].

Ignition System	Air/Fuel Equiv. Ratio	EGR [%]	Ignition Timing [°aTDC]	Ignition Delay [CAD]	Combustion Duration [CAD]	CoV(IMEP) [%]	BSFC [g/kW-hr]	BS HC [g/kW-hr]	BS NO_x [g/kW-hr]	BS CO [g/kW-hr]
65 mJ	1	3	-18.75	19.77	15.21	0.27	227.3	1.68	11.15	23.48
		23	-46.5	40.99	29.87	0.56	217.4	3.85	2.00	22.73
	1.6	2	-33	33.13	26.6	1.09	201.9	3.93	3.27	2.27
		10	-52.5	52.01	34.08	2.69	204.9	6.88	1.08	4.14
140 mJ	1	3	-19.5	20.15	15.44	0.32	224.6	1.63	10.93	23.45
		23	-45	40.99	31.07	0.51	215.4	3.32	2.55	22.38
	1.6	2	-35.25	34.56	26.6	0.88	201.1	3.59	4.41	2.26
		10	-55.5	53.91	33.59	1.6	203.2	5.46	1.92	3.41
CEI	1	4	-19.5	20.42	15.59	0.32	226.8	1.41	8.54	17.45
		23	-43.5	39.88	28.74	0.5	217	3.47	2.04	20.53
	1.6	2	-36	35.58	27.27	1.14	201	3.73	2.49	2.08
		10	-54	52.94	36.61	2.44	203.6	6.85	1.35	4.00

The camera integration time was chosen to provide the best signal-to-noise ratio for each operating condition; these times ranged from 10 to 20 μs, much shorter than the frame period of 920 μs. The cameras did not offer the capability of changing the integration time during the engine cycle, so the chosen integration time was necessarily a compromise between sensitivity during the very early flame development and ability to image late in the cycle before being overwhelmed by saturation. Because saturation occurred in later images (beginning around $MFB_{00.5}$), it was not possible to correct for different exposure times by simple multiplication of the counts in each pixel; all that is known about the saturated pixels is that the number of counts generated is greater than or equal to the maximum possible for the camera, so multiplying them to below-saturation levels would be misleading.

Table 9. Engine operating conditions and parameters measured. Engine speed was 1000 rev/min; IMEP was 6.8 bar. Cases with 3% EGR occurred with the EGR valve closed [73].

Ignition System	Air/Fuel Equiv. Ratio []	EGR [%]	Spark Timing [°aTDC]	mean($MFB_{00.5}$) [°aTDC]	Ignition Delay [CAD]	Comb. Duration [CAD]	CoV(IMEP) [%]
65 mJ	1.0	3	-18.75	-2.51	16.5	15.2	0.3
	1.6	10	-52.50	-6.11	47.1	34.1	3.0
Corona	1.0	3	-13.35	-2.01	11.7	15.0	0.4
	1.6	10	-35.10	-7.85	27.7	30.7	1.9

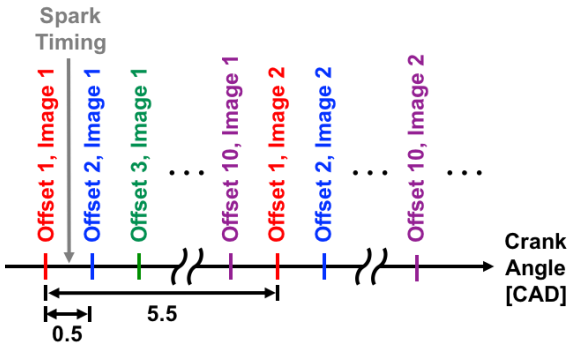

Figure 27. An illustration of the crank angles at which images were recorded. Images from each subset were recorded in a single measurement. Successive subsets were recorded in successive measurements moments later [72]. In courtesy of Dr. Michael C. Gross.

3.7 Image Processing Algorithms

Image processing is required to detect the location of the flame boundaries accurately, and to eliminate background noise and other interfering signals from in-cylinder reflections. Several image processing strategies are described in this chapter.

3.7.1 Otsu's Method

Otsu's method identifies an intensity threshold in a grayscale image that accurately separates the foreground and the background of an image [74]. A grayscale image is an array of discrete values from 0 to $2^n - 1$, where n is the number of bits and the value is the pixel intensity. Each pixel intensity is sorted into an intensity histogram that represents the image. In

an image, with a distinct foreground and background of relatively equal size, the histogram creates two distinct peaks at a low and high intensity. The image is then split into two classes which represent the foreground and background. The inter-class variance is measured, and where that value is maximized is the appropriate intensity threshold for the image. The benefit of this method is that it creates a global threshold that is unique to each image. Global thresholds tend to be more robust against local noise than a locally calculated threshold. Two sample image flame images are shown in Figure 28, and their histograms are shown in Figure 29 and Figure 30.

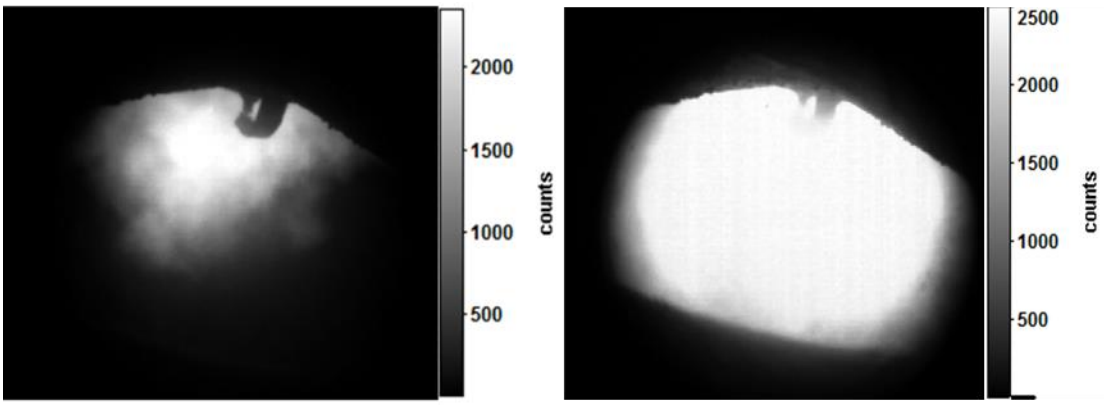

Figure 28. Sample raw images used to create histograms in Section 3.7.1.

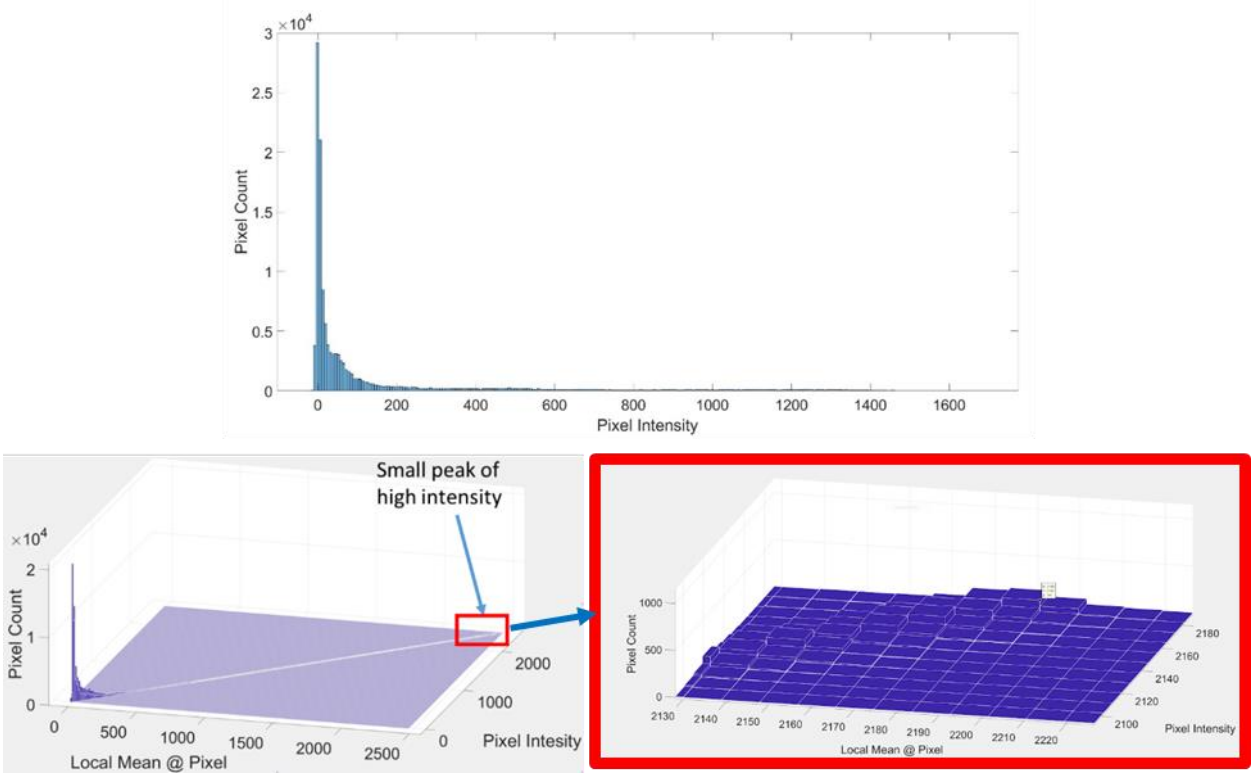

Figure 29. Shown are three histograms associated with the raw image of the small flame (left) in Figure 28. Top: The intensity histogram used in the original Otsu's method. Note that there is no

high intensity peak for Otsu's method to identify. Left: 2-D histogram where axis are the local mean of each pixel, the pixel intensity and the number of pixels that fall at each x-y coordinate. Right: Enlarged view of the high intensity peak that is identified with Otsu's 2-D method which could not be identified with the original Otsu's method. In courtesy of Margaret Poppe.

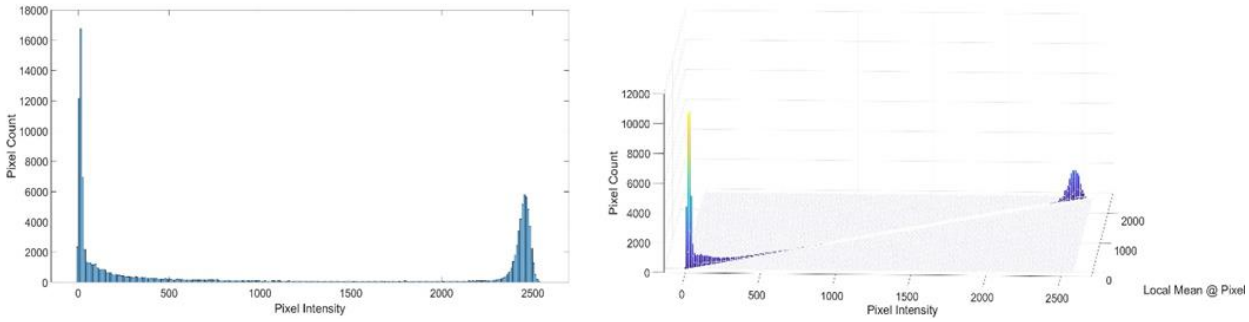

Figure 30. Shown are the results of the histogram of the large flame image (right) in Figure 28. Unlike the smaller flame image histograms shown in Figure 12, the high intensity peak is more defined in both the original histogram and the 2-D histogram. However, the high intensity peak decreases in size in the 2-D histogram because noise that was sorted into the 1-D intensity histogram is moved away from the true intensity peak. In courtesy of Margaret Poppe.

Implementation of Otsu's method in flame thresholding application is not sufficient without user input. Otsu's method requires two distinct peaks to identify a threshold that maximizes the inter-class variance. There are three key features of our images that prevent the formation of two distinct peaks. First, the noise in our images raises the center region of the histogram, which relatively decreases the two peaks. Second, the small size of the flame compared to the background decreases the size of the high intensity peak. Finally, the gradient of intensity in the flame distributes the high intensity peak over a wider region, which further decreases the size of the high intensity peak. To overcome this lack of two distinct peaks, the user defines multiple thresholds for the image, then selects the threshold that most accurately sets the intensity threshold. So, instead of two classes, there are three, four, or five classes depending on the image being thresholded.

While his method generates a threshold between the background and foreground intensity, it is subjective. The subjectivity of the images yields more subjective results and significantly increases the time needed to process the images. Therefore, the following algorithms have been surveyed or developed to study flame images.

3.7.2 Two-Dimensional Otsu's Method

Two-dimensional Otsu's method combines a measure of pixel intensity as well as the features of the surrounding pixels [75]. By combining both types thresholding methods, it is easier for a computer to set an accurate threshold with a noisy image.

Two-dimensional Otsu's method uses the pixel intensity histogram that Otsu's method uses on one of the two axis. The second axis of the histogram is the local mean at each pixel. To create this histogram, the mean of an SxS region surrounding a pixel is stored at that pixel location. Then, the local means of each pixel are sorted into a histogram with the same number of bins as the intensity histogram. At this point, each pixel is associated with a bin in the intensity histogram and the local mean histogram and they are combined into a two-dimensional histogram. In the two-dimensional histogram, the x-axis is the pixel intensity, the y-axis is the local mean of the pixel and the z-axis is the number of pixels located at each x-y coordinate. Figure 31 shows the process by which pixel in the bottom right is sorted into its location in the 2-D histogram. After creating the two-dimensional histogram, the histogram is sorted into 4 classes with a threshold on each axis. The classes are measured for variance and the maximum inter-class variance for both axis determined the threshold. Then, the threshold on the intensity axis is applied to the image to produce a thresholded image.

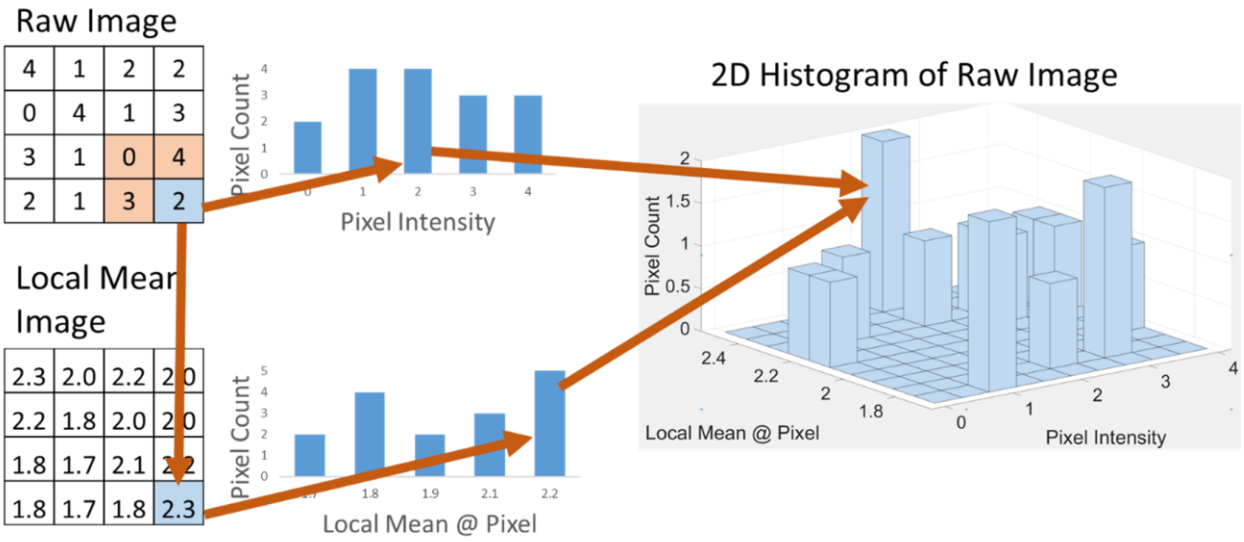

Figure 31. 2-D Otsu's method sorts pixels based on an x-y coordinate where x is the bin from the intensity histogram and y is the bin from local mean histogram. This example shows how the sample pixel in the bottom right of the raw images is sorted into the intensity histogram, the local mean histogram and then it's location in the final 2-D histogram for the sample image. In a larger image, two distinct peaks begin to form at the (high intensity, high local mean) and the (low intensity, low local mean). In courtesy of Margaret Poppe.

Flame image tests showed significant improvement with 2-D Otsu's method over 1-D Otsu's method, especially with the small flame kernels. When the signal to noise ratio is low, 1-D Otsu's method picks up a large portion of the noise as the foreground, whereas 2-D Otsu's method can avoid majority of the noise.

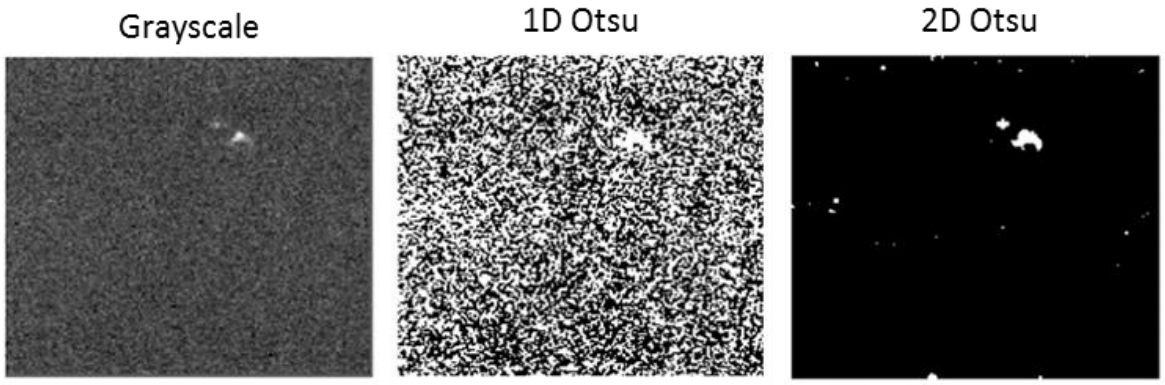

Figure 32. Comparison of binarization performance of standard 1-D and 2-D Otsu algorithms on a very early (9.5 CAD after ignition) flame kernel under lean (λ=2) and 10% EGR-diluted, 1000 RPM, 6.8 bar IMEP conditions. 2-D Otsu's method performs significantly better for this image with low signal-to-noise ratio.

In order to improve the thresholding quality in flame imaging applications further, three different algorithms are developed and tested based on 2-D Otsu's method.

3.7.2.1 Quartering Method

The background intensity distribution produced from 2D Otsu thresholding is often asymmetrical with a positive skew, as shown in Figure 33. The degree of this skew varies significantly with crank angle. One consequence of this varying skew is changes in the shape of the histogram curve between its highest peak and 2D Otsu's intensity threshold. Triangular thresholding techniques, and other binarization methods that use some characteristics of this portion of the histogram, such as the point of minimum curvature, will often result in binary images that include portions of the true background in their foreground.

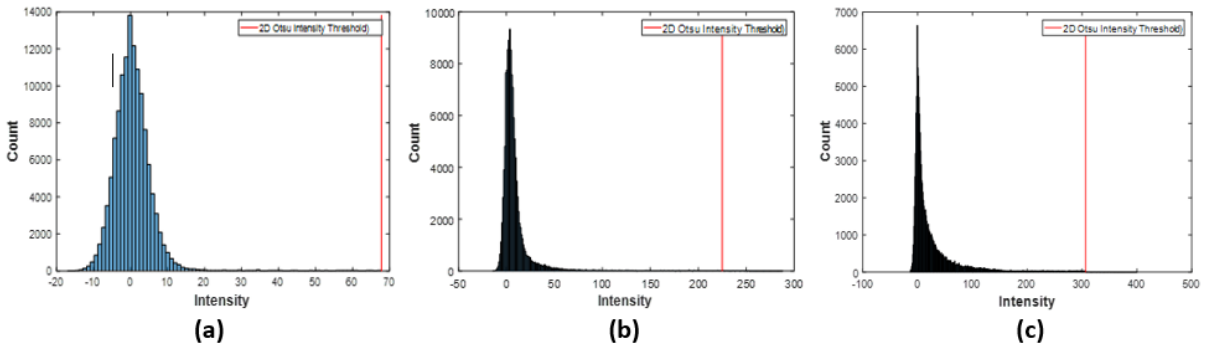

Figure 33. 2D Otsu's Method results in characteristically different background intensity distributions for varying flame kernel sizes. As flame kernel size increases from a to c, the positive skew within the background becomes more extreme. This progression presents difficulties developing automatable thresholding techniques. In courtesy of Caleb Sherwood.

The Quartering Method is based upon two assumptions about the background intensity distribution that is created from 2D Otsu thresholding. The first assumption made is that the background intensity distribution produced from 2D Otsu thresholding will be approximately unimodal. This unimodal distribution may be either positively skewed or asymmetrical. The second assumption made is that the intensity i_{true}, which represents both the highest intensity of the true background distribution, and the proper intensity threshold for separating a grayscale image into its true foreground and true background, occurs at some intensity i between the beginning of the upper tail of the background intensity histogram and i2D-Otsu, where i2D-Otsu represents the intensity threshold set by 2D Otsu's method. The overall goal of the Quartering Method is to outline the shape of the asymmetrical portion of the background intensity histogram (if such a portion is present) with a continuous curve, calculate the first derivatives of this curve with respect to intensity, and place i_{true} at the lowest intensity at which these first derivatives become constant and negligibly small in magnitude.

In Quartering Method, after performing 2D Otsu's thresholding, a histogram is produced for the intensity distribution of the resulting background. A smoothed, continuous curve, $y(i)$, is produced to outline the shape of the histogram, where $y(i)$ is the pixel count corresponding to intensity i. Another curve, $T(i)$, is then produced to outline the asymmetrical portion of the background intensity histogram, beginning at $i = i_{min} + 2i_{peak}$, where i_{min} is lowest intensity in the background distribution, and i_{max} represents the intensity at the maximum value of y(i) (which is assumed to be at the peak of the background distribution). Distributions of the magnitudes of the first and second derivatives of $T(i)$ with respect to intensity i are produced, along with the

median and third quarter of the first derivative magnitude distribution, $(|T'(i)|)_{median}$ and $(|T'(i)|)_{thirdQuarter}$.

The intensity domain of $T(i)$ is then broken into four equal portions, notated ($Q_{1...}$ Q_4), and the median first and second derivative magnitudes of each of these portions are calculated. Intensities i_1 … i_4 are used to describe the intensities at the end of each quarter. The first of these quarters with a median first derivative magnitude that is lower than the average of $(|T'(i)|)_{median}$ and $(|T'(i)|)_{thirdQuarter}$ is selected, and notated as Q_m. An intensity i_m, corresponding to the maximum value of $T''(i)$ within Q_m, is found and the intensity threshold is then adjusted such that it is equal to $(i_m + (i_m - i_{m-1}))$. The grayscale image is then binarized using this new, single threshold for intensity. A sample image background intensity distribution with key quartering method parameters are shown in Figure 34.

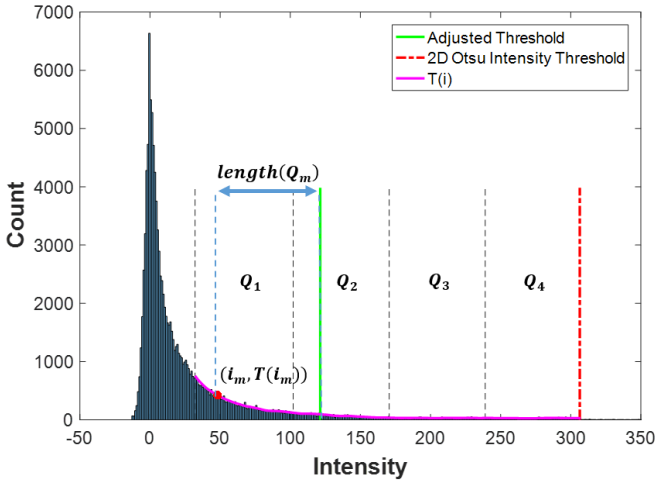

Figure 34. A background intensity distribution created from 2D Otsu's thresholding. The Quartering Method breaks the upper tail of the background intensity distribution, defined by curve T(i), into segments, which are notated as Q1… Q4. It then compares the first and second derivative characteristics within each segment to the derivative characteristics of the entirety of T(i). This process helps to include portions of the true foreground that are often cut off by 2D Otsu's method. In courtesy of Caleb Sherwood.

In larger flame kernels, this thresholding method provides a robust way of placing low-intensity regions of the true foreground, that 2D Otsu's method often places in the background, into the foreground of binary images. However, in images with extremely skewed background intensity distributions, the Quartering Method will place portions of the true background within the foreground. This makes the quartering method susceptible to reflections and other sources of corruption which greatly alter the background intensity distributions.

3.7.2.2 Ordinary Differential Equation Solution Fit Method

As an effort to address the issues of consistency within the quartering method, ordinary differential equation (ODE) solution fit method is proposed. Similar to the Quartering Method, the ODE Fit Method uses a continuous curve to outline the shape of the background intensity distribution, and estimate where the curve becomes approximately constant with respect to intensity. However, whereas the Quartering method works by breaking the intensity range of the background distribution into segments, and analyzing derivative characteristics within each segment, the ODE Fit Method fits the solution to a first order differential equation to the upper tail of the background intensity histogram.

After performing 2D Otsu's thresholding, a histogram is produced for the intensity distribution of the resulting background. A continuous curve, $y(i)$, is produced to outline the shape of the histogram, where $y(i)$ is the pixel count corresponding to intensity i. The intensity at which $y(i)$ is maximal is notated $i_{max,\,y}$, and the intensity value representing the third quarter of the background intensity distribution is notated $i_{thirdQuarter}$. A second curve, $T(i)$, is then created to describe the asymmetrical portion of the background intensity distribution, with $T_0(i)$ occuring at $\frac{2i_{max,y}+i_{thirdQuarter}}{2}$. Numerical first derivatives of $T(i)$ with respect to intensity are calculated, and these values are used to produce a first order differential equation (ODE) of the form $\frac{dT}{dt} = A \times T(i) + B$, where A and B are constants. The solution to this differential equation is notated $T_{est}(i)$. To approximate where $T(i)$ becomes constant with respect to intensity, the first derivative of $T_{est}(i)$ at i_0, $T_{est}'(i_0)$, is used to produce a parameter τ that describes the exponential change in $T_{est}(i)$ with respect to intensity. The value of $\tau - i_0$ functions in a way similar to a time constant of a linear time-invarient system. $(\tau - i_0)$ represents the change in intensity required to decrease $T_{est}(i_0)$ to a value of zero at a rate of $T_{est}'(i_0)$. The exponential behavior of $T_{est}(i)$ results in an actual decrease to $\frac{1}{e}T_{est}(i_o)$ over this change in intensity values. Hence, τ is identified as the intensity at which $T_{est}(i)$ is equal to 36.8% of $T_{est}(i_0)$. At an intensity value of $i_0 + 4(i - i0)$, first derivatives of $T_{est}(i)$ are assumed to become negligible, and the intensity threshold $i_{threshold}$ is then adjusted such that it is equal to $i_0 + 4(i - i0)$. A sample image background intensity distribution with key ODE solution fit parameters are shown in Figure 35.

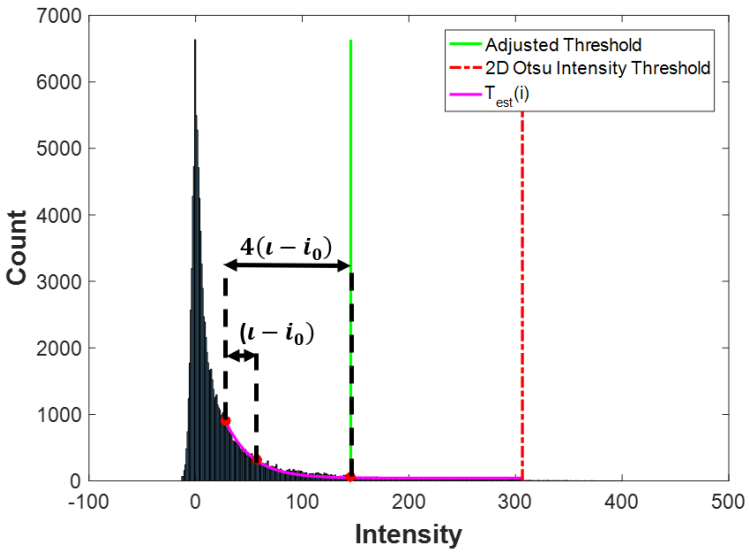

Figure 35. The ODE fit method uses a first order differential equation to characterize the shape of the upper tail of the background intensity distribution. Test(i) is the solution to this first order differential equation. In courtesy of Caleb Sherwood.

The ODE fit method produces more consistent results than quartering method. However, in cases of significant reflections or other sources of corruption, the tail of the background intensity distribution can often not be reasonably described with a first order differential equation, and the application of this thresholding technique may not produce reasonable results.

3.7.2.3 Gradient Thresholding Method

In order to address the cases where the image intensity distribution cannot be accurately estimated with a first order ODE, gradient thresholding method is developed. In this method, the grayscale image is smoothed through use of a moving average, and a three dimensional projection of the image is produced by making the moving average intensity of the grayscale image a function of pixel indices, notated *F(x,y)*, with origin *(0,0)* located at the the top left corner of the image. The x and y components of the two-dimensional numerical gradient, $\partial F/\partial x$ and $\partial F/\partial y$, respectively, are used to calculate the magnitude of the numerical gradient of *F(x,y)* at each pixel. The values of these numerical gradient magnitudes are notated as *G(x,y)*.

The surface-normal vectors of *G(x,y)*, along with an angle α, the angle that the normal vector of *G(x,y)* makes with the positive z axis, are calculated at each pixel location. A distribution of all α angle values (one for each pixel in image) is produced, and the α angle value corresponding to the maximum inter-class variance is calculated using standard Otsu's method. This threshold calculated from this 1D Otsu's step is notated $\alpha_{threshold}$. The image is binarized

using this angle threshold, rather than an intensity value. Pixels with an angle greater than $\alpha_{threshold}$ are given a binary value of 1, and all other pixels are given a binary value of 0.

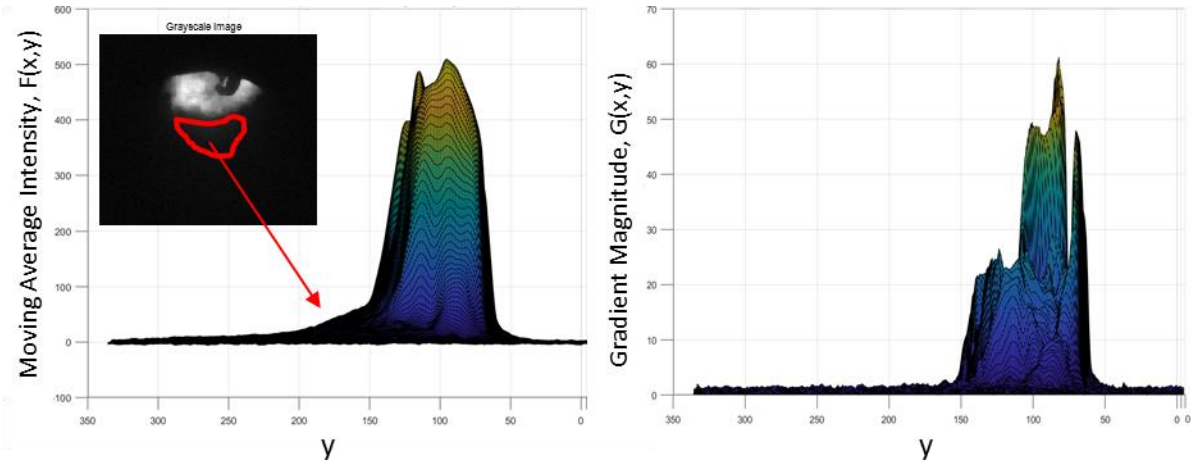

Figure 36. There are often shapeless, high-intensity regions within the grayscale image, resulting from reflections or improper exposures that do not belong to the flame kernel. The difference between values of G(x,y) at these pixel locations, and the values of G(x,y) at the edges of the flame kernel, are proportionally larger than the difference in values of F(x,y) at these two respective locations. Thus, analyzing G(x,y) during the thresholding process, rather than F(x,y), makes it easier to exclude these regions from the foreground. In courtesy of Caleb Sherwood.

Creating a binary image using threshold will typically create an image that ensures that the entirety of the flame kernel is included within the foreground. However, the flame kernel boundaries of the binary image can be rounded and imprecise. To more accurately define the flame kernel boundaries, one more intensity distribution is analyzed, consisting of all pixel intensity values that have an α value greater than $\alpha_{threshold}$, but intensity and moving average intensity values that are not both greater than their respective thresholds from the initial 2D Otsu iteration, $i_{threshold}$ and $(\bar{\imath})_{threshold}$. Standard Otsu's method is performed on this intensity distribution, and the resulting intensity of maximum inter-class variance is defined as the new threshold for the grayscale image, $i_{adjustedThreshold}$. If the value of $i_{adjustedThreshold}$ is lower than that of the original threshold set by 2D Otsu's method, $i_{threshold}$, the grayscale image is binarized again, this time using $i_{adjustedThreshold}$.

The main advantage of the gradient method is that it is capable of excluding reflections that are near the same intensities as the true flame kernel boundaries. This results in it being the most dependable of the explored thresholding techniques in terms of including low-intensity regions of larger flame kernels within the foreground. Although automatable, it is more computationally expensive to process images than the Quartile or ODE Fit methods.

Gradient thresholding method with two sample flame images with the intermediate $\alpha_{threshold}$ step is shown in Figure 37.

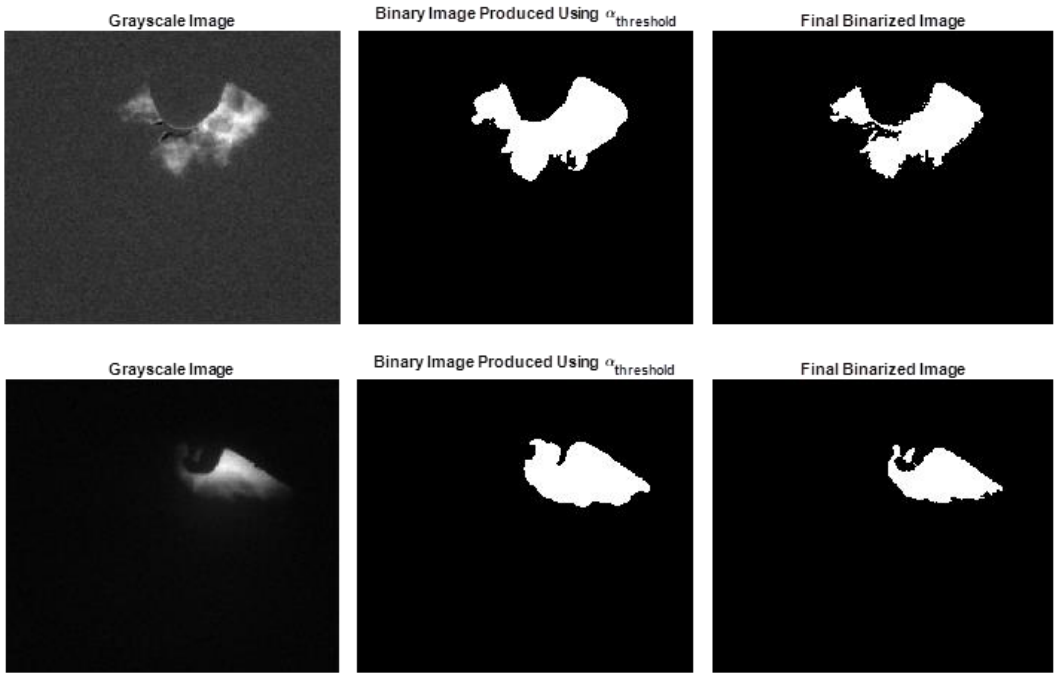

Figure 37. General process of the gradient thresholding technique is summarized here. Two binary images are created, the first using $\alpha_{threshold}$ on the distribution of angle α values, and the final binarized image being produced from an analysis of pixels that are included within the foreground of the angle α binary image, but that were placed in the background by the initial 2D Otsu intensity thresholding.

3.7.3 Noise Removal

Thresholding algorithms discussed in Sections 3.7.1 and 3.7.2 remove majority of the noise and can detect the flame in the foreground. However, especially with the low signal-to-noise ratio images, which are typically early flame kernels under lean and diluted engine conditions, some portion of the noise remains in the binarized image. In order to clear up that remaining noise, connected binarized pixels in the image are defined as objects, and objects that are smaller than a pre-determined size are regarded as noise and erased. Figure 38 demonstrates this noise removal algorithm, and a sample noise removal from a binarized flame image is shown in Figure 39.

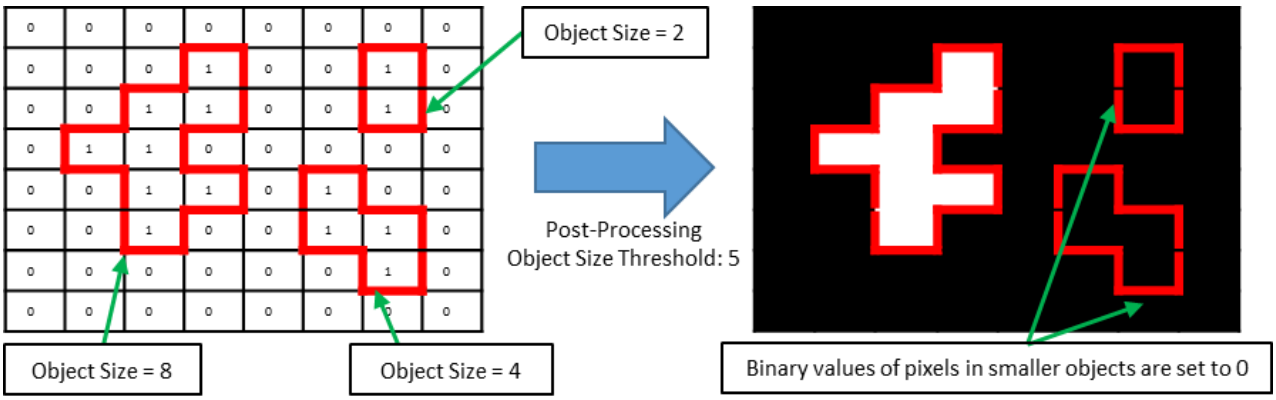

Figure 38.Demonstration of noise removal algorithm. Binarization algorithm does not remove all the noise. In this example, object sizes below 5 pixels are detected as noise and automatically removed. In courtesy of Caleb Sherwood.

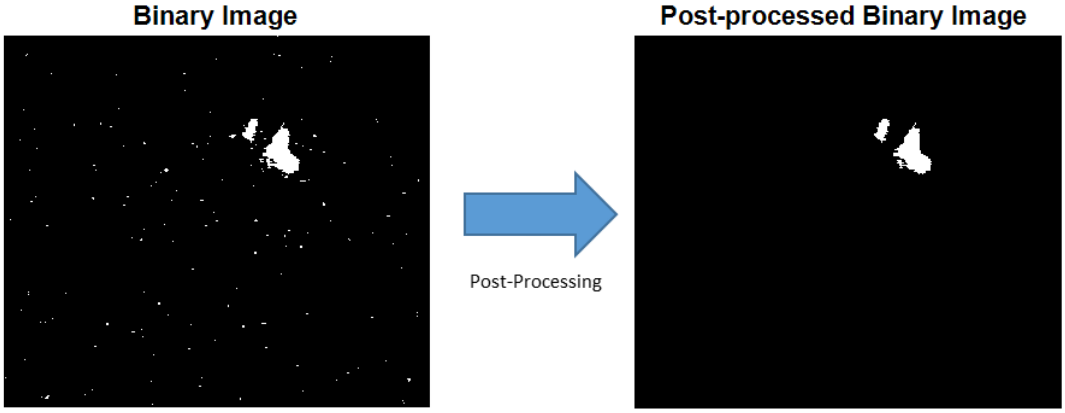

Figure 39. Sample noise removal post-processing on a binarized image. In courtesy of Caleb Sherwood.

3.7.4 Assessment of Methods

A list of processed images by each thresholding method discussed in Section 3.7 is shown in Figure 12. Images from three different igniters (65 mJ, 140 mJ, corona) are shown to illustrate the applicability range of these techniques. For each case, gradient method has yielded the best results, as it captured sharply captured the edges of the flame even at the lowest signal locations.

Additionally, a summary of the advantages and the disadvantages of each technique is provided in Table 10.

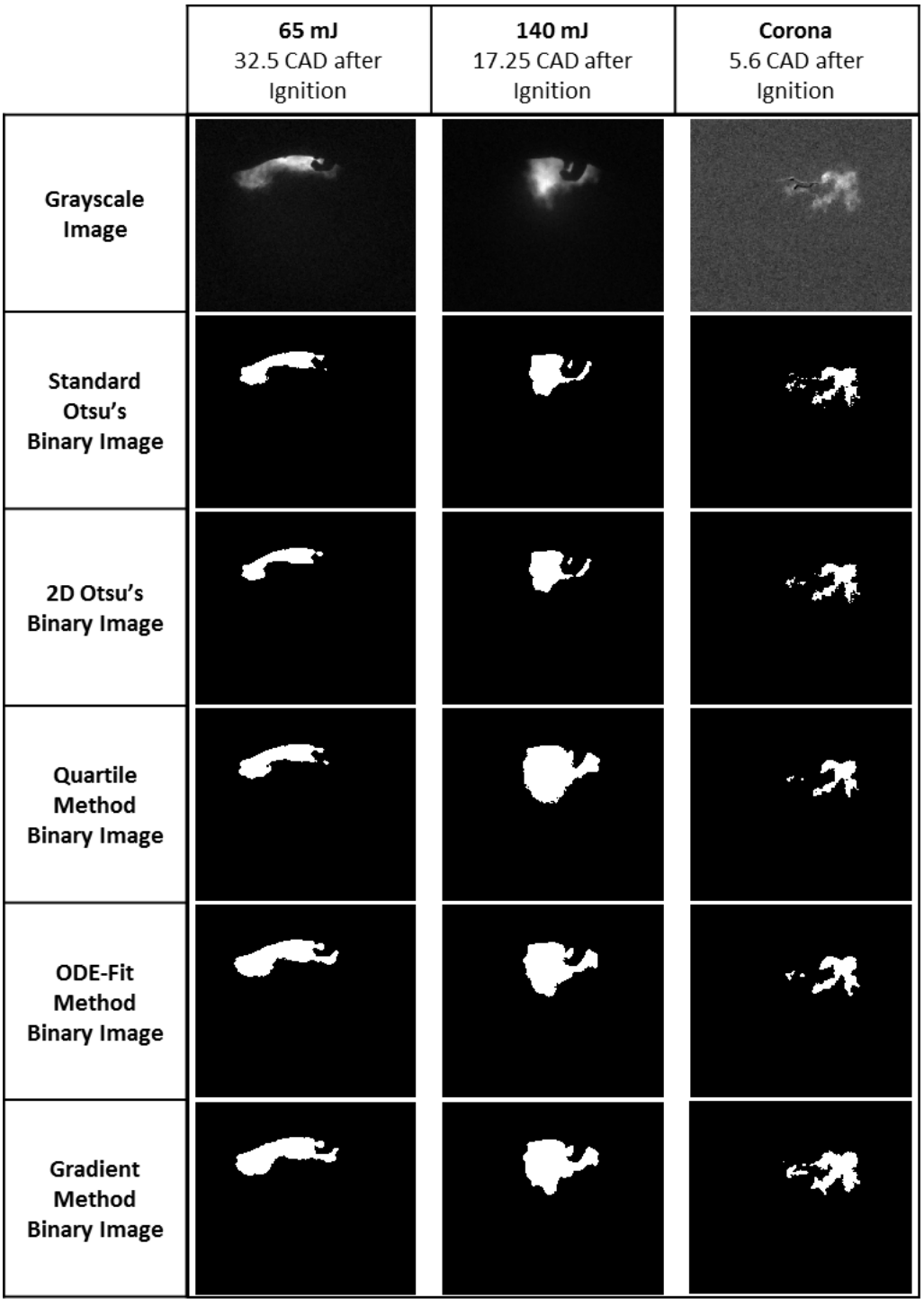

Figure 40. Image processing results for all the algorithms discussed for three sample images of flame kernels ignited by a 65 mJ, a 140 mJ, and a corona igniter under λ=1.6, 10% EGR, 1000 RPM, 6.8 bar IMEP engine operating conditions. In courtesy of Caleb Sherwood.

	Advantages	Disadvantages	Runtime per 100 images (s)
1D Otsu	Computationally quick and simple.	Cannot handle small images with foregrounds and low signal-to-noise ratio well. Requires user input to define the number of thresholds for a given image set.	41.8
2D Otsu	Capable of distinguishing foregrounds when its size is significantly smaller than the size of the background. Can distinguish the foreground in images corrupted by noise.	Cannot handle images with low signal-to-noise ratio. When the flame kernels are larger and there is variation of intensity within the flame kernel itself, maximizing interclass variance erroneously assigns lower-intensity regions of the flame kernel as part of the background.	46.1
Quartile	Provides robust way of including low-intensity regions of the flame kernel within the foreground. Accounts for asymmetry and abnormalities in intensity distributions, which may occur on an individual-image basis.	Lower precision than the other thresholding methods. Sometimes picks up regions of reflections/background that have intensities that are close to or higher than the intensities within the flame kernel.	67.3
ODE Solution Fit	Includes low-intensity regions of the flame kernel within the foreground. More precise than the quartile method, and yields more consistent results.	Does not account for individual images with particularly strong reflections in the background. In such cases, the background intensity distribution may not be accurately described by a first order differential equation.	49.2
Gradient Thresholding	Capable of removing reflections with varying intensity that are difficult to account for with the other methods. Analyzes a larger number of characteristics of the background and foreground than other methods, which allows it to more effectively distinguish the highest intensities of the true background from the lowest intensities of the flame kernel.	Computationally expensive.	179.8

Table 10. Assessment of each method is given.

3.8 Image Analysis

The view of the top of the flame was more obstructed by the head in Camera 2's images, making computing metrics from these images more challenging. These computations are still being developed, so only images and metrics from Camera 1 are reported here.

The image-processing procedure, illustrated in Figure 41, was carried out with a combination of LaVision DaVis and MathWorks MATLAB. Although the cameras have monochrome sensors, false color was applied in many images presented here to aid the reader's eye. The first image in Figure 41 is the raw image recorded by Camera 1 at 1000 r/min, 6.8 bar IMEP, $\lambda = 1.0$, and 3% EGR. A background image (not shown), recorded immediately before ignition (as indicated in Figure 27), was subtracted, reducing noise and yielding the second image. A median filter with a 3x3-pixel window was applied to smooth the image without compromising the edges as much as a Gaussian filter, yielding the third image. Even with the piston painted matte black, reflections from the piston were still visible in some cases. To reduce these reflections, Otsu's method of thresholding [74] was applied. Values below the threshold were set to 0; those above were set to 1, resulting in the fourth image. The median-filtered image was multiplied by the binarized image to create the thresholded final image.

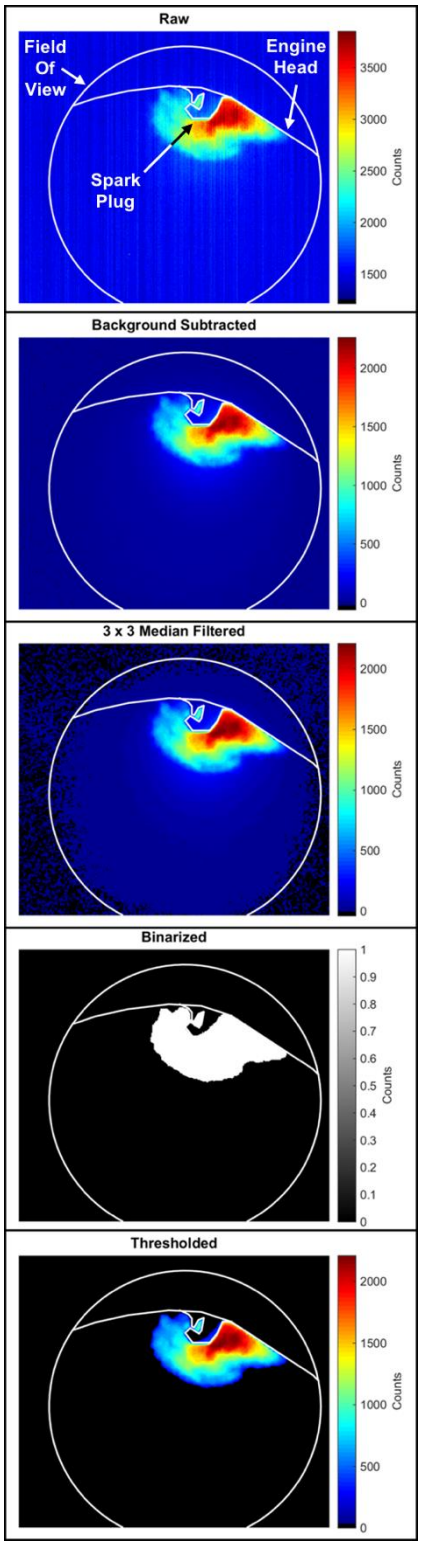

Figure 41. Images from Camera 1 illustrating the image-processing procedure [72].

The collection of all the images recorded at a given crank angle during each 100-cycle measurement is called a “subset” in this document. Each subset of thresholded images was

averaged, creating a mean image for each crank angle. The standard deviation of all the binarized images in select subsets was computed. The binarized image was chosen as the source of this calculation in order to avoid complications due to saturation. Using the binarized images also yielded standard-deviation images that were automatically normalized to a fixed scale: 0-0.5. A number of quantitative metrics were computed from the single and mean images, as described below.

The total integrated image signal, *S*, was defined as the sum of the counts in all pixels of a thresholded image. *S*, being essentially the total brightness of the flame in the 1.0- to 1.7- μm band, should be strongly dependent on the temperature and concentration of water in the flame. It is therefore expected that *S* should be correlated with the timing of major combustion landmarks.

The location of the flame centroid (center of mass) of each single image and each mean image was computed by weighting each pixel according to its brightness. The centroid is one way to quantify a flame's location. A "centroid cloud" was created for select subsets by marking the centroid of each image with a circle color-coded by the peak pressure, P_{max}, of that cycle. A centroid cloud illustrates the distribution of flame locations for each operating condition and shows where the flames producing the lowest and highest peak pressure were located. Centroid displacement was defined as the distance (in pixels) of the centroid of a given image from the centroid of the mean image. The effective radius (in pixels) of each flame was calculated as the radius of a circle having the same area as the flame. The normalized centroid displacement, δ, was calculated by dividing the centroid displacement of an image by the effective radius of the flame in that image. δ quantifies how far away a given cycle's flame is from the flame's average position for that operating condition.

$$I = \sum_{n=1}^{N} \sum_{m=1}^{M} c_{m,n} \times [(m - y_c)^2 + (n - x_c)^2]$$

The area moment of inertia (also called the second moment of area), *I*, was computed by the formula shown above for an *M*×*N*-pixel image, where $c_{m,n}$ is the pixel intensity at m^{th} row and n^{th} column and (x_c, y_c) is the centroid location. *I* is a measure of how much "mass" (number of pixels weighted by signal strength) a flame image has and how far that mass is from the centroid.

$$r_{gyr} = \sqrt{I/A}$$

Because very different shapes can have the same area and the same moment of inertia, the radius of gyration, r_{gyr}, was computed by the above formula from the area moment of inertia and the total projected area of the flame, A, in order to quantify the differences in flame shape. The radius of gyration is the radius of a point mass with the same I as the flame in the image; it is equal to the root-mean-square distance of each pixel (weighted by its brightness) from the centroid. For objects in general, r_{gyr} is a measure of how compact or extended the object is. A circle will have a small radius of gyration, while a rectangle of the same area with an aspect ratio of, e.g., 10:1 will have a larger r_{gyr}. A flame whose image has a larger radius of gyration would be expected to have a higher ratio of area to volume, in other words to be more stretched or wrinkled, and to burn more quickly. Different radii of gyration are illustrated in sample binarized flame images in Figure 42.

Figure 42. Binarized flame images illustrating different radii of gyration. For flames with the same size (top and middle), flames that are more spatially dispersed (middle) have higher r_{gyr} values. When both flames are similarly shaped (top and bottom), larger flames (bottom) have higher values of r_{gyr}. The units of area and r_{gyr} are pixels .

Each borescope contains a fish-eye lens at its tip, which provides the widest possible FoV but also distorts the images. As a result, calibrating the spatial dimensions, so that distances (e.g., δ) can be reported in mm rather than in pixels, is not as straightforward as applying a linear pixel-to-mm scaling. Instead, three-dimensional dewarping must be performed. That processing has not yet been undertaken, and all distances were calculated in pixels. It is expected that proper dewarping, once performed, will only strengthen the relationship between the image-derived and pressure-derived metrics described in the Results sections, so the conclusions drawn in that section remain valid even without calibration.

In order to investigate whether the IR images of the early flame kernel agreed with and predicted measurements based on the in-cylinder pressure, the Pearson correlation coefficient, *R*, was calculated for several combinations of an image-based metric (e.g. r_{gyr}, δ) computed at an early crank angle and a later metric (e.g., MFB_{10} or P_{max}) computed from in-cylinder pressure measurements in Cylinder 6 (and thus specific to that cylinder). It was not reasonable to compare the image-based metrics for different operating points at the same crank angle, since the flame development at any one crank angle would be very dissimilar between the points. Likewise, using a fixed crank-angle delay relative to the spark timing would not work for all conditions. For this document, the mean $MFB_{00.5}$ in Cylinder 6 for a given operating condition, labeled mean($MFB_{00.5}$) here, was chosen as the time at which the image-based measurements would be computed for the Pearson calculation. This timing provided a more consistent level of flame development and ensured sufficient delay between the image- and pressure-based measurements for the results to be of interest. The symbol $R(x, y)$ is used in this document to represent the correlation between image metric *x*, measured at mean($MFB_{00.5}$), and pressure metric *y*.
In order to compare images at multiple crank angles for different operating conditions, it was necessary to determine "normalized crank angles" at which flame development was comparable across conditions. Six crank angles evenly spaced between spark timing and mean($MFB_{00.5}$) were computed for each condition, and these crank angles were labeled $\theta_{x/5}$ where *x* indicated the fraction of angle between spark and mean($MFB_{00.5}$), as shown in Figure 43.

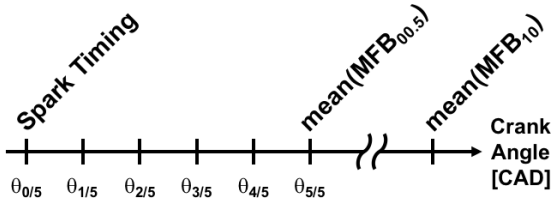

Figure 43. The normalized crank angles, $\theta_{x/5}$, at which images from different conditions were compared. In courtesy of Dr. Michael C. Gross [72].

3.9 Comparative UV-IR Imaging of Ignition Experiments

Near-IR imaging (1000-1700 nm) enabled us to track the water emission to identify the burned-gas region inside the low-light engine cylinder. With this technique, the early flame kernels in an engine environment were identified and studied. However, by choosing IR imaging

to study flames more rigorously, the ability to detect spark plasmas and corona streamers are compromised, because the majority of the signal from these plasmas are in the UV and visible bands. The plasma-to-kernel transition is critical to understand the entire ignition process. OH* radical is a tracer of the flame front, so it is of particular interest.

In order to address this issue, a benchtop experimental setup was built to measure the chemiluminescence from hydroxyl radicals (OH*) in the plasma and the flame kernel (Figure 44). OH* is a tracer of the flame front, and it emits strongly across 280-340 nm, with the strongest emissions near 310 nm [76]. A LaVision HS-IRO image intensifier and a 260-380 nm band-pass filter were used to enable high-speed VisionResearch Phantom v7.3 CMOS visible band-camera to detect this OH* emission at 12 kHz rate and 29.24 μs exposure time.
Since all the data collected in the engine experiments were from the IR band, it was important to be able to interpret the correspondence between that IR signal to its UV counterpart. In order to achieve that, a Xenics Cheetah-640-CL camera with 1000 nm long-pass filter, the same camera and filter used in the engine experiments to detect strong H_2O signals within 1.0-1.7 m band (Section 3.4), were set to image the ignition event in the synchronously with the Phantom camera. Even though synchronized, Cheetah camera could not run at 12 kHz rate as the Phantom camera, so it was set to run at 1 kHz rate with the help of a skip-fire box as the Cheetah camera captured images at every twelfth Phantom camera image. Exposure time of the Cheetah camera was set to be 50 μs.

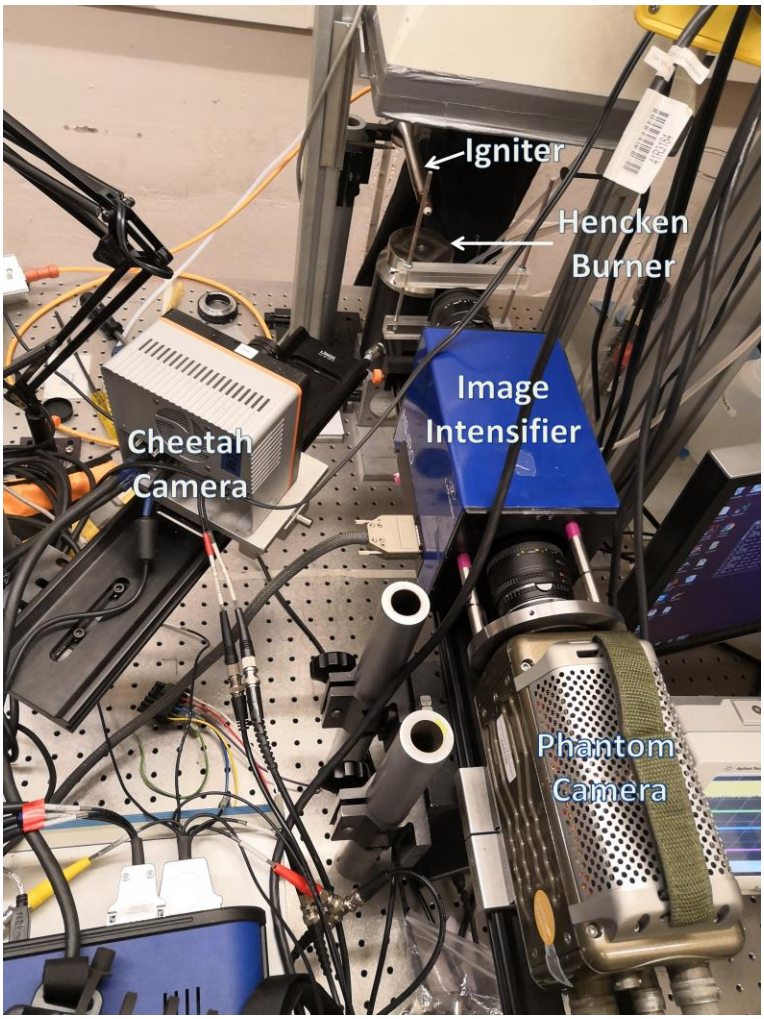

Figure 44. Experimental setup for the atmospheric UV-IR imaging experiments.

These experiments were conducted under atmospheric conditions. A Hencken burner is used in order to provide adequate control over mixture conditions. As it can be seen in Figure 45, Hencken burner has a fine honeycomb structure through which methane and air were delivered as a laminar premixed mixture.

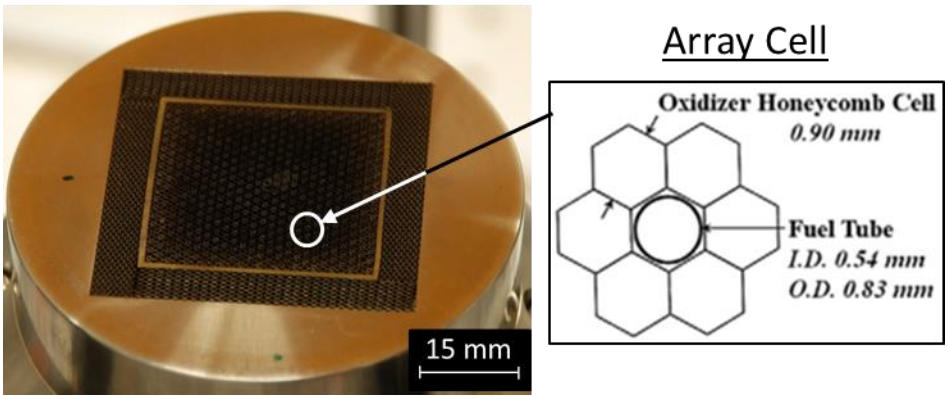

Figure 45. Hencken burner and the schematic of its array cell structure [77] are shown. In courtesy of Ivan Tibavinsky.

A BorgWarner EcoFlash corona igniter was placed above the Hencken burner to ignite the methane-air mixture with corona streamers. Views of this igniter from both cameras are shown in Figure 46. The ignition voltage and duration were set to be 50 V and 350 μs (single burst) respectively. The voltage output from the controller box of this igniter was measured as in Figure 47, which shows the actual discharge duration to be ~380 μs. The actual voltage that creates the corona discharge is also significantly higher than this measured control-box output voltage, because this voltage goes into the igniter in which it gets amplified.

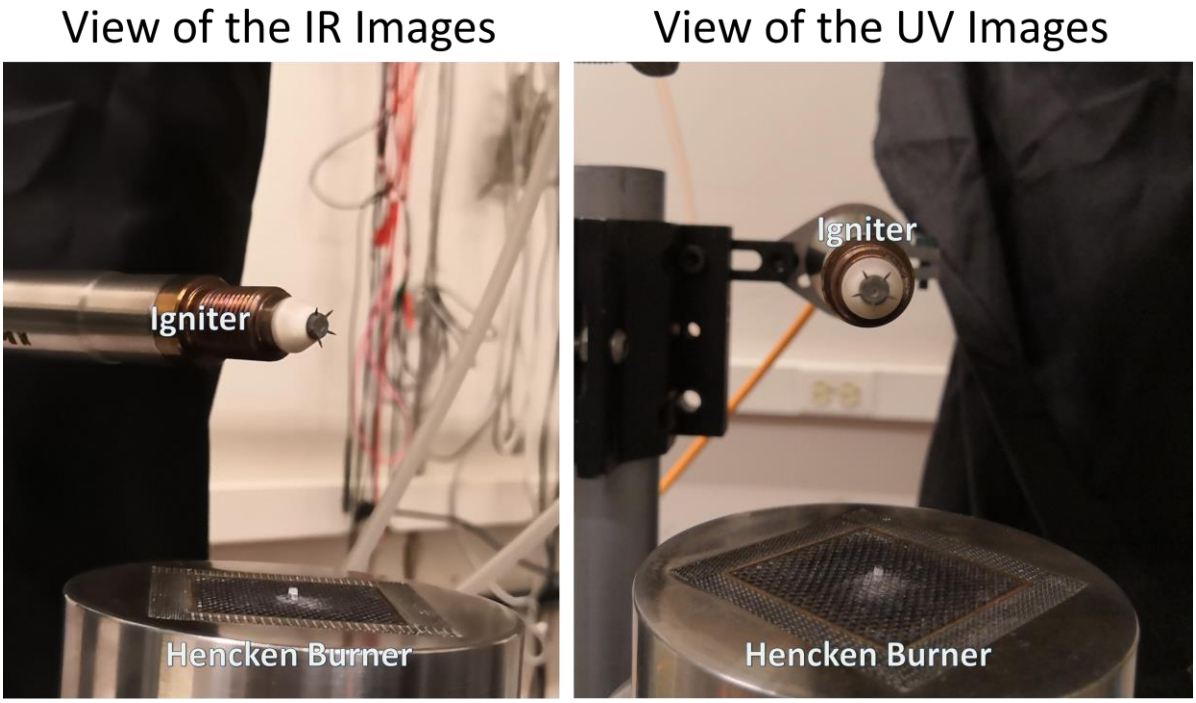

Figure 46. Visible views of the igniter from Cheetah (left) and Phantom (right) camera locations.

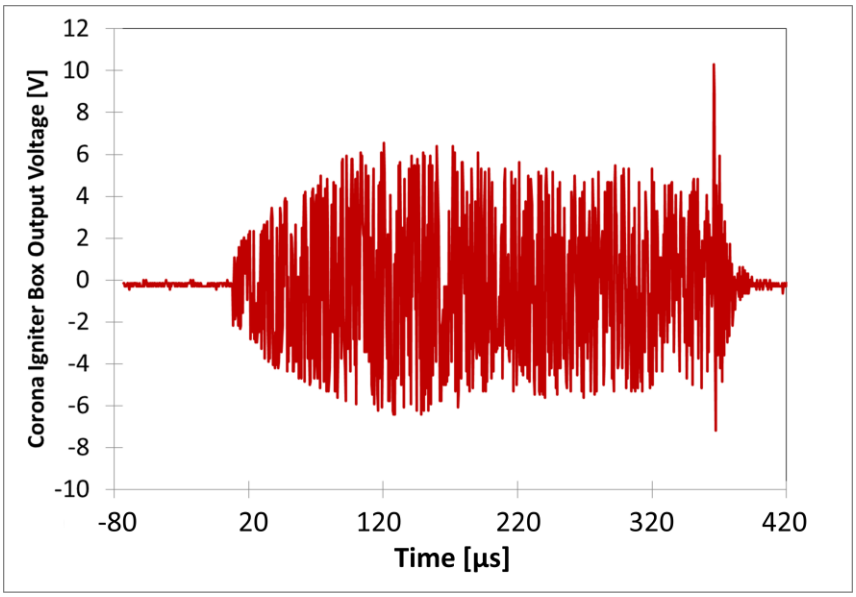

Figure 47. Measured voltage output from the corona ignition system's controller box.

CHAPTER 4 RESULTS AND DISCUSSION

4.1 Pressure-Derived Results and Emissions

Quantitative results are tabulated in Table 7 and Table 8. Ignition delay is defined as the mean (for all 100 cycles) difference (in CAD) between spark timing and MFB_{10}. Combustion duration is defined as the mean difference between the MFB_{10} and MFB_{90}. BSFC is the brake specific fuel consumption. BS HC is the brake specific mass of unburned hydrocarbons measured in the exhaust before the catalytic converter. Likewise, BS NO_x is the brake specific mass of oxides of nitrogen measured in the exhaust before the catalytic converter.

Table 7 shows the effects of the CEI dwell and glow times on these parameters. Each column is color-coded from red for the lowest value to blue for the highest. The two durations had similar impacts. The mean ignition delay and BSFC were essentially unchanged across the conditions tested. CoV(IMEP), BS HC and brake specific carbon monoxide emission (BS CO) favored longer durations, while combustion duration and BS NO_x favored shorter durations. Table 8 shows the comparison of the igniters over a range of operating conditions and is color-coded in the same manner as Table 7. For all of the igniters, lean mixtures yielded reduced BSFC, BS NO_x, and BS CO as well as increased ignition delay, combustion duration, and BS HC. Similarly, EGR-diluted mixtures resulted in lower BS NO_x and BSFC as well as higher ignition delay, combustion duration, and BS HC. Unlike lean operation, EGR caused a mild increase in CO emission. When excess air and EGR were introduced together, CoV(IMEP) levels increased significantly. Comparing the igniters reveals that CEI reduced BS NO_x compared to 65-mJ and 140-mJ igniters, with the exception that the 65-mJ igniter performed the best under EGR-diluted conditions. CEI also reduced BS CO compared to the 65-mJ and 140-mJ igniters, with the exception that the 140-mJ system performed better at the $\lambda = 1.6$ and 10% EGR point. All three igniters had very similar ignition delay and combustion duration characteristics. The 140-mJ system outperformed 65 mJ system and CEI in terms of CoV(IMEP) under all lean-and-diluted conditions, and also in terms of BS HC in all common conditions except the stoichiometric undiluted case, in which CEI performed marginally better.

To more clearly illustrate trends in the data, selected results from Table 8 corresponding to two operating conditions, $\lambda = 1.0$ with minimal EGR and $\lambda = 1.6$ with 10% EGR, are plotted in Figure 48 and Figure 49. These conditions were selected because they were the most extreme conditions (the easiest and most difficult to ignite). As discussed above, the minimum EGR rate (the rate measured with the EGR valve closed) was nonzero; for all three igniters, it was 3-4% for the stoichiometric points and 2% for the lean points. Figure 48 is a plot of CoV(IMEP) for each igniter for each of these two operating conditions. All three igniters produced comparable CCV for the stoichiometric, minimally diluted condition. All the igniters yielded higher CCV in the lean, dilute condition, but the 140-mJ IDI system performed significantly better than the others. Figure 49 shows the brake specific quantities of three types of emissions (hydrocarbons, oxides of nitrogen, and carbon monoxide). The two operating points are plotted on separate axes to enhance clarity. For the stoichiometric, minimally diluted condition CEI yielded the lowest quantity of all three pollutants. For the lean, dilute condition, the 140-mJ system produced the lowest BS HC and BS CO, but the 65-mJ system produced the lowest BS NO_x.

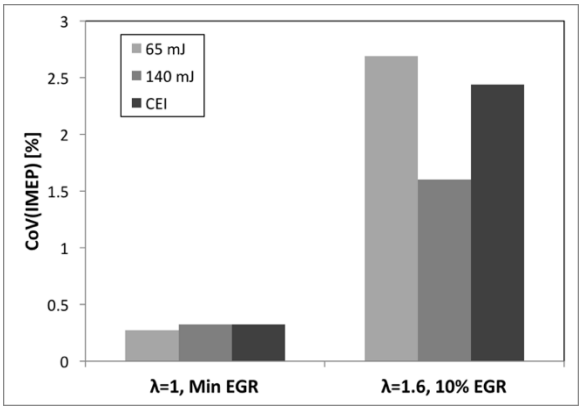

Figure 48. Cycle-to-cycle variation for each igniter at two operating points [71].

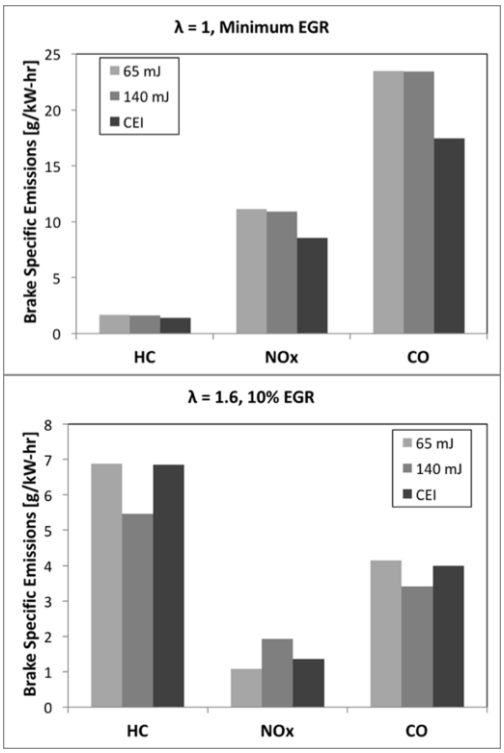

Figure 49. Brake-specific emissions for each igniter at two operating points. Top: stoichiometric air/fuel mixture with minimum EGR (3-4%). Bottom: lean mixture with 10% EGR [71].

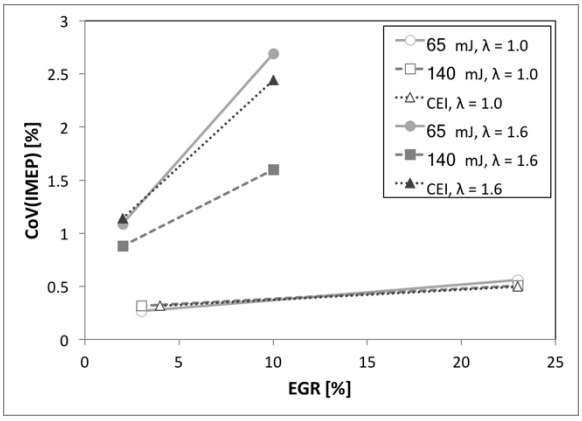

Figure 50. CoV(IMEP) plotted against EGR rate for each igniter [71].

The results in this chapter exhibit that variations in mixture compositions and igniter selection has a direct impact on the emissions and CCV of in-cylinder pressures. Understanding the cause of this CCV requires direct imaging of the flame. Therefore, rest of the dissertation focuses on the image-based results to explain flame kernel behavior.

4.2 Image-Derived Results

4.2.1 Effect of the Mixture Composition on Ignition and Combustion

Figure 51 presents the mean images (computed over 100 cycles) at five normalized crank angles ($\theta_{1/5}$ through $\theta_{5/5}$) for all four operating conditions with 140-mJ igniter. The conditions are shown in the order of increasing IMEP variability—see Table 8—from left to right. As expected, mean images of all four cases at $\theta_{5/5}$ look similar in terms of flame size and intensity distribution, because they all correspond to the same combustion phase ($MFB_{00.5}$). However, the discrepancy in flame-kernel size between operating conditions becomes increasingly apparent for increasingly early normalized crank angles. Especially at $\theta_{1/5}$, the kernel size is clearly largest for the stoichiometric and minimally diluted case, whereas it is the smallest for the lean and diluted case. This result indicates that the initial laminar flame-kernel growth regime is extended, and thus flame wrinkling is delayed, with excess air and dilution. Another observation from Figure 51 is that the flame location and orientation differ substantially from case to case across any given $\theta_{x/5}$. The primary reason is the discrepancy in spark timing (Table 8). Since the optimized spark timing is different for each case, the flow (tumble and swirl) and pressure conditions during spark and early kernel growth are also different, which result in differences in flame-growth patterns.

The standard deviation of the binarized images computed at the same normalized crank angles are presented in Figure 52. These images visualize the variation in location of the flame boundaries over 100 cycles. For all four cases, the curved red band indicating flame-boundary variability widens as the combustion phase progresses from $\theta_{1/5}$ to $\theta_{5/5}$. Comparison of different operating points across the same $\theta_{x/5}$ reveals that EGR dilution and lean operation, either individually or combined, widen the band of flame-boundary variability. This observed image variability is consistent with the CoV(IMEP) results tabulated in Table 8, as the cases with higher CoV(IMEP) exhibit higher flame boundary variability, and vice versa.

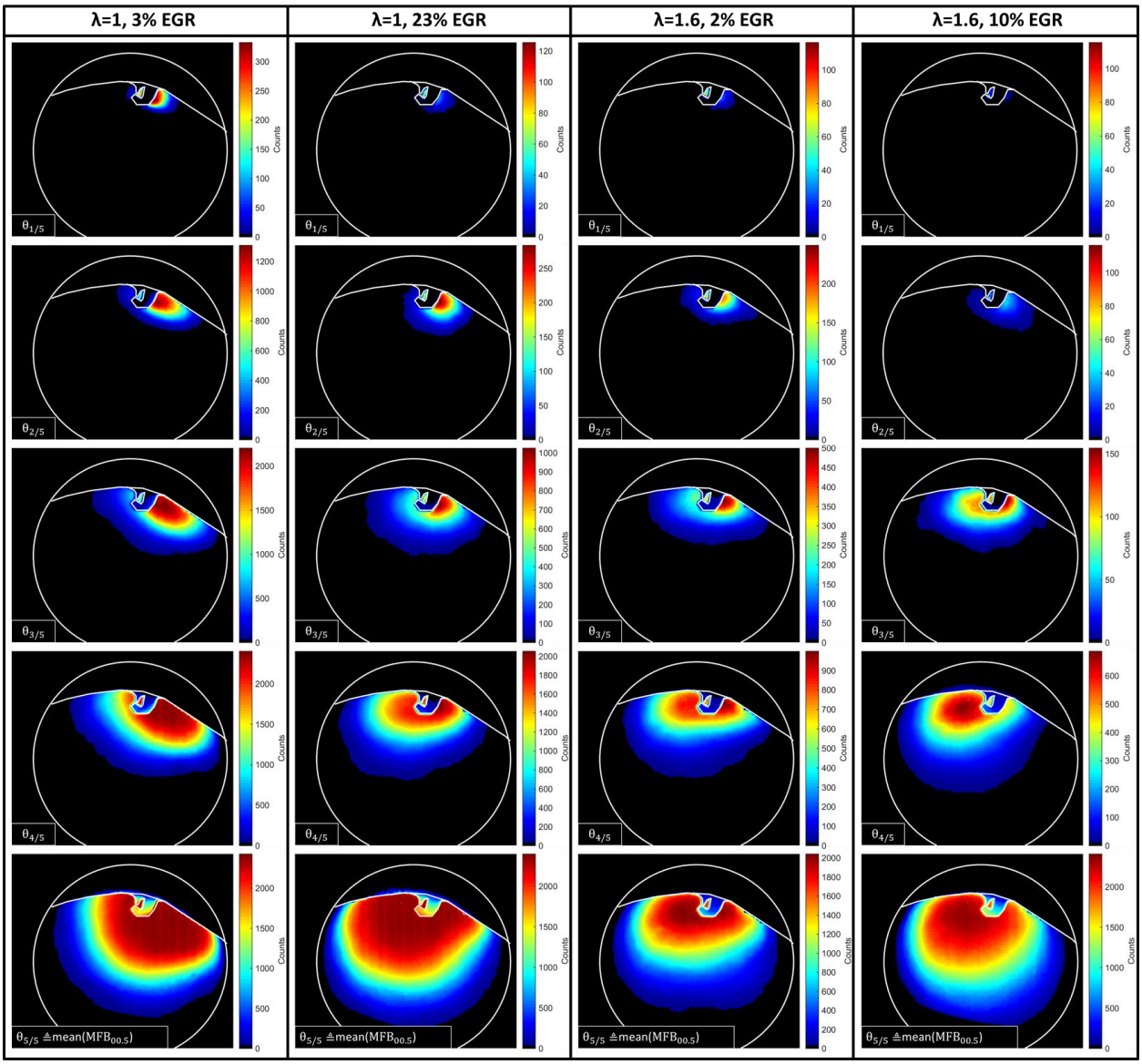

Figure 51. Mean images of flame locations from Camera 1 for five crank angles for four operating conditions with 140-mJ igniter, all at an engine speed of 1000 rev/min and an IMEP of 6.8 bar [72].

Centroid clouds computed at the same crank angles for all four conditions are shown in Figure 53. Comparing the first column to the second and the third column to the fourth shows that, until about $\theta_{3/5}$, the cases with the minimum achievable EGR have smaller clouds than those with 10-23% EGR. Similarly, comparing the first column to the third shows that, until $\theta_{3/5}$, the stoichiometric case produces a smaller cloud than the lean case. This result indicates that both higher EGR rates and leaner air/fuel ratios are associated with less consistent flame location, which agrees with the well documented observation that increasing the EGR rate or λ increases

CCV. It has been established [78, 79] that the combustion physics occurring between spark timing and ~MFB_{01} is the principal source of CCV. Schiffmann *et al*. [17] studied the relationship between the early kernel growth and CCV using a number of optical diagnostics applied to an optically accessible engine. This work attempts to investigate the same period in a modified production engine via the more limited optical access provided by borescopes and using IR imaging to maximize signal and locate the flame. One approach to reliably ignite leaner and more EGR-dilute mixtures is to employ an advanced ignition system, which is the goal of the project of which this work is part. The results of the impact of igniter choice on the combustion of lean/dilute natural-gas mixtures resulting from the project are described in Chapter 4.2.2.

Examining Figure 53 again reveals another pattern, which appears by mean($MFB_{00.5}$), the bottom row of the figure, for each operating point. For each condition, centroids positioned lower in the plot (farther from the head) very early in the cycle lead to higher peak pressures. This result makes intuitive sense; flames centered farther from the head have more room to grow without being quenched, leading to better combustion. This relationship, though well known, is not provided by the pressure-derived metrics.

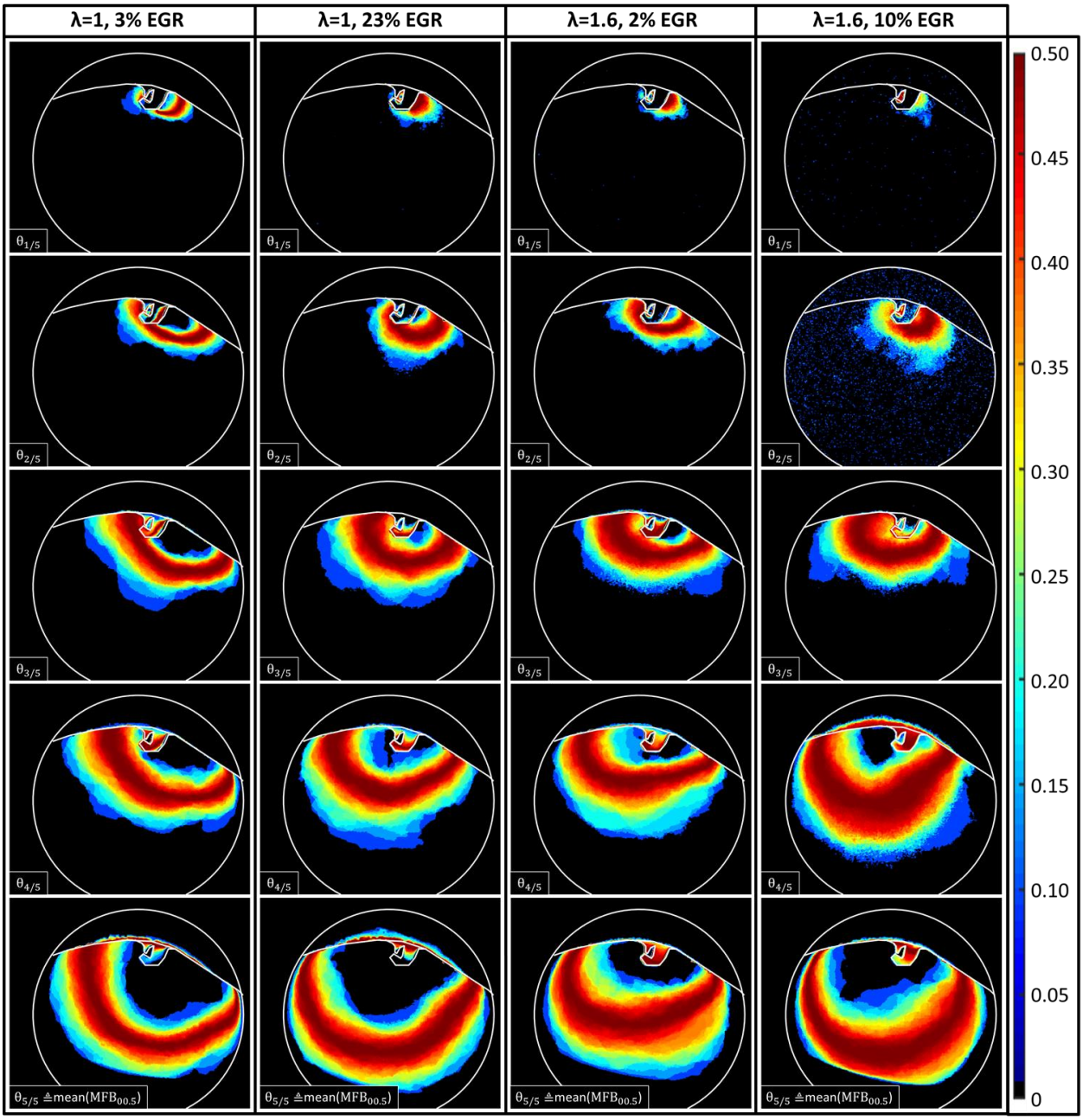

Figure 52. Standard deviation of the binarized images from Camera 1 for five crank angles for four operating conditions with 140-mJ igniter, all at an engine speed of 1000 rev/min and an IMEP of 6.8 bar [72].

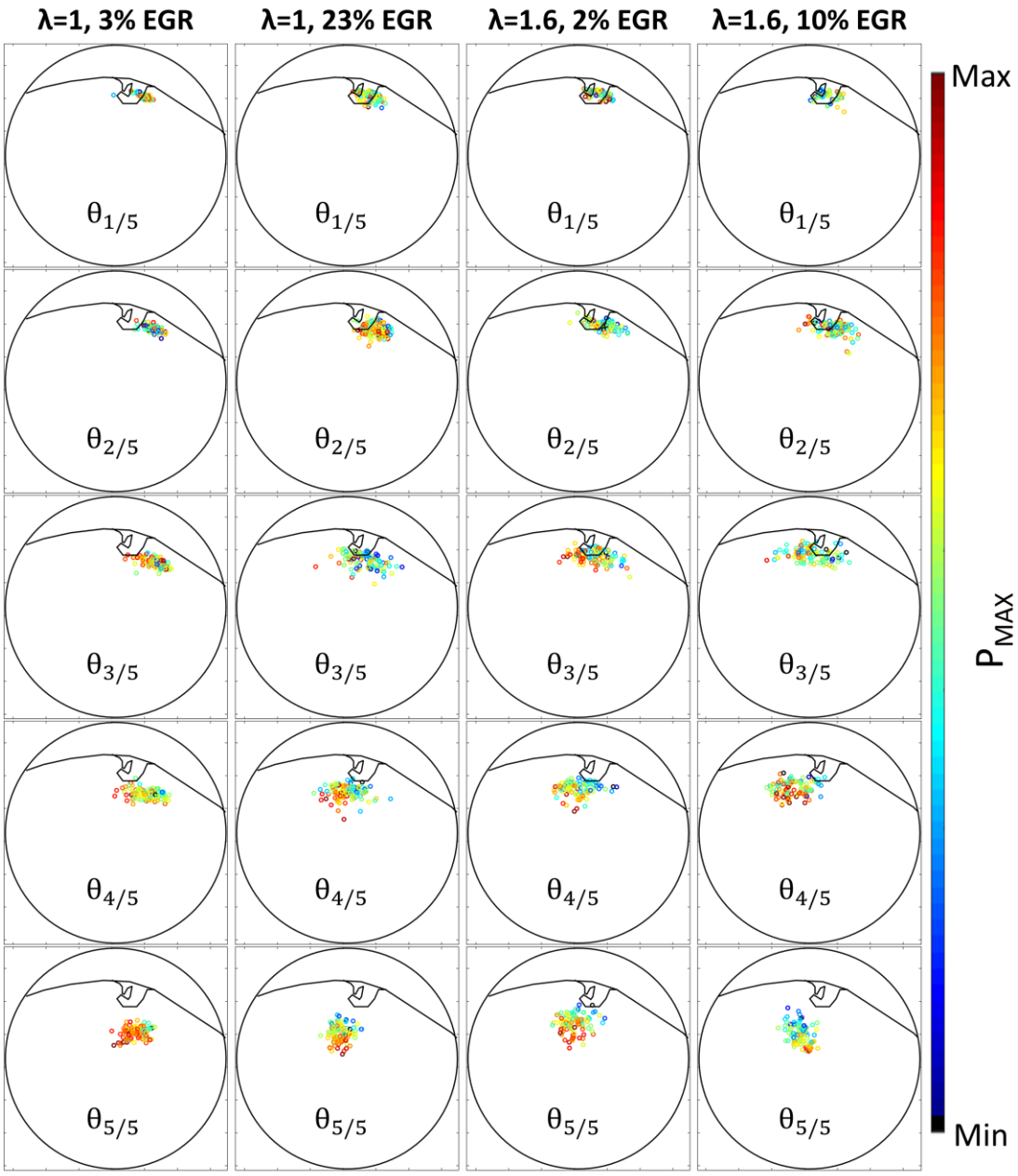

Figure 53. Centroid clouds for five crank angles for four operating conditions with 140-mJ igniter, all at an engine speed of 1000 rev/min and an IMEP of 6.8 bar [72].

Figure 54 is a set of correlation plots, each showing the relationship between four MFB_x values (MFB_{05}, MFB_{10}, MFB_{50}, and MFB_{90}) and the radius of gyration for 100 cycles for all four operating points. Recall that r_{gyr} is a measure of the degree to which the flame is stretched or elongated. The plots and the Pearson correlation coefficients shown in this figure and tabulated in Figure 54 indicate that the very early-cycle measurement of the radius of gyration is a good predictor for the timing of major combustion landmarks up to MFB_{50}, but that this predictive

capability is weaker for MFB_{90} and therefore for combustion duration (defined here to be MFB_{90} - MFB_{10}). Note that the correlation coefficients are negative; meaning a flame whose two-dimensional projection exhibits a smaller r_{gyr} is correlated with later values for $MFB_{05,}$ $MFB_{10,}$ MFB_{50}, and MFB_{90}. This result is consistent with expectations; a flame whose image has a smaller radius of gyration would be expected to be less stretched and wrinkled and therefore to burn more slowly.

Similarly, results from engine operation listed in the rightmost four columns of Table 8, though not plotted, show that the total integrated signal predicts the early flame development through MFB_{50} well (though not as well as r_{gyr} does), but likewise does not correlate as strongly with MFB_{90} and combustion duration. This result is consistent with the interpretation of the integrated signal as closely related to the reaction rate.

Returning to the discussion of radius of gyration, Figure 55 is a correlation plot showing the relationship between the peak in-cylinder pressure and the r_{gyr} measured at mean($MFB_{00.5}$) and for all 100 cycles at the four operating points. The *R* values presented in the legend show that r_{gyr} measured very early in the cycle can predict the eventual P_{max}, which typically occurs somewhere near MFB_{50}, for all four conditions. In other words, more extended flames burn more quickly and reach higher pressures, which is consistent with expectations.

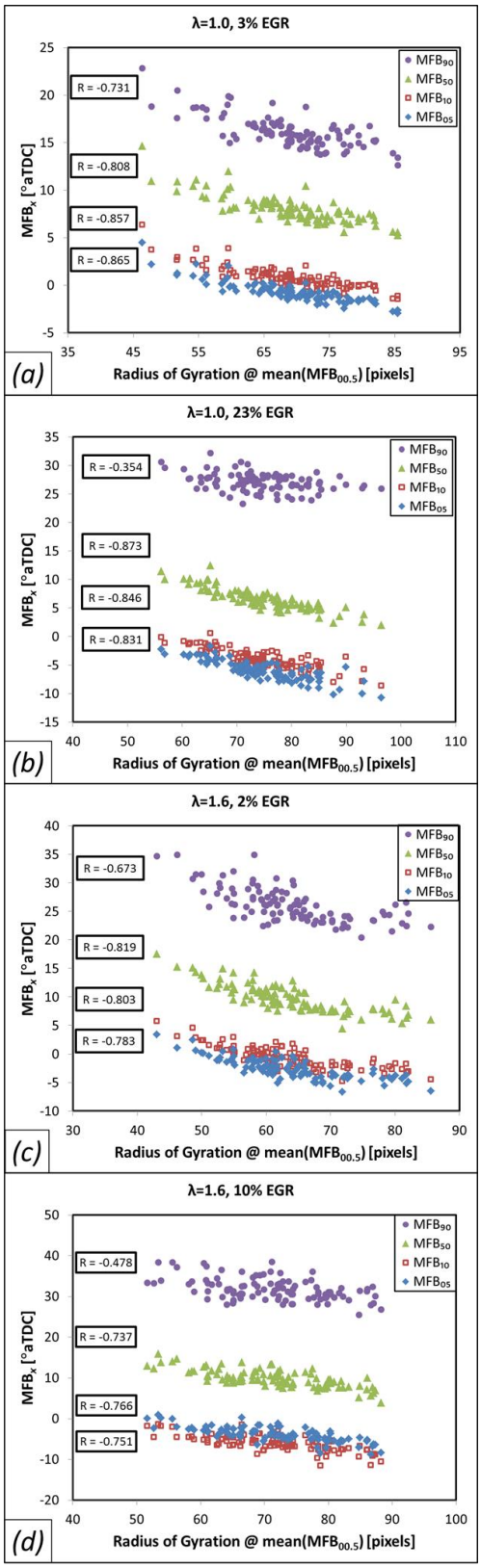

Figure 54. MFB_{05}, MFB_{10}, MFB_{50}, and MFB_{90} correlated with r_{gyr} measured at mean($MFB_{00.5}$) for 100 cycles of operation at all four operating conditions [72].

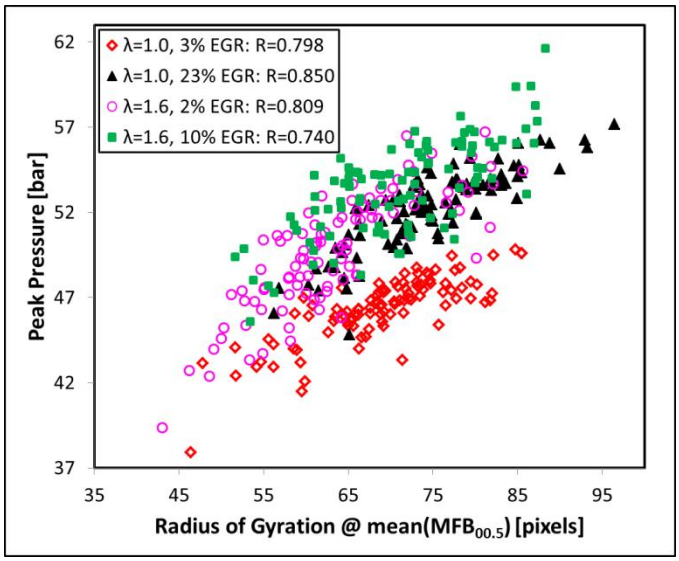

Figure 55. Peak pressure correlated with radius of gyration measured at mean($MFB_{00.5}$) for 100 cycles of operation at four operating conditions [72].

Figure 56 is a set of correlation plots showing the relationship between normalized centroid displacement and MFB_{10} for all 100 cycles of the same four operating conditions. Recall that δ is a measure of how far the position of the flame at one early crank angle in any given cycle differs from the average centroid position over 100 cycles. The dashed line segments are added to aid the eye. For δ values below ~0.2-0.4, where the density of data points is relatively high, a pattern is evident in the point distribution; the cycles with smaller displacements are more consistent in the time at which they reach 10% fuel burn. For δ values greater than ~0.2-0.4, the density of points is too low for any pattern to be apparent, so no conclusion can be drawn from these few highly displaced cycles. This result indicates that flames that are located farther from the average position result in more inconsistent combustion timing.

Results shown in this chapter illustrate how mixture composition impacts the shape of the flame. CCV in flames are typically caused by in homogeneities and inconsistencies in mixture composition and flow conditions. Under lean and EGR-diluted mixtures, the laminar flame speeds are lower, so the discrepancies in thermodynamic and flow conditions near the flame front causes a more pronounced variation in in flame shape at further combustion phases. The early flame shape is informative about the conditions surrounding the flame such that the flame is stretched.

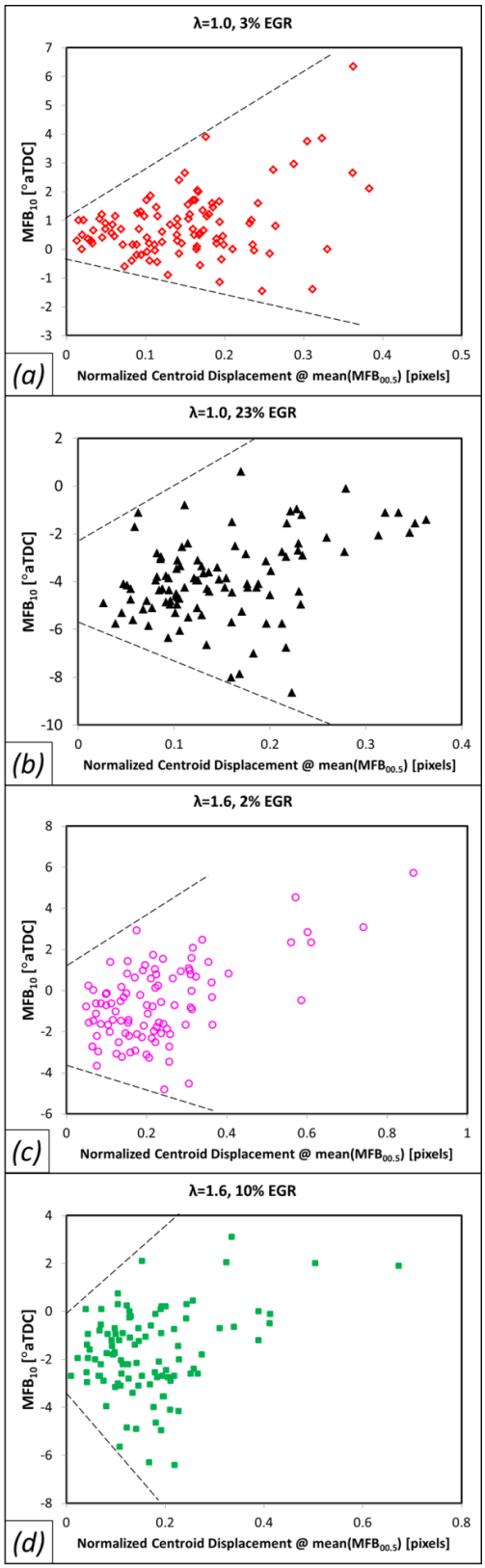

Figure 56. MFB_{10} correlated with δ measured at mean($MFB_{00.5}$) for 100 cycles at all four operating conditions [72].

4.2.2 Effect of the Igniter Selection on Ignition and Combustion

4.2.2.1 Comparison of Conventional, Conventional High-Energy, and Controlled Electronic Ignition Systems

The first part of this section will focus on image-based data for the operating point with λ = 1.6 and 10% EGR. This condition was chosen for highlighting in this section because it was the most difficult-to-ignite mixture tested. The integration times for the images reported were 10 μs for the 65-mJ system, 20 μs for the 140-mJ system, and 10 μs for CEI.

Figure 57 illustrates the variation between cycles of the three Bosch ignition systems studied for this condition. The images in each column were recorded at normalized crank angle $\theta_{3/5}$ during different cycles with one ignition system. The cycles used in this figure were chosen subjectively to exemplify the variation between cycles, and the images do not necessarily represent an objective comparison between systems. Additionally, as Figure 57 illustrates, IR borescopic images of early flame kernels are consistently visible and clear, even before $MFB_{00.5}$ (which equals $\theta_{5/5}$). Thus, high-speed IR imaging can provide valuable information about kernel development at points where data from pressure transducers are unreliable.

Figure 58 illustrates the evolution of an average cycle with each ignition system. The images were recorded at $\theta_{1/5}$, $\theta_{2/5}$, $\theta_{3/5}$, $\theta_{4/5}$, and $\theta_{5/5} \triangleq \text{mean}(MFB_{00.5})$. Although these images were recorded with unequal integration times and are presented in false-color scales intended to optimize the view of each individual image (rather than the same color scale for all images), they were all thresholded individually, so the shape the flames can be compared. Both of the high-energy systems produce larger flame kernels, compared to the standard-energy system, at $\theta_{4/5}$ and $\theta_{5/5}$, as expected. Interestingly, the 140-mJ system produced smaller kernels at $\theta_{1/5}$ and $\theta_{2/5,}$ which is counterintuitive. The two high-energy systems produce very similar flame sizes at mean($MFB_{00.5}$), but the paths the kernels take to arrive at that point are significantly different. The mean($MFB_{00.5}$) for this mixture was -6.11, -6.28, and -13.64 °aTDC for the 65-mJ system, the 140-mJ system, and CEI, respectively, meaning that the CEI system consumes the first 0.5% of the fuel much earlier in the cycle than the other two systems. This timing manifests in Figure 58 as the flame kernels of the 65- and 140-mJ systems being partially obscured by the piston at $MFB_{00.5}$, as visible at the bottom of the flame in the bottom row of images in the left and middle columns.

Figure 59 shows the standard deviation of the binarized images over 100 cycles to illustrate the cycle-to-cycle variability of the flame boundary location throughout the cycle for the same lean, dilute mixture. The rows were recorded at the same five crank angles as in Figure 58. Early flame growth with 65 mJ igniter results in slightly wider bands of high variability (indicated by red, orange, or yellow false color) compared to the 140 mJ igniter and the CEI system. This result is consistent with the higher measured CoV(IMEP) for that system, as tabulated in Table 8.

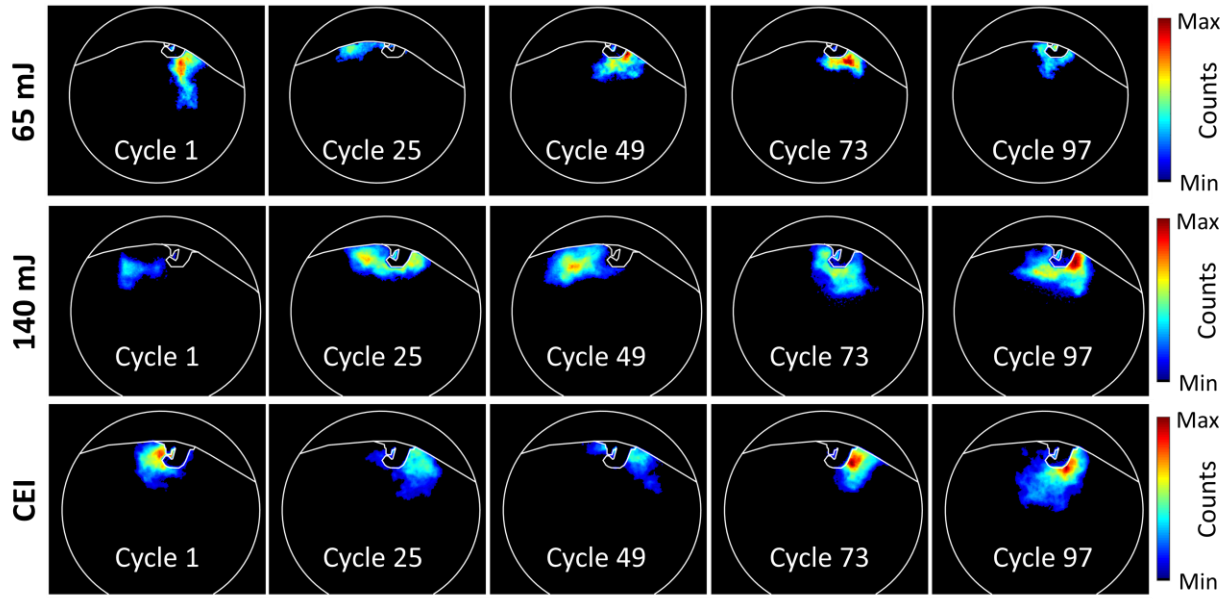

Figure 57. Images recorded at the same normalized crank angle, $\theta_{3/5}$, during different combustion cycles for all of the ignition systems studied [71].

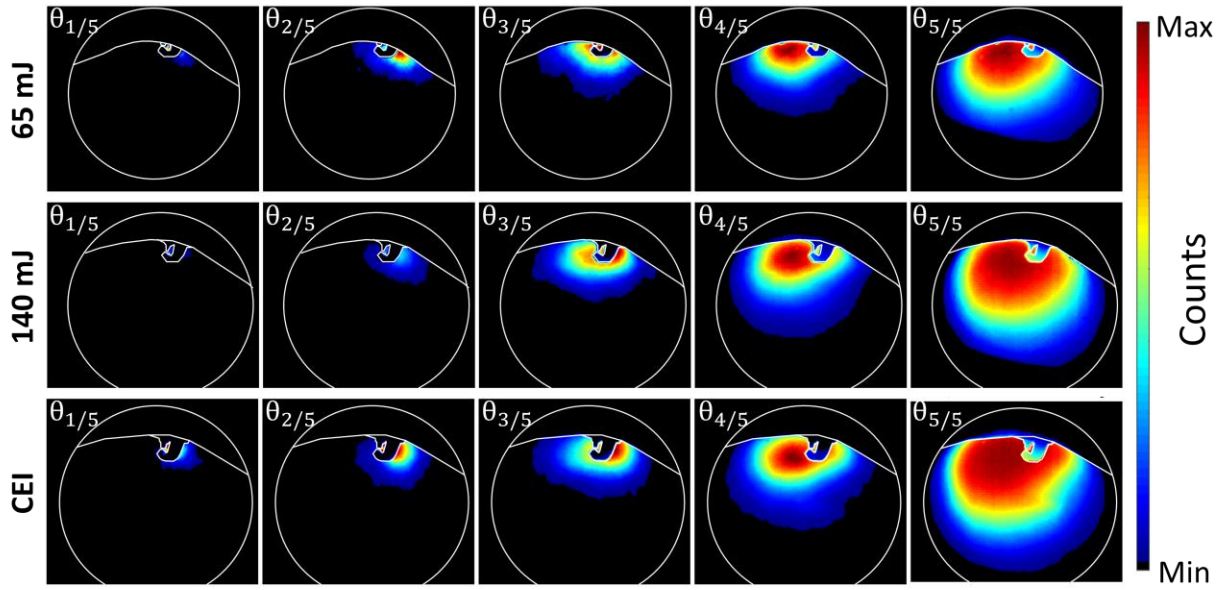

Figure 58. Images showing the flame development during an average cycle for each ignition system. Each frame was computed by taking the mean of each pixel across all images recorded at given crank angle for all 100 cycles of the measurement [71].

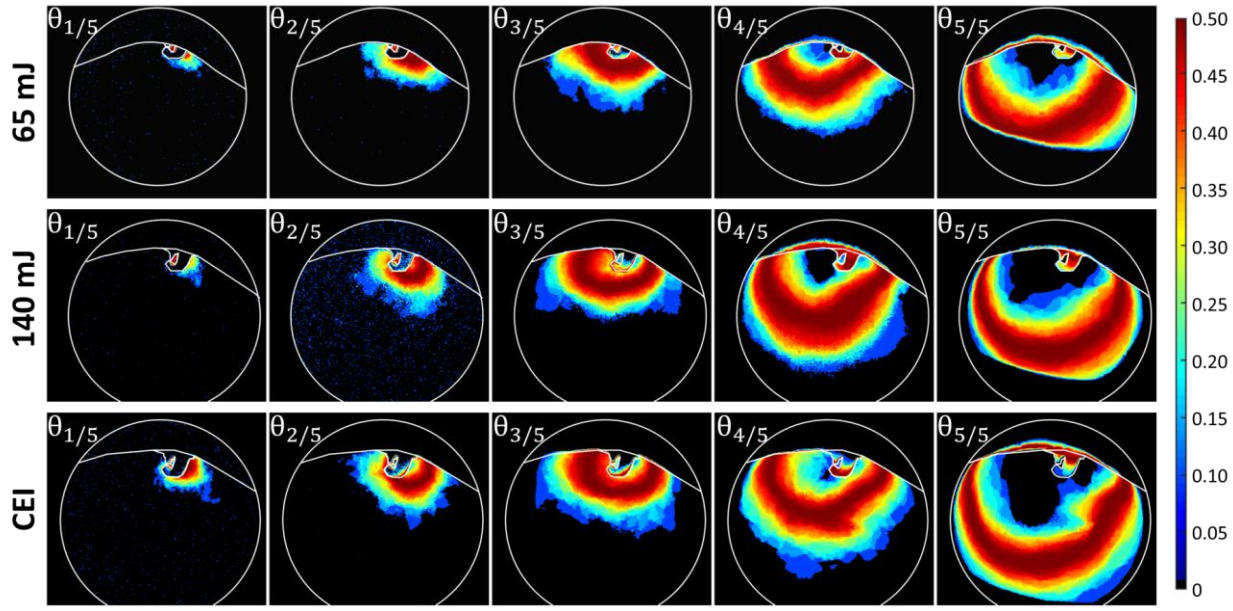

Figure 59. The standard deviation of the binarized images of flame development with each ignition system. Each frame was computed by taking the standard deviation of each pixel across all the binarized images recorded at a given crank angle for all 100 cycles of the measurement [71].

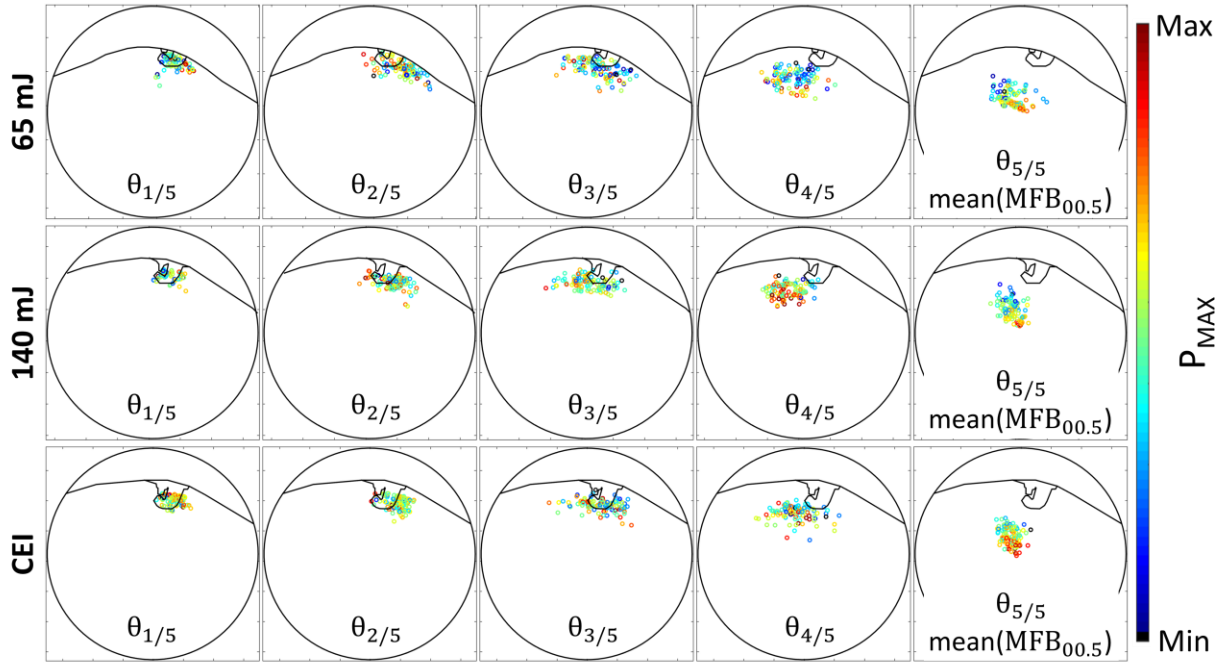

Figure 60. Centroid clouds for each ignition system for various crank angles. Each circle marks the location of the centroid of the flame in one cycle at that crank angle and is color-coded according to the P_{max} of that cycle [71].

Figure 60 shows centroid clouds at $\theta_{1/5}$, $\theta_{2/5}$, $\theta_{3/5}$, $\theta_{4/5}$, and $\theta_{5/5}$ for each ignition system. The 65-mJ system's clouds are larger than those of the high-energy systems for all the crank angles shown. The 140-mJ and CEI systems' clouds are approximately the same size through the first three frames, but in the last two frames, the CEI cloud is larger. This result is consistent with the CoV(IMEP) values plotted on the right half of Figure 48; both high-energy systems produce lower cycle-to-cycle variability than the standard-energy system, but the 140-mJ system produces the lowest CCV. Significantly, by the final image, all three systems' images display clear relationships between the centroid locations and the peak pressures associated with them; the centroids with lower peak pressure are located to the upper left (closer to the head), while those associated with higher peak pressure are located to the lower right (farther from the head). This result agrees with intuition; the flames that are centered farther from the head surface are expected have more room to grow before quenching at the walls and to eventually yield higher peak pressures.

4.2.2.2 Comparison of Conventional and Corona Ignition Systems

Corona ignition system is investigated under a comparative study with 65-mJ igniter. The results from the in-cylinder pressure transducers are tabulated in Table 9. For each mixture, the

ignition delay was much shorter for the corona system, but the combustion duration was more similar between the two systems. In short, the corona system greatly accelerates the flame's growth during the first 10% of fuel burn but doesn't dramatically shorten the time required to consume the next 80% of the fuel. For both of the igniters, the lean/dilute mixtures yielded increased ignition delay and combustion duration. The increase in ignition delay—a factor of 2.85 for IDI and 2.37 for corona—was significantly lower for the corona system. By contrast, the increase in combustion duration—factor of 2.24 for IDI and 2.04 for corona—was very similar for both of the systems. This result also indicates that the corona ignition is more beneficial to the early phases of combustion. The CoV(IMEP) increased by a factor of 10 for IDI but only 4.8 for corona, indicating that the corona system ignites the mixture more repeatably.

Figure 61 shows the early development of flames ignited by the IDI system, as seen by Camera 1. Each successive row was recorded 1.0 CAD after the previous one. The timing of each image is denoted in degrees of crank angle after spark timing (°aS). On the left are binarized single frames recorded during the 50^{th} cycle of consecutive offset. These images are not from the same cycle, so they do not form a sequence of consecutive images, but they do illustrate the behavior of the early flames. Single-frame images are shown because they capture the fine structure that is blurred in the mean images. Binarized images are used because they better convey the extent of the flame, particular during the first 1-2 °aS, when the flame is dim and the signal-to-noise ratio is port. On the right are binarized mean images produced by averaging all cycles at each crank angle. IDI system generates a single ~1-mm spark plasma, around which a small, circular flame kernel forms. This flame kernel goes through a slow laminar growth phase until it reaches the size at which it begins to wrinkle. Once the flame wrinkles, rate of growth increases dramatically due to the increase in flame surface area.

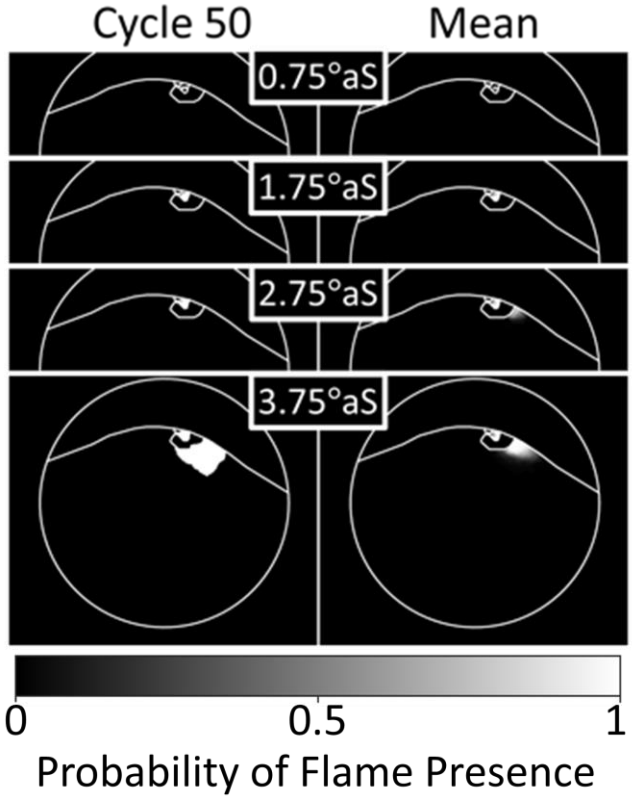

Figure 61. The early development of flames conventionally ignited flames. Left: Binarized single frames from the 50th cycle of consecutive offsets. Right: Mean binarized images at each crank angle [73].

Figure 62 is the corona equivalent of Figure 61, as seen by Camera 1. Because the corona-ignited kernels grew so quickly, the offset between successive 100-cycle measurements was halved for measurements with this system; each row in the figure was recorded 0.5 CAD after the one above. The corona system ignites five kernels, one from each electrode tip. Only four kernels are visible in these images; the fifth kernel, located behind the igniter in images recorded with Camera 1, is visible in images recorded with Camera 2; those images are not presented here. The binarized single frames illustrates how the flame propagates along the streamers produced by the electrode tips and that the flame kernel exhibits significant wrinkling almost immediately after ignition. This wrinkling speeds the flame growth early in the cycle. The exact streamer paths are random, so they are different in each of the cycles shown, but the streamer-like shape of the flame kernels is apparent by 0.85 °aS. These irregularly shaped ~1-cm-long streamers initiate flame wrinkling very quickly. Thus, the flame kernels' slow, laminar growth regime is eliminated. Having five initial flame kernels instead of one further increases the

flame surface area in the early stages of combustion. As can be seen in Figure 62, the five flame kernels have merged by 3.35 °aS. The behavior is less pronounced in the mean images, such as those shown on the right, due to the stochastic nature of the streamer locations. However, the consistent creation of separate flame kernels is still visible in the mean images.

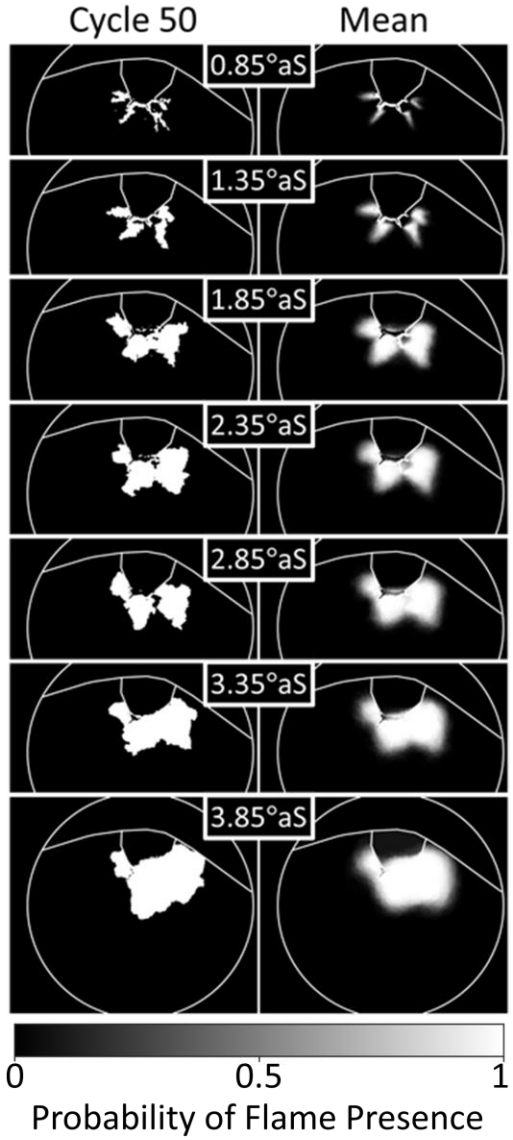

Figure 62. The early development of flames corona-ignited flames. Left: Binarized single frames from the 50th cycle of consecutive offsets. Right: Mean binarized images at each crank angle [73].

Figure 63 is a plot of flame area (as measured with Camera 1) for each mixture and each ignition system. Note that this plot only covers the early flame growth (from spark timing until the corresponding ensemble-averaged $MFB_{00.5}$ for each case); beyond TDC, the flame fills and saturates the camera's FoV. The plot shows that the corona-ignited flame grows much more

rapidly than the conventionally ignited one. The growth-rate patterns are also significantly different between the corona-ignited flames and the conventionally-ignited flames. Corona-generated flames demonstrate nearly linear growth immediately after the spark, due to the elimination of the laminar growth phase. Corona's advantage over IDI in minimizing ignition delay becomes even more pronounced in the lean and highly diluted mixtures, as can be seen in Figure 63. This behavior explains the shorter ignition delay of the corona system. The data does not extend late enough in the cycle to assess the behavior of the flame from MFB_{10} to MFB_{90}.

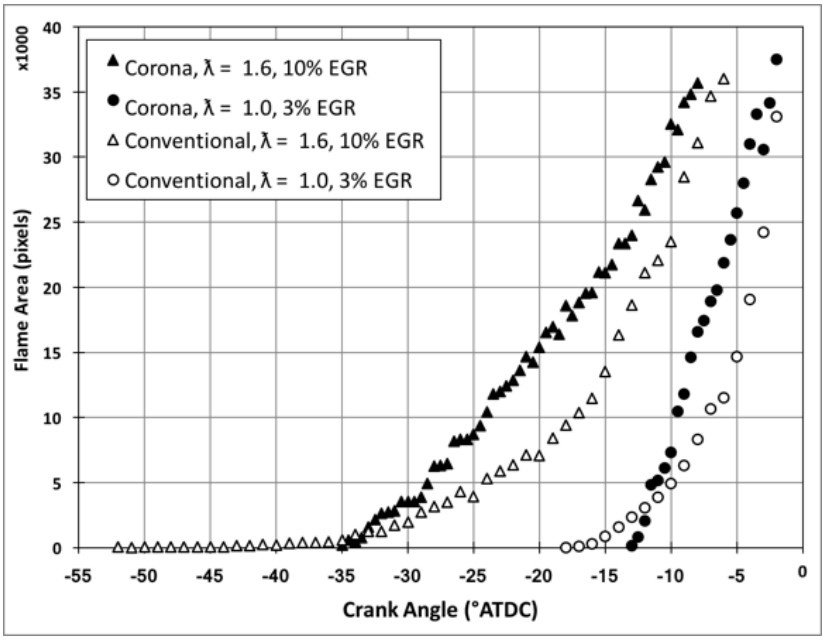

Figure 63. Flame area as a function of crank angle for two igniters and two mixtures, as measured by Camera 1 [73].

Figure 64 shows images recorded by Camera 1 at several crank angles for both ignition systems at a single operating condition: engine speed = 1000 rev/min, IMEP = 6.8 bar, λ = 1.0, and 3% EGR. Because the conventionally ignited flames grew more slowly than those ignited by the corona system the timing offset between measurements was 1.0 CAD for the conventional system and 0.5 CAD for the corona system. Additionally, because the ignition timing was optimized for each igniter, the images for the conventional igniter were recorded beginning at 0.75 CAD after spark timing (°aS), while those for the corona system were recorded beginning at 0.85 °aS. The images illustrate the differences in how the flame kernels evolve. The five streamers created by the corona igniter—the view of the rearmost one is obscured by the igniter in these images—creates a much larger, more wrinkled initial flame. This corona-ignited kernel also grows more quickly. It is believed that, since the kernel is wrinkled from its inception, it

skips the slow, laminar flame-growth phase and skips immediately to the fast, turbulent flame-growth phase.

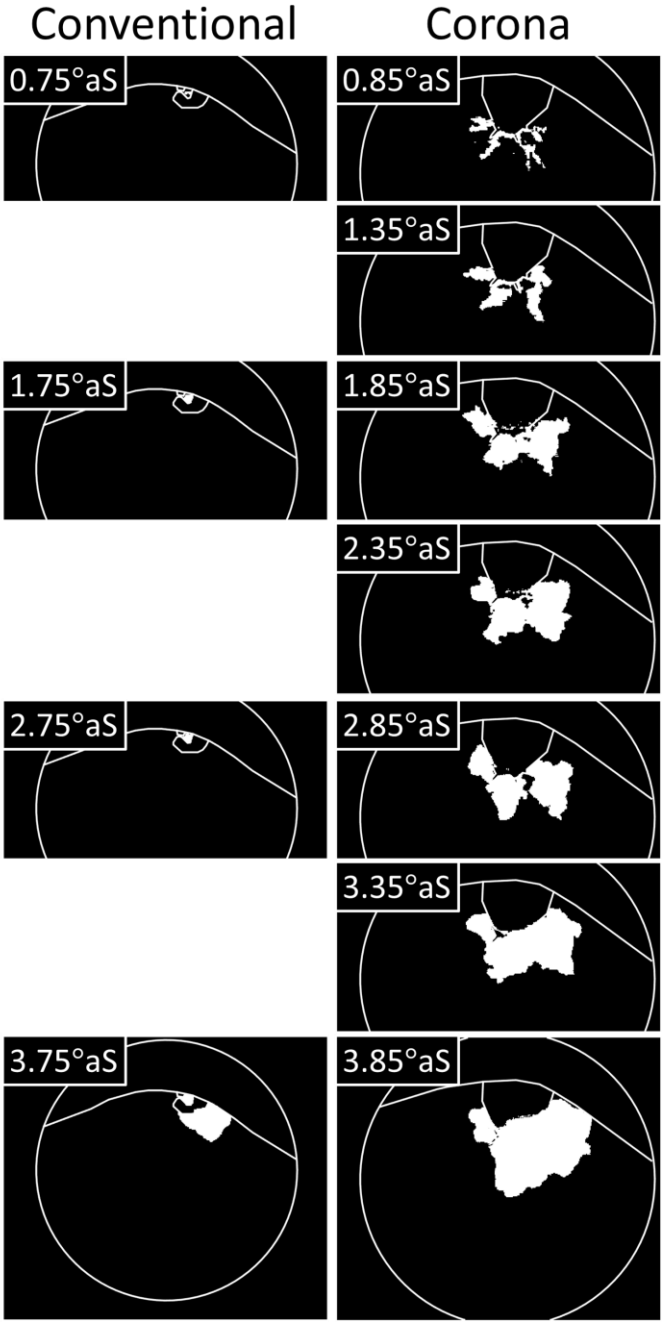

Figure 64. Binarized instantaneous image sequences of flame-kernel growth for two ignition systems. Engine speed is 1000 rev/min; IMEP = 6.8 bar; λ = 1.0, and 3% EGR. Images were taken at a lower rate for the conventional system due to the slower flame growth [80].

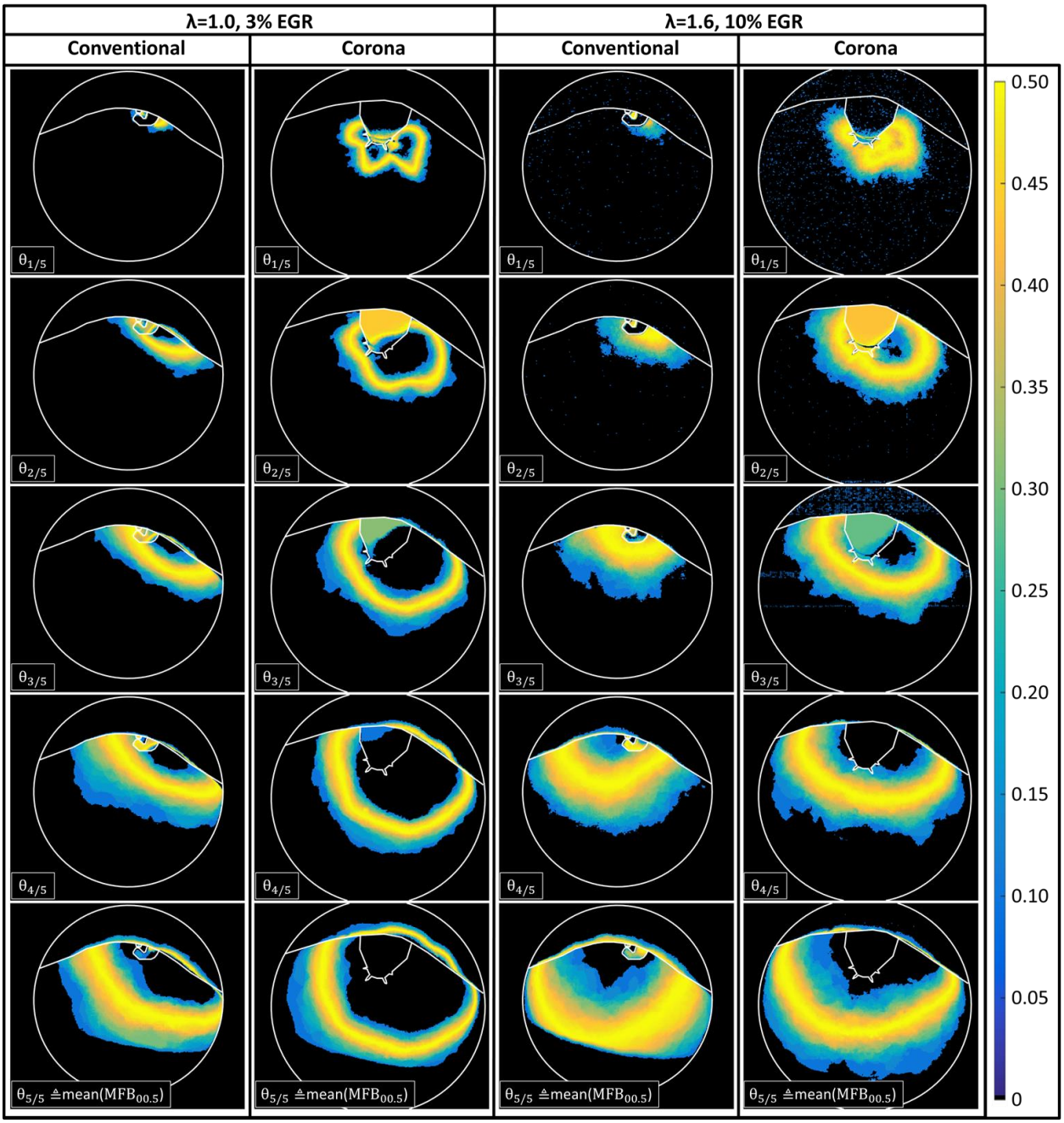

Figure 65. Standard deviation of binarized images at five normalized crank angles for two mixtures and two ignition systems. Engine speed is 1000 rev/min; IMEP = 6.8 bar. Lean, dilute mixtures yield more CCV than stoichiometric, minimally diluted mixtures, and corona-ignited flames exhibit less CCV than conventionally ignited ones. The CoV(IMEP) for each condition is, from left to right, 0.3%, 0.4%, 3.0%, and 1.9% [80].

Figure 65 shows the standard deviation of the binarized images at five normalized crank angles ($\theta_{1/5}$ through $\theta_{5/5}$) for both igniters, each igniting two mixtures. One condition is stoichiometric with minimal (3%) EGR; the other is lean with 10% EGR. In these figures, which are false-colored according to the scale shown on the right, the band of bright (yellow) pixels

represent the cycle-to-cycle variation in the flame boundary; wider bands indicate more CCV. Comparing the first column to the third and the second to the fourth reveals the bright (yellow) band is wider for the lean/dilute for each, indicating greater CCV for that mixture. Comparing column one to column two and column three to four shows that the bright band is wider for the conventional system, again pointing toward greater CCV with that system. These results agree with the pressure-based measurements of CoV(IMEP), which are reported in Table 9.

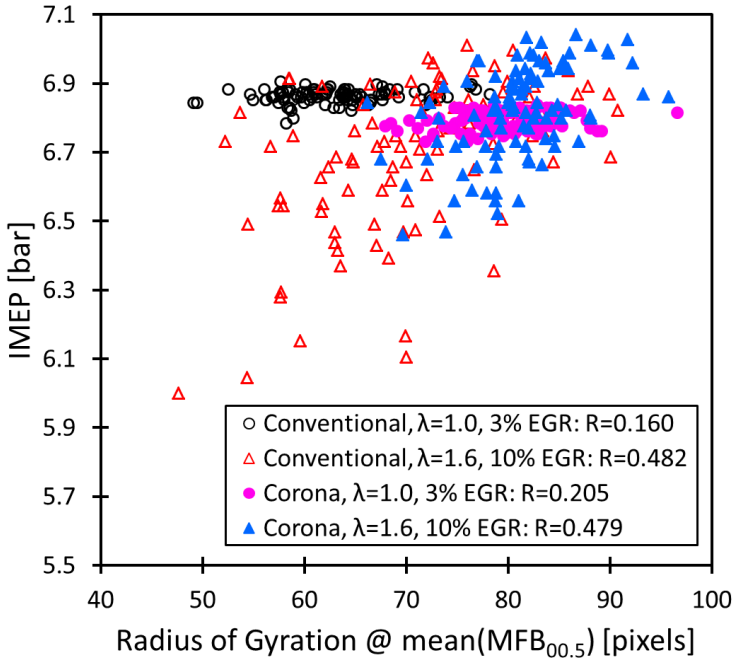

Figure 66. The IMEP of each cycle is insensitive to r_{gyr} at mean($MFB_{00.5}$) for the stoichiometric, minimally diluted mixtures, but it is sensitive to r_{gyr} for lean, dilute mixtures [80].

Figure 66 shows how the shape of the very early flame kernels has an impact on the highly diluted flames but not the stoichiometric ones as evidenced by the correlation between the radius of gyration measured at mean($MFB_{00.5}$) and the eventual IMEP of that cycle. This plot includes data from 100 cycles for each of the four igniter/mixture combinations. For both igniters, the lean, combustion the stoichiometric, minimally diluted mixture is robust under variation in r_{gyr}. In other words, the shape of the very early kernel has little impact on the combustion efficacy of each cycle, leading to very small Pearson correlation coefficients. By contrast, for both igniters, combustion of the lean, dilute mixture was very sensitive to variation in r_{gyr}. Different kernel shapes resulted in different IMEPs, leading to significant correlations. Note that the sensitivity of the igniters to the early-kernel shape are very similar, as indicated by the similar correlation coefficients: 0.482 for the conventional system, 0.479 for corona.

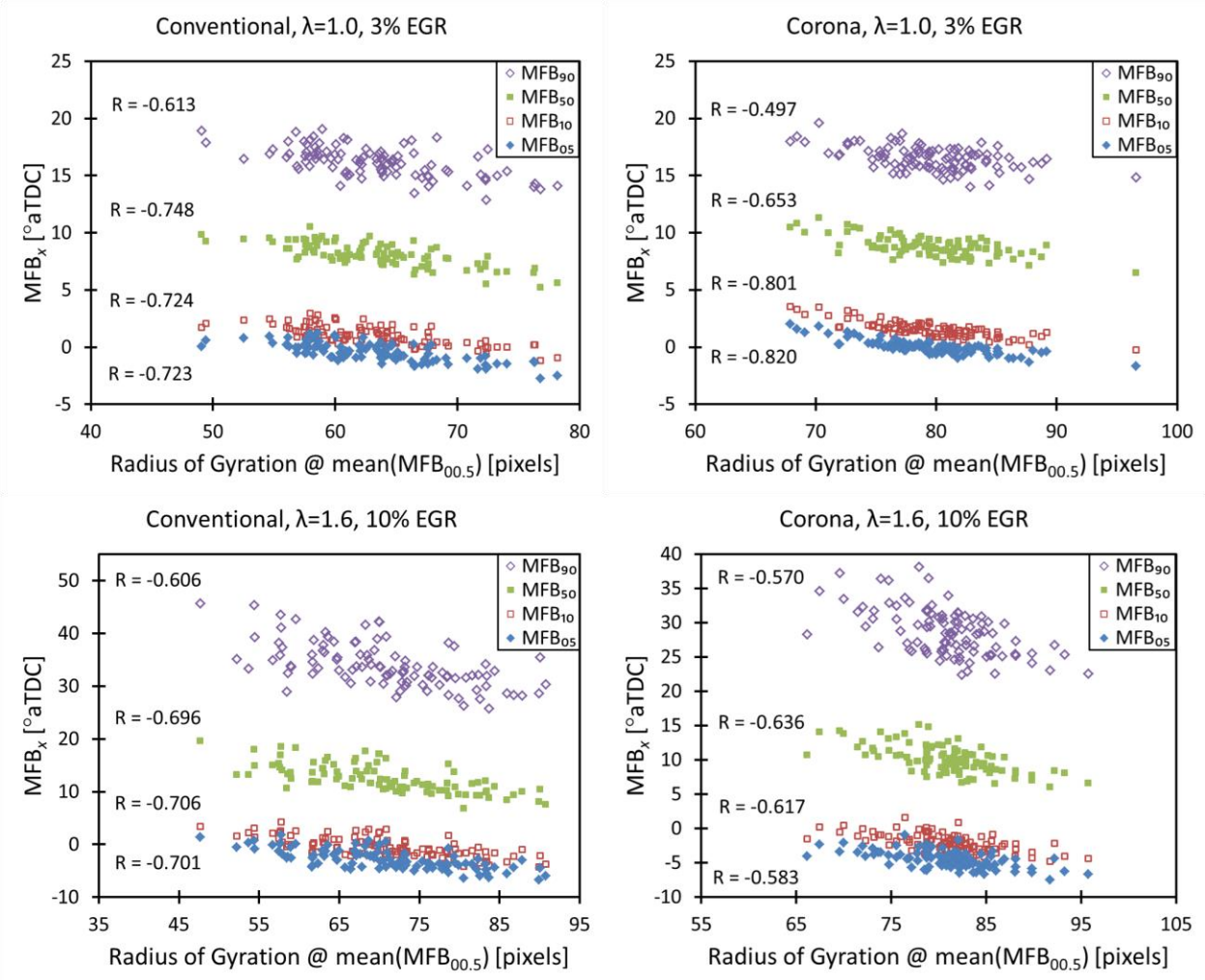

Figure 67. Correlation plots of r_{gyr} at mean($MFB_{00.5}$) and four MFB_x values for all four igniter/mixture combinations, MFB_{05}, MFB_{10}, MFB_{x50}, and MFB_{90} are negatively correlated with the r_{gyr} measured at mean($MFB_{00.5}$). The early MFB_x values are more strongly correlated than the later ones [80].

Figure 67 presents a series of correlation plots showing the relationship between the radius of gyration measured at mean($MFB_{00.5}$) and MFB_x (for x = 5, 10, 50, 90) for 100 cycles for all four combinations of air/fuel mixture and igniter. For all four combinations and all four values of x, a negative correlation with magnitude of at least 0.497 exists. In other words, early flames with more extended or stretched shapes reach these four combustion milestones more quickly. This result agrees with expectations, since extended kernel shapes are expected to be more wrinkled and to burn more quickly. It is important to note that all four MFB values occur much later in the cycle than the time at which r_{gyr} is measured, so this measurement demonstrates

predictive capability. As might be expected, the predictive capability is stronger for the earlier MFB values than the later ones.

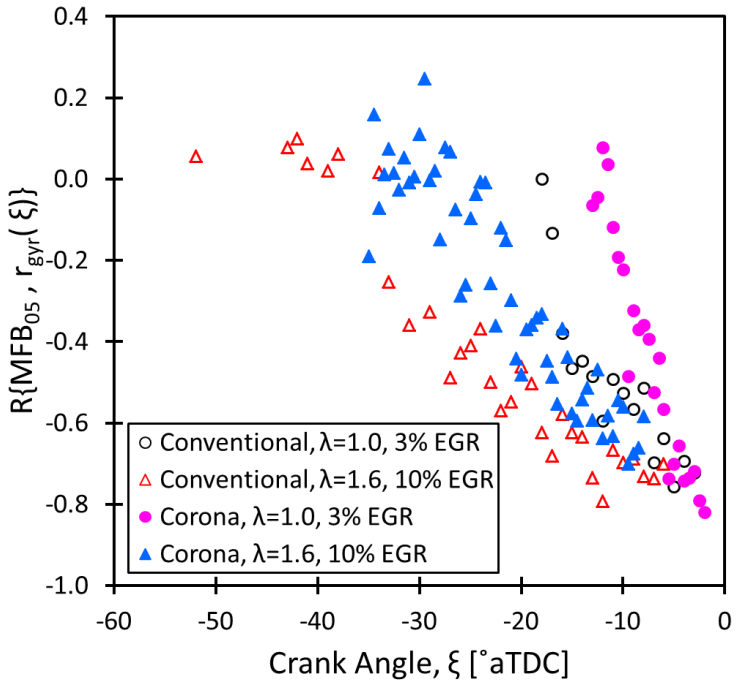

Figure 68. The negative correlation between MFB_{05} and the radius of gyration measured at a given crank angle is stronger if the r_{gyr} is measured at a later crank angle. The mean($MFB_{00.5}$) for each case is tabulated in Table 9 [80].

Figure 68 shows how the correlation between MFB_{05} and the radius of gyration measured at a given crank angle changes as the crank angle of r_{gyr} measurement varies. The result is qualitatively similar for all four igniter/mixture combinations: generally negative correlations that grow stronger as the crank angle of measurement approaches mean($MFB_{00.5}$). As discussed for Figure 67, the sign of the correlation (negative) is consistent with expectations. Additionally, the most negative values of the correlation coefficient are approximately -0.8 in all cases. It is important to note, however, that there are important differences between the cases. First, the data points for the four different cases begin at different crank angles, since the spark timing was optimized for each case, as tabulated in Table 9. Second, for both igniters, in the stoichiometric, undiluted case, the curves are much steeper than in the lean, dilute cases. This result may be due to the flames growing much more quickly in these cases or to the combustion being less sensitive to the flame shape.

4.3 Comparative UV-IR Imaging of Ignition Results

Figure 69 presents the plasma-to-flame transition of corona ignition of methane over a Hencken burner in the 280-340 nm band at 12 kHz, where the experimental setup details are explained in Chapter 3.2. The corona discharge duration is measured to be 380 μs, and the plasma streamers yield very strong signal during this period. The brightness of the plasma in UV is so high that the streamers appear saturated in the images. Still, the outlines of the streamers are visible. When imaging was performed in IR in the engine experiments (Section 4.2), these streamers were not captured. This is the first time they are recorded in this study, along with the subsequent flame (OH* radical) formation. As it can be seen at 417 μs in Figure 69, the OH* radicals start forming immediately following the discharge at spatially distinct locations where the streamers were.

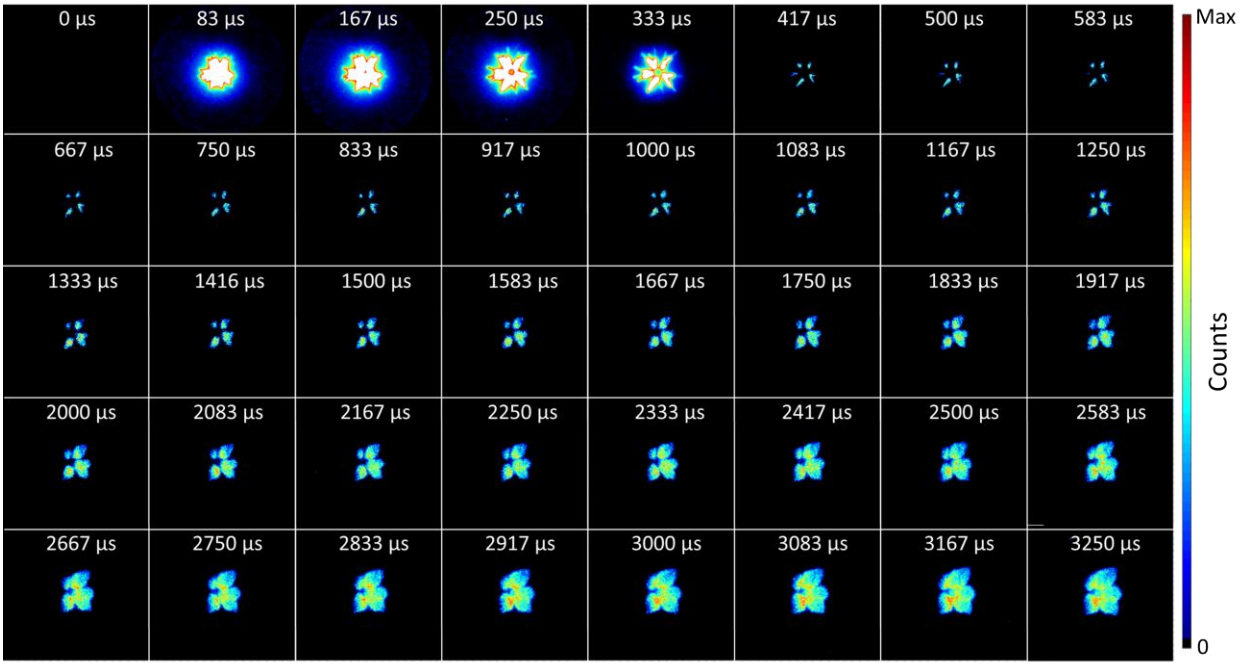

Figure 69. UV image progression of corona ignition over a Hencken burner at 12 kHz. The electrical discharge is initiated at 0 μs, and its duration is 380 μs.

In order to have a direct comparison between the IR and the UV signals, simultaneous imaging of corona ignition and flame propagation over a Hencken burner is performed as described in Chapter 3.9. The resultant comparison of image progressions is shown in Figure 70. The igniter boundaries on both IR and UV sides and the field of view in the UV images are outlined. Based on the voltage measurements, the spark duration is between 0-380 μs. At 341 μs, UV signal is very strong along the streamers that the plasma is saturated in the images, whereas

in the IR band there is no signal for corona plasma at the same instant. Subsequent ignition and flame propagation is shown until the flame reaches the boundary of the field of view. As expected, IR signal is the strongest around the centroid and the thick parts of the burned gas region, because the signal is mainly from H_2O, a combustion product. On the other hand, UV signal is strongest at the flame front, because the signal is from OH* radical. From the images, it could be observed that the flame is growing in the direction where the OH* signal is strongest.

Under the same voltage and duration settings, another interesting observation was made when the igniter failed to form corona streamers and formed an arc plasma between one of the electrode tips and the edge of the igniter's metal threaded part. This arc plasma and the subsequent ignition are also recorded. Simultaneous IR and UV progressions are shown in Figure 71. Note that the IR timing here is slightly different than the one shown in the successful corona ignition image sequence (Figure 70). The reason for that is the randomness of the initial signal input from the skip-fire box, which all have been recorded in every experiment to still be able to match sequences and make comparisons between cases. This skip-fire box related discrepancy prevented the arc plasma to be captured at its peak signal by the IR camera, but the UV image at 341 μs (same timing as the plasma shown in Figure 70) is added to guide the reader. This arc plasma also ignited the mixture, however, the flame formation was significantly slower and the flame signals were significantly lower at any given time after spark compared to the corona ignition case.

One of the factors that could affect the resolution of the flame front detection is the lifetime of emissions from H_2O molecules for IR imaging and OH* radicals for UV imaging. OH* is an electronically excited state of OH, so its lifetime is in the ~ns range. The H_2O molecules, on the other hand, emit through vibrational excitation. Thermal conduction from the flame front could potentially heat up the surrounding mixture and vibrationally excite the nearby H_2O molecules, and that can cause interfering H_2O emissions which could hinder the flame front detection. The UV-IR comparisons in Figure 70 and Figure 71 already show matching behavior in terms of flame shape under atmospheric pressure. Under engine pressures, the potentially hindering effect of added IR emissions via H_2O conduction would be even less of a problem, because the diffusive time scale is a function of the second power of characteristic length, and the mean free path of water molecules are estimated to drop from 904 nm (at 1 atm) to 134 nm (at 6.8 bar, which is the IMEP for all engine operations in this dissertation) at adiabatic flame

flame temperatures. This estimation indicates that there would be a ~50 fold reduction in diffusive time scales for the water molecules, hence the already clear IR image quality would further improve for flame detection.

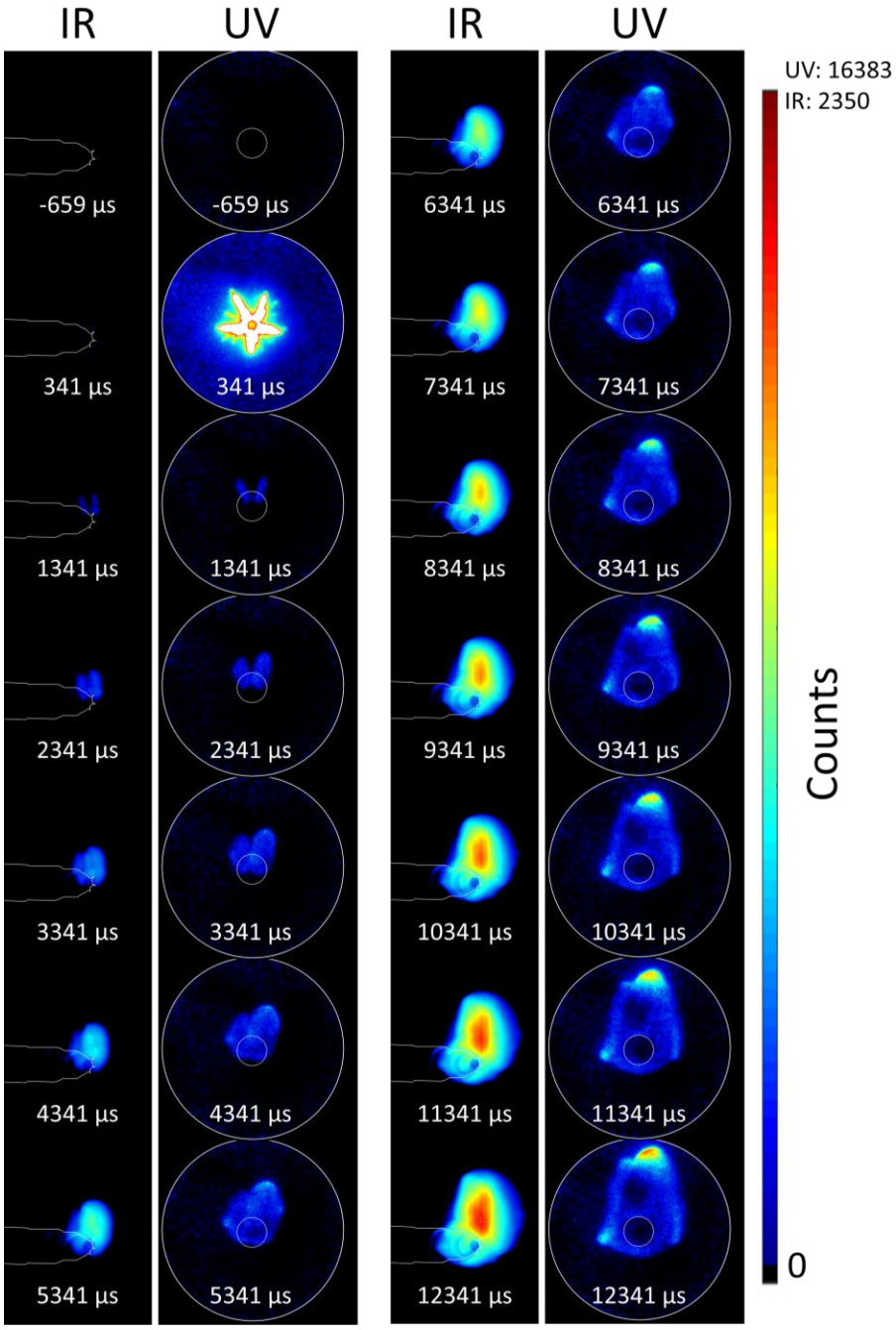

Figure 70. Side-by-side comparison of IR and UV images of corona ignition over a Hencken burner. The electrical discharge is initiated at 0 µs, and its duration is 380 µs. The outline of the igniter is overlaid on IR images. Field of view from the camera through intensifier (outer circle) and the outline of the igniter (inner circle) are overlaid on UV images.

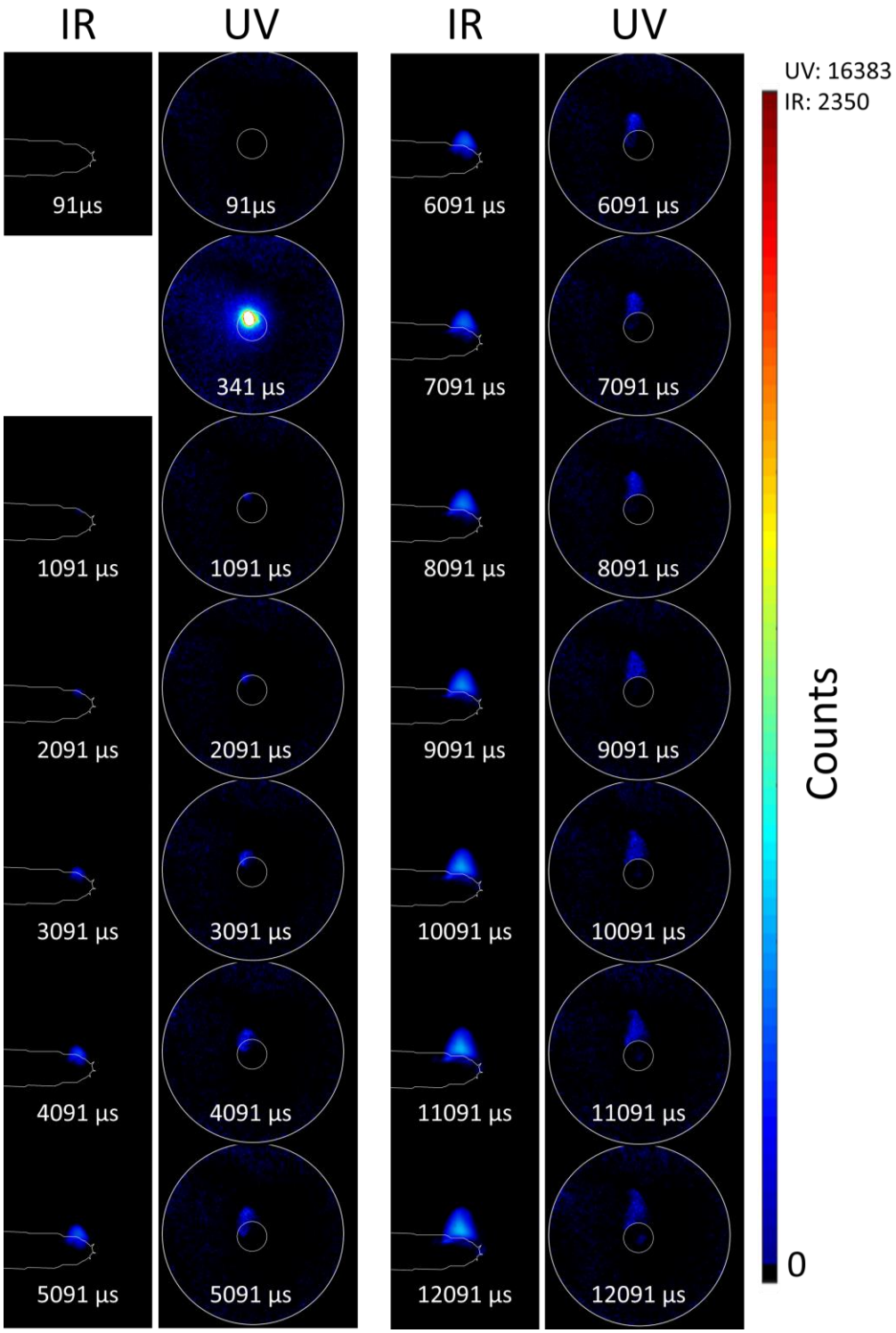

Figure 71. Side-by-side comparison of IR and UV images of arc (failed corona) ignition over a Hencken burner. The electrical discharge is initiated at 0 µs, and its duration is 380 µs.

In an effort to quantify the discrepancies between the IR and UV signals and corona and arc ignited cases, total signal from the recorded images are calculated and plotted in Figure 72.

Corona-ignited flame kernel had significantly larger and a faster growing signal in both IR and UV bands. Large intensities from plasmas caused high total signal peaks in the UV band (peaks above y-axis threshold, exact values not shown because these plasma images were saturated), whereas this behavior was not observed in the IR band. Additionally, total IR signal is observed to grow faster than the total UV signal during the flame kernel development. This could be attributed to the fact that H_2O is a product of combustion, and its amount keeps on increasing with the growth of burned mass volume, whereas OH* predominantly appears on the flame front only.

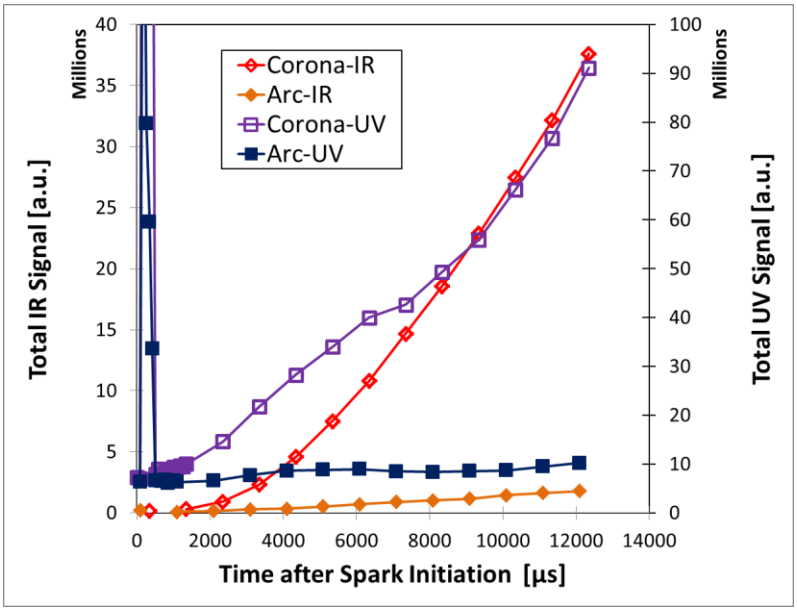

Figure 72. Total signal in IR and UV images as a function of time. Both corona and arc-ignited cases are shown.

The results from the comparative UV-IR imaging indicate that the borescopic IR imaging results reported in Chapter 4.2 would hold true for an equivalent UV-based analysis.

CHAPTER 5 SUMMARY AND CONCLUSIONS

Natural gas is a promising fuel for the heavy-duty internal combustion engine market due to its emissions, cost stability, and fuel security. In order to further improve the emissions and fuel economy, lean operation and EGR dilution are desired. However, reliable ignition of a lean and EGR-diluted natural gas in an engine is a challenging problem, because the higher auto-ignition temperature and lower flame speeds of diluted natural gas increase the risk of misfires, partial-burns. Additionally, such low flame speeds amplify the cycle-to-cycle variations that are mainly caused by inconsistent mixing conditions.

In order to help enable the full potential of natural gas as a marketable heavy-duty engine fuel, a better understanding of in-cylinder early flame kernel formation, factors that affect it, its effect on engine performance, and exploration of the ignition strategies that can promote desirable flame kernel formation are instrumental. Studying these early flame kernels is not possible merely with pressure-based measurements, since the pressure sensors cannot detect such small flame kernels. Therefore, optical diagnostic of the ignition event is required. In this PhD work, an infrared borescopic imaging system is built and employed to study the ignition event in a production-level engine.

In-cylinder infrared borescopic imaging of early flame-kernel growth has been described, and the procedure for processing these images and deriving quantitative metrics from them has been explained. These optical techniques were applied, along with standard measurements based on in-cylinder pressure, to a six-cylinder, 9.7-liter natural-gas-fueled heavy-duty engine burning four different air/fuel mixtures at an engine speed of 1000 rev/min and an IMEP of 6.8 bar. Imaging in the near infrared and short-wavelength infrared offered several advantages over visible-band optical diagnostics. Since the H_2O emissions are strong in this spectral region, the need for intensifiers or other additional equipment was eliminated. Additionally, the strength of this emission made it possible to obtain high-quality flame images through borescopes installed in a production engine, rather than an optically accessible engine, providing access to realistic operating conditions not available in optical engines.

Even with all the signal-to-noise ratio advantages that came with IR imaging, accurately identifying flame kernels in borescopic images have been challenging, because the in-cylinder images included background reflections from the cylinder surface that interfered with the signal collected from the flame, and signal-to-noise ratio was still not optimal at the first stages of flame kernel development. Several image processing tools have been investigated, developed, and assessed to optimize image segmentation for the flame identification problem. Gradient thresholding method had the best performance, because it could reliably remove reflections with varying intensity.

Following the image processing, a number of image-based metrics that characterize the flame were calculated, such as flame area, total flame signal, radius of gyration, and flame centroid. Several relationships between image-based metrics measured very early in the cycle, at mean($MFB_{00.5}$), and pressure-derived metrics measured much later in the cycle were observed:

- Flames centered farther from the head at mean($MFB_{00.5}$) lead to higher peak pressures, because the flames that grew farther from the head could keep their energy and grow faster without being quenched, which eventually lead to higher peak pressure in the combustion cycle. This result, which could not be obtained with pressure sensors only, showed that borescopic infrared high-speed imaging can provide guidance for future engine design, as the combustion chamber design influences the flame growth pattern.
- Flames displaced farther from the mean location at the beginning of combustion exhibited less consistent early flame growth (quantified by MFB_{10}) than flames not displaced as far. This result shows that the pressure-based variability and flame kernel location variability are interlinked, because inconsistency in ignition location leads to inconsistencies in temperature and flow field, for which the early flame kernel growth is highly sensitive.
- Flames with larger radii of gyration at mean($MFB_{00.5}$), in other words, flames with more extended shapes (due to high levels of flame stretching or wrinkling), were strongly correlated with higher peak combustion pressure, earlier values of MFB_{05}, MFB_{10}, and MFB_{50}, and were also correlated (though more weakly) with earlier values of MFB_{90}. Such early extended and wrinkled flames (large radius of gyration) are caused by high shear stress during ignition, and they possess a larger surface area at the same size, and this property enables them to grow faster than non-extended flames. The stronger correlation between early flame extendedness and the earlier MFB values, as opposed to lower correlation with later MFB values, indicates that the major improvement with the better performing ignition systems is in reduction of the ignition delay. Once the flame

wrinkling is achieved and a turbulent flame is established, then the rest of the flame growth (MFB_{90}-MFB_{10}) does not depend significantly on the ignition history.

- EGR dilution and lean operation caused an increase in flame-boundary variability in the early flame kernel that is consistent with the IMEP variability. EGR dilution and lean operation both reduce laminar flame speeds, and slower flames demonstrate higher sensitivity to spatial and cycle-to-cycle variations in thermodynamic and flow properties of the mixture, which is manifested as large flame boundary variability in standard deviation images. High variability in flame growth eventually results in high variability in engine performance parameters, such as IMEP.

These results were consistent with expectations, but it is important to note that the image-derived metrics revealed trends earlier in the cycle than they could be detected from the pressure measurements. Therefore, these metrics are shown to have predictive capability on the overall combustion cycle behavior in an internal combustion engine. The measurement techniques and image-processing procedures that were described here demonstrated how borescopic IR imaging can be used to obtain quantitative information about early flame kernel growth and how this is related to combustion performance.

In addition to understanding the basic relationships between the early flame kernels and full-cycle combustion, high-speed infrared in-cylinder imaging and image-based quantitative metrics combined with standard metrics derived from in-cylinder pressure measurements and emissions benches were used to investigate the differences between a standard-energy ignition system and two high-energy systems in a six-cylinder, 9.7-liter engine fueled with natural gas. Four operating points (all at 1000 rev/min engine speed and 6.8 bar IMEP) were studied for each igniter.

Pressure-derived measurements showed that, for this engine and these operating points, both of the high-energy igniters (the 140-mJ IDI system and the Controlled Electronic Ignition system) demonstrated lower cycle-to-cycle variation compared to 65-mJ igniter for mixtures that were lean, EGR-diluted, or both. In most lean or dilute cases, the 140-mJ IDI system demonstrated the lowest CoV(IMEP). Thus, high-energy igniters demonstrated their capability to ignite leaner and more EGR-diluted mixtures that are difficult to reliably ignite with conventional low-energy igniters. During the formation and the laminar growth regimes of the kernel before wrinkling, the flame is highly susceptible to quenching as its heat release rate via

combustion is low to combat the conductive heat losses from the flame surface to the mixture and the nearby solid boundaries (*e.g.*, electrodes). By providing additional energy to the flame kernel to combat such losses and to promote higher ionization, high energy igniters make the ignition process more robust. Similarly, longer ignition duration of these igniters play a role in quenching prevention and flame stretching as the flame kernel is moved by in-cylinder flows during spark discharge. With all the igniters, combustion with leaner and EGR-diluted mixtures yielded improved efficiency and emissions, as tabulated in Table 8.

In addition to the pressure-based results, CCV was also studied through borescopic infrared imaging of the early stages of flame-kernel development (from spark timing through $MFB_{00.5}$), where pressure-sensor data is not reliable. Under lean and EGR-diluted operation, CCV of early flame kernels generated by each igniter was visualized by standard-deviation images and flame-centroid tracking. The 65-mJ ignition system produced the largest regions of variability in the images, consistent with the measured CoV(IMEP). The centroid clouds show that cycles with flames farther from the head eventually result in high peak pressures, indicating that engine design and combustion strategy must keep the early flame towards the center of the chamber, and away from surfaces, in order to minimize the quenching and heat losses from the flame to these surfaces.

In the final stage of engine testing, the performance of a conventional spark ignition system and a corona ignition system were compared for stoichiometric and for lean, dilute mixtures. For the engine speed and load tested here (1000 rev/min and 6.8 bar IMEP) the high-frequency corona ignition system produced significantly shorter ignition delays, similar combustion durations, and lower CCV(IMEP) for each mixture tested ($\lambda = 1.0$ with 3% EGR and $\lambda = 1.6$ with 10% EGR) than a conventional IDI system delivering 65 mJ to each spark event. The corona system yielded shorter ignition delay and faster flame growth by increasing the effectiveness of spark-to-energy transfer (creating higher amount of OH* radicals quickly by using a non-equilibrium plasma), thus addressing the ignition limit, and by reducing the required flame-travel distances (using a distributed ignition source), thus addressing the partial-burn limit.

Additionally, the ignition delay and CCV were degraded less when going from the stoichiometric, minimally diluted case to the lean, dilute case when the corona igniter was used than when the conventional igniter was used. Since the corona igniter has five long (~20 mm) streamers instead of one short (~1 mm) spark plasma, it provides multiple elongated spatial

directions for the flame to initiate and grow on. As there are spatial and cycle-to-cycle variations in mixture composition, temperature, and flow field, the risk of having misfires or subpar ignition is greatly reduced with corona ignition, because the probability of having unfavorable mixture conditions at any point of the entire distributed streamer length is much lower than having unfavorable conditions at a localized short plasma near the engine head. Additionally, the streamers grow towards the center of the combustion chamber, which promotes the early flame kernel to grow away from the engine head, and reduces the early heat losses and partial quenching at the engine head. That robustness against variation manifests itself more strikingly when the global conditions in the cylinder (*e.g.*, air-fuel equivalence ratio, EGR ratio) reduce down the laminar flame speeds, thus emphasizing the effects of local inhomogeneities on the overall flame behavior. The combustion duration suffered similar degradation for both systems, which shows that, regardless of the igniter, the ignition quality mainly affects the duration and the physical processes in the flame initiation and early growth until the turbulent flame establishment, and not the MFB_{90}-MFB_{10} period.

The high-speed infrared images of the early flame kernels are consistently visible and clear, even before $MFB_{00.5}$, demonstrating that such imagery can provide valuable information about kernel development at points where data from pressure transducers are unreliable. The in-cylinder imagery also illustrated how the IDI- and corona-ignited flame kernels formed and grew differently. The flame area calculated from the IR images quantified the faster growth of the corona-ignited flames. The advantages of using a corona igniter for establishing a flame and promoting its rapid growth, even in highly dilute conditions, was directly evident from the images that were acquired via borescopic optical access. Further, a detailed analysis of the images showed that the flame development is highly sensitive to the geometric shape of the flame, confirming that the elongated flames with large surface areas grow faster. However, conventional igniters rely heavily on the in-cylinder flow properties to cause strain on the flame to reach this wrinkled elongated state, whereas corona igniter can create such a flame much more quickly without relying on the flow conditions as much by providing a larger and distributed ignition site.

In the engine experiments, majority of the collected signal in the near-IR band was from H_2O molecules in the burned gas region. Main advantage of IR imaging was the increased signal quality and the ability to observe early flame kernels without the need for intensifiers. However,

flame front identifying radicals (e.g., OH*), corona plasma, and major components of spark plasma mostly fall in the UV band. Additional Hencken burner experiments were conducted to aid the interpretation of the IR images from the engine. These benchtop experiments revealed several important conclusions. Simultaneous IR-UV imaging demonstrated the mapping between the H_2O molecules in the burned gas and the OH* radicals in the flame front. In addition to that, corona streamer-to-flame transition is captured at higher temporal resolution. Arc (failed corona) and corona flame kernel development characteristics are compared in IR and UV bands visually and quantitatively. The corona system, as expected by its non-equilibrium plasma, promoted faster OH* radical formation, which lead to faster ignition as consistent with the engine experiments. The temporal flame development characteristics in UV and IR bands in benchtop experiments demonstrated that there is a time delay between the start of the ignition process, evident by the luminosity from the corona discharge that is seen in the UV but not IR. However, once the plasma luminosity is over, the IR signals appear and they follow the UV signals, which means that the IR-based results discussed on flame development in the engine experiments will follow expected OH*-based analysis.

All in all, the most significant conclusions derived from this Ph.D. work could be succinctly summarized as below:

- Significant reduction in ignition delay in lean, EGR-diluted natural gas combustion is achieved when the early flame kernel is non-spherical (stretched, wrinkled, distributed).
- Corona ignition technique is highly effective in reducing ignition delays and providing robustness against cycle-to-cycle variations, because it creates distributed and wrinkled flame kernels very quickly without relying on the flow conditions to stretch the flame kernel as the point ignition methods do.
- High-speed borescopic infrared imaging of H_2O molecules is a highly applicable diagnostic technique to study flame kernels, as it yields comparable results to OH* imaging without the need of image intensifiers or laser excitation.

CHAPTER 6 FUTURE WORK

The work presented here provided valuable contribution to understanding the ignition and combustion variability in heavy-duty natural gas engines by use of borescopic infrared imaging. However, there are also newly emerged scientific or practical questions as well as remaining unanswered problems.

In the engine experiments, imaging was performed within 1.0-1.7 μm band to detect water molecules as a proxy to identify the flame locations. This way, cyclic variability of flame kernels was observed successfully. Similarly, pressure variation inside the engine cylinder was measured by pressure transducers. Mixture composition, on the other hand, which is observed to be one of the main parameters that contribute to cyclic variability, was only measured as a global parameter in the intake manifold as an integrated value over 100 cycles. Therefore, studying the effects of stratification, improper mixing, and residual gases in the engine was not possible within the course of this work. Simultaneous, high-speed and high-resolution spectral measurements inside the engine cylinder, specifically around the igniter and early flame kernel would yield a powerful contribution. Similarly, synchronized in-cylinder flow field and temperature measurements would contribute immensely to understanding the root causes of variations better. All these suggested measurements would have been even more valuable, if they could be performed in three dimensions.

The effectiveness of corona igniter to create wrinkled and elongated flame kernels is demonstrated in this study directly; however, this system's complete effect on altering the reaction kinetics and flame initiation by means of non-equilibrium plasma effects is not fully discovered. Differences in OH* radical generation is demonstrated on benchtop experiments, but additional spectroscopic measurements to detect key species around the spark plug under varying pressures and mixture compositions could yield valuable results.

Finally, more applications other than heavy-duty automotive engines that can utilize the flame initiation benefits of corona ignition should be surveyed and studied. Several supersonic and subsonic aerospace applications could be interesting first candidates to experiment as in [66].

BIBLIOGRAPHY

[1] "Liquefied Natural Gas Use: Basic Training Manual," Batelle, Pine & Associates UMTA-OH-06-0056-94.1, May 1994.

[2] G. Genchi and E. Pipitone, "Octane Rating of Natural Gas-Gasoline Mixtures on CFR Engine," 2014.

[3] V. Sick, "High speed imaging in fundamental and applied combustion research," *Proceedings of the Combustion Institute,* vol. 34, pp. 3509-3530, 2013.

[4] V. Sick, M. C. Drake, and T. D. Fansler, "High-speed imaging for direct-injection gasoline engine research and development," *Experiments in Fluids,* vol. 49, pp. 937-947, 2010.

[5] G. P. Agrawal, "Optical receivers," *Fiber-Optic Communication Systems,* pp. 133-182, 1997.

[6] S. R. Turns, *An Introduction to Combustion: Concepts and Applications*, 3rd ed. New York: McGraw-Hill, 2012.

[7] C. B. Ludwig, W. Malkmus, J. Reardon, J. Thomson, and R. Goulard, *Handbook of infrared radiation from combustion gases*. Washington, D.C.: Natioinal Aeronautics and Space Administration, 1973.

[8] J. Frank, R. Barlow, and C. Lundquist, "Radiation and nitric oxide formation in turbulent non-premixed jet flames," *Proceedings of the Combustion Institute,* vol. 28, pp. 447-454, 2000.

[9] S. Brookes and J. Moss, "Measurements of soot production and thermal radiation from confined turbulent jet diffusion flames of methane," *Combustion and Flame,* vol. 116, pp. 49-61, 1999.

[10] C. Paul, A. Sircar, S. Ferreyro-Fernandez, A. Imren, D. C. Haworth, S. P. Roy, *et al.*, "Modeling radiative heat transfer and turbulence-radiation interactions in engines," The Pennsylvania State University2017.

[11] S. R. Turns, *An Introduction to Combustion*, 3rd ed. New York: McGraw-Hill, 2011.

[12] A. A. Quader, "What limits lean operation in spark ignition engines-flame initiation or propagation?," SAE Technical Paper 760760, 1976.

[13] J. D. Dale, M. Checkel, and P. Smy, "Application of high energy ignition systems to engines," *Progress in Energy and Combustion Science,* vol. 23, pp. 379-398, 1997.

[14] H. Chen, M. Xu, D. L. Hung, and H. Zhuang, "Cycle-to-cycle variation analysis of early flame propagation in engine cylinder using proper orthogonal decomposition," *Experimental Thermal and Fluid Science,* vol. 58, pp. 48-55, 2014.

[15] D. L. Hung, H. Chen, M. Xu, J. Yang, and H. Zhuang, "Experimental investigation of the variations of early flame development in a spark-ignition direct-injection optical engine," *Journal of Engineering for Gas Turbines and Power,* vol. 136, p. 101503, 2014.

[16] P. Schiffmann, "Root Causes of Cycle-to-Cycle Combustion Variations in Spark Ignited Engines," 2016.

[17] P. Schiffmann, D. L. Reuss, and V. Sick, "Empirical investigation of spark-ignited flame-initiation cycle-to-cycle variability in a homogeneous charge reciprocating engine," *International Journal of Engine Research*, p. 1468087417720558, 2017.
[18] T. Alger, J. Gingrich, B. Mangold, and C. Roberts, "A continuous discharge ignition system for EGR limit extension in SI engines," *SAE International Journal of Engines*, vol. 4, pp. 677-692, 2011.
[19] G. Ruan, D. Kienzle, D. Roth, and M. Becker, "Dual coil ignition for gasoline EGR engines," *MTZ worldwide*, vol. 74, pp. 18-21, 2013.
[20] M. Brandt, A. Hettinger, A. Schneider, H. Senftleben, and T. Skowronek, "Extension of Operating Window for Modern Combustion Systems by High Performance Ignition," in *Ignition Systems for Gasoline Engines: 3rd International Conference, November 3-4, 2016, Berlin, Germany 3*, 2017, pp. 26-51.
[21] Y. Ikeda, A. Nishiyama, H. Katano, M. Kaneko, and H. Jeong, "Research and Development of Microwave Plasma Combustion Engine (Part II: Engine Performance of Plasma Combustion Engine)," 2009.
[22] B. Wolk, A. DeFilippo, J.-Y. Chen, R. Dibble, A. Nishiyama, and Y. Ikeda, "Enhancement of flame development by microwave-assisted spark ignition in constant volume combustion chamber," *Combustion and flame*, vol. 160, pp. 1225-1234, 2013.
[23] S. Bohne, G. Rixecker, V. Brichzin, and M. Becker, "High-Frequency Ignition System Based on Corona Discharge," *MTZ worldwide*, vol. 75, pp. 30-35, 2014.
[24] D. I. Pineda, B. Wolk, J.-Y. Chen, and R. W. Dibble, "Application of Corona Discharge Ignition in a Boosted Direct-Injection Single Cylinder Gasoline Engine: Effects on Combustion Phasing, Fuel Consumption, and Emissions," 2016.
[25] A. Schenk, G. Rixecker, and S. Bohne, "Results from Gasoline and CNG Engine Tests with the Corona Ignition System EcoFlash," in *Laser Ignition Conference*, 2015, p. W4A. 4.
[26] C. D. Cathey, T. Tang, T. Shiraishi, T. Urushihara, A. Kuthi, and M. A. Gundersen, "Nanosecond plasma ignition for improved performance of an internal combustion engine," *IEEE Transactions on Plasma Science*, vol. 35, pp. 1664-1668, 2007.
[27] D. L. Wisman, S. D. Marcum, and B. N. Ganguly, "Chemi-ion-current-induced dissociative recombination in premixed hydrocarbon/air flames," *Journal of Propulsion and Power*, vol. 24, pp. 1079-1084, 2008.
[28] T. X. Phuoc, "Laser-induced spark ignition fundamental and applications," *Optics and Lasers in Engineering*, vol. 44, pp. 351-397, 2006.
[29] E. G. Groff and M. K. Krage, "Microwave effects on premixed flames," *Combustion and flame*, vol. 56, pp. 293-306, 1984.
[30] H. Jaggers and A. Von Engel, "The effect of electric fields on the burning velocity of various flames," *Combustion and Flame*, vol. 16, pp. 275-285, 1971.
[31] N. Nakamura, T. Baika, and Y. Shibata, "Multipoint spark ignition for lean combustion," presented at the SAE Technical Paper 852092, 1985.
[32] T. Briggs, T. Alger, and B. Mangold, "Advanced ignition systems evaluations for high-dilution si engines," *SAE International Journal of Engines*, vol. 7, pp. 1802-1807, 2014.
[33] M. K. Das and S. T. Thynell, "Corona, Spark, and Electrothermal-Chemical Plasma Ignition Systems," *Handbook of Combustion*, 2010.

[34] R. Maly, "Spark Ignition: Its Physics and Effect on the Internal Combustion Engine," in *Fuel Economy in Road Vehicles Powered by Spark Ignition Engines*, G. S. S. John C. Hilliard, Ed., ed: Springer Science+Business Media, LLC, 1984, pp. 91-148.
[35] G. Ruan, D. Kienzle, and D. Roth, "Dual coil ignition for gasoline EGR engines," *MTZ worldwide*, vol. 74, pp. 18-21, 2013.
[36] H. Senftleben, "Advanced Ignition System," R. B. GmbH, Ed., ed, 2016.
[37] J. D. Dale, M. D. Checkel, and P. R. Smy, "Application of high energy ignition systems to engines," *Progress in Energy and Combustion Science*, vol. 23, pp. 379-398, 1997/01/01 1997.
[38] R. Anderson and J. Asik, "Lean air-fuel ignition system comparison in a fast-burn engine," SAE Technical Paper 0148-7191, 1985.
[39] R. W. Anderson, "The effect of ignition system power on fast burn engine combustion," SAE Technical Paper 0148-7191, 1987.
[40] B. Bihari, S. B. Gupta, R. R. Sekar, J. Gingrich, and J. Smith, "Development of advanced laser ignition system for stationary natural gas reciprocating engines," in *ASME 2005 Internal Combustion Engine Division Fall Technical Conference*, 2005, pp. 601-608.
[41] D. Graham-Rowe and R. Won, "Lasers for engine ignition," *Nature photonics*, vol. 2, p. 515, 2008.
[42] S. B. Gupta, R. R. Sekar, and G. E. Hillman, "Laser based ignition system for natural gas reciprocating engines, laser based ignition system having capability to detect successful ignition event; and distributor system for use with high-powered pulsed lasers," ed: Google Patents, 2006.
[43] S. B. Gupta, R. R. Sekar, Z. Xu, K. H. Leong, C. B. Reed, S. Pal, *et al.*, "Laser Based Ignition of Natural Gas-Air Mixtures," in *ASME 2003 Internal Combustion Engine Division Spring Technical Conference*, 2003, pp. 187-195.
[44] H. Yamamoto, S. Horita, and T. Matsuoka, "Surrounding combustion process (SCP)-new concept for lean burn engine," SAE Technical Paper 0148-7191, 1992.
[45] N. Nakamura, T. Baika, and Y. Shibata, "Multipoint spark ignition for lean combustion," SAE Technical Paper 0148-7191, 1985.
[46] R. D. Matthews, M. Hall, R. Faidley, J. Chiu, X. Zhao, I. Annezer, *et al.*, "Further analysis of railplugs as a new type of ignitor," SAE Technical Paper 0148-7191, 1992.
[47] E. Toulson, H. J. Schock, and W. P. Attard, "A review of pre-chamber initiated jet ignition combustion systems," SAE Technical Paper 0148-7191, 2010.
[48] A. K. Oppenheim, "Prospects for Combustion in Piston Engines," SAE Technical Paper 0148-7191, 2002.
[49] L. Gussak, M. C. Turkish, and D. C. Siegla, "High chemical activity of incomplete combustion products and a method of prechamber torch ignition for avalanche activation of combustion in internal combustion engines," SAE Technical Paper 0148-7191, 1975.
[50] L. Gussak, "The Role of Chemical Activity and Turbulence Intensity in Prechamber-Torch Organization of Combustion of a Stationary Flow of a Fuel-Air Mixture," SAE Technical Paper 0148-7191, 1983.
[51] S. Biswas and L. Qiao, "Prechamber Hot Jet Ignition of Ultra-Lean H 2/Air Mixtures: Effect of Supersonic Jets and Combustion Instability," *SAE International Journal of Engines*, vol. 9, 2016.
[52] P. L. Mtui and P. G. Hill, "Ignition delay and combustion duration with natural gas fueling of diesel engines," SAE Technical Paper 0148-7191, 1996.

[53] J. Liu, F. Yang, H. Wang, M. Ouyang, and S. Hao, "Effects of pilot fuel quantity on the emissions characteristics of a CNG/diesel dual fuel engine with optimized pilot injection timing," *Applied Energy*, vol. 110, pp. 201-206, 2013.
[54] (2016, 7/14). *First Generation Westport™ HPDI Technology: Westport High Pressure Direct Injection Technology*. Available: http://www.westport.com/is/core-technologies/combustion/hpdi
[55] R. J. Goldston and P. H. Rutherford, *Introduction to plasma physics*: CRC Press, 1995.
[56] H. C. Jaggers and A. von Engel, "The effect of electric fields on the burning velocity of various flames," *Combustion and Flame*, vol. 16, pp. 275-285, 1971/06/01 1971.
[57] E. S. Stockman, S. H. Zaidi, R. B. Miles, C. D. Carter, and M. D. Ryan, "Measurements of combustion properties in a microwave enhanced flame," *Combustion and Flame*, vol. 156, pp. 1453-1461, 7// 2009.
[58] Y. Ikeda, A. Nishiyama, Y. Wachi, and M. Kaneko, "Research and Development of Microwave Plasma Combustion Engine (Part I: Concept of Plasma Combustion and Plasma Generation Technique)," 2009.
[59] A. Fridman and L. A. Kennedy, *Plasma physics and engineering*: CRC press, 2004.
[60] J. Graf, T. Lauer, and B. Geringer, "Ignition systems for highly-supercharged downsized engines," *MTZ worldwide*, vol. 74, pp. 48-53, 2013.
[61] D. I. Pineda, J.-Y. Chen, and R. W. Dibble, "Corona discharge ignition in a single cylinder research engine under boosted conditions," 2016.
[62] D. I. Pineda, B. Wolk, T. Sennott, J.-Y. Chen, R. W. Dibble, and D. Singleton, "Nanosecond Pulsed Discharge in a Lean Methane-Air Mixture," in *Laser Ignition Conference*, 2015, p. T5A. 2.
[63] J. Sevik, T. Wallner, M. Pamminger, R. Scarcelli, D. Singleton, and J. Sanders, "Extending Lean and EGR-Dilute Operating Limits of a Modern GDI Engine Using a Low-Energy Transient Plasma Ignition System," in *ASME 2015 Internal Combustion Engine Division Fall Technical Conference*, 2015, pp. V001T03A007-V001T03A007.
[64] D. R. Singleton, J. O. Sinibaldi, C. M. Brophy, A. Kuthi, and M. A. Gundersen, "Compact pulsed-power system for transient plasma ignition," *IEEE Transactions on Plasma Science*, vol. 37, pp. 2275-2279, 2009.
[65] S. Starikovskaia, "Plasma assisted ignition and combustion," *Journal of Physics D: Applied Physics*, vol. 39, p. R265, 2006.
[66] A. Starikovskiy and N. Aleksandrov, "Plasma-assisted ignition and combustion," *Progress in Energy and Combustion Science*, vol. 39, pp. 61-110, 2013.
[67] A. Y. Starikovskiy, "On the role of 'hot' atoms in plasma-assisted ignition," *Philosophical Transactions of the Royal Society of London A: Mathematical, Physical and Engineering Sciences*, vol. 373, 2015-08-13 00:00:00 2015.
[68] N. Chintala, A. Bao, G. Lou, and I. V. Adamovich, "Measurements of combustion efficiency in nonequilibrium RF plasma-ignited flows," *Combustion and flame*, vol. 144, pp. 744-756, 2006.
[69] G. Lou, A. Bao, M. Nishihara, S. Keshav, Y. G. Utkin, J. W. Rich, *et al.*, "Ignition of premixed hydrocarbon–air flows by repetitively pulsed, nanosecond pulse duration plasma," *Proceedings of the Combustion Institute*, vol. 31, pp. 3327-3334, 2007.
[70] (2015, 7/21). *Transient Plasma Systems*. Available: http://www.transientplasmasystems.com/

[71] A. Mazacioglu, M. Gross, J. Kern, and V. Sick, "Infrared Borescopic Evaluation of High-Energy and Long-Duration Ignition Systems for Lean/Dilute Combustion in Heavy-Duty Natural-Gas Engines," in *SAE Technical Paper 2018-01-1149, 2018.*
[72] M. Gross, A. Mazacioglu, J. Kern, and V. Sick, "Infrared Borescopic Analysis of Ignition and Combustion Variability in a Heavy-Duty Natural-Gas Engine," presented at the SAE Technical Paper 2018-01-0632, 2018.
[73] A. Mazacioglu, M. C. Gross, J. Kern, and V. Sick, "Infrared borescopic characterization of corona and conventional ignition for lean/dilute combustion in heavy-duty natural-gas engines," *Proceedings of the Combustion Institute,* 2018.
[74] N. Otsu, "A threshold selection method from gray-level histograms," *IEEE transactions on systems, man, and cybernetics,* vol. 9, pp. 62-66, 1979.
[75] L. Jianzhuang, L. Wenqing, and T. Yupeng, "Automatic thresholding of gray-level pictures using two-dimension Otsu method," in *Circuits and Systems, 1991. Conference Proceedings, China., 1991 International Conference on*, 1991, pp. 325-327.
[76] N. Ladommatos and H. Zhao, *Engine combustion instrumentation and diagnostics*: SAE international Warrendale, PA, 2001.
[77] T. Ombrello, C. Carter, and V. Katta, "Burner platform for sub-atmospheric pressure flame studies," *Combustion and Flame,* vol. 159, pp. 2363-2373, 2012.
[78] F. A. Ayala and J. B. Heywood, "Lean SI engines: the role of combustion variability in defining lean limits," presented at the SAE Technical Paper 2007-24-0030, 2007.
[79] F. A. Matekunas, "Modes and measures of cyclic combustion variability," presented at the SAE Technical Paper 830337, 1983.
[80] V. Sick, L. Henrion, A. Mazacioglu, and M. C. Gross, "Time-resolved infrared imaging and spectroscopy for engine diagnostics," presented at the 13th International AVL Symposium on Propulsion Diagnostics, Baden-Baden, Germany, 2018.